

THESIS FOR THE DEGREE OF DOCTOR OF PHILOSOPHY

**Hydride-ion transport mechanisms in oxyhydrides
and nitride-hydrides: a neutron spectroscopy and
computational approach**

LUCAS FINE

Department of Chemistry and Chemical Engineering
CHALMERS UNIVERSITY OF TECHNOLOGY
Göteborg, Sweden 2025

**Hydride-ion transport mechanisms in oxyhydrides and nitride-hydrides:
a neutron spectroscopy and computational approach**

LUCAS FINE

ISBN 978-91-8103-258-1

This thesis work is part of a collaboration agreement between Chalmers University of Technology and the Institut Laue-Langevin (ILL), Grenoble, France. It has been financially supported primarily by grants from the ILL and the Swedish Research Council.

© LUCAS FINE, 2025

Doktorsavhandlingar vid Chalmers tekniska högskola
Ny serie nr 5716
ISSN 0346-718X

Department of Chemistry and Chemical Engineering
Chalmers University of Technology
SE-41296 Göteborg
Sweden
Telephone + 46 (0)31-772 1000

Cover: Hydride-ions and vacancies hosted within the channel-like structure of the novel nitride-hydride catalyst $\text{Ca}_3\text{CrN}_3\text{H}$, as revealed by neutron spectroscopy and machine learning molecular dynamics simulations.

Chalmers Digitaltryck
Gothenburg, Sweden 2025

Hydride-ion transport mechanisms in oxyhydrides and nitride-hydrides: a neutron spectroscopy and computational approach

LUCAS FINE

Department of Chemistry and Chemical Engineering
Chalmers University of Technology

Abstract

This thesis investigates the fundamental mechanisms governing hydride-ion transport in the novel nitride-hydride $\text{Ca}_3\text{CrN}_3\text{H}$ and oxyhydride perovskites $\text{ATiO}_{3-x-y}\text{H}_x\Box_y$ ($\text{A} = \text{Ba}, \text{Sr}$, and \Box denotes anion vacancies), which are promising materials for energy and catalysis applications. However, key questions remain regarding the structure-dynamics relationships that govern their transport behavior. To address these, this thesis combines quasielastic and inelastic neutron scattering with density functional theory and molecular dynamics simulations to probe the diffusional and vibrational dynamics of hydride-ions. The aim is to provide a comprehensive understanding of the structural and chemical factors enabling hydride-ion transport and to guide the development of energy and catalytic devices based on these materials.

In the nitride-hydride $\text{Ca}_3\text{CrN}_3\text{H}$, the results reveal characteristic hydride-ion vibrational modes correlated with the hydride-ion site occupancy, and the analysis of the vibrational spectrum indicates the presence of vacant sites. These vacancies enable jump-diffusion dynamics, including localized, back-and-forth motions, and successive jumps across nearest-neighbor vacancies. Both dynamics are characterized by exceptionally low activation energies, which facilitates the hydride-ion transport.

In the oxyhydride perovskites $\text{ATiO}_{3-x-y}\text{H}_x\Box_y$, hydride-ion diffusion similarly requires anion vacancies and proceeds via jumps to nearest-neighbor vacancies. The results suggest that both localized, back-and-forth jumps and long-range, successive jumps can occur on comparable timescales in regions with sufficient vacancy content. However, in regions of lower vacancy content, long-range transport is impeded due to the lack of continuous pathways of vacancies and hydride-ions. Additionally, the results show that localized electrons (i.e., polarons) increase the migration energy barrier of hydride-ions compared to delocalized electrons in the conduction band.

These findings showcase the critical role of both anion vacancy concentration and electronic structure in enabling efficient hydride-ion transport, providing design principles for developing next-generation nitride-hydride and oxyhydride hydride-ion conductors and catalysts.

Keywords: *oxyhydride, nitride-hydride, hydride-ion, ionic transport, neutron scattering, density functional theory, molecular dynamics.*

List of publications

This thesis is based on the following publications:

I Configuration and Dynamics of Hydride Ions in the Nitride-Hydride Catalyst $\text{Ca}_3\text{CrN}_3\text{H}$

L. Fine, R. Lavén, Z. Wei, T. Tsumori, H. Kageyama, R. Kajimoto, M. Jimenéz-Ruiz, M. M. Koza, and M. Karlsson
Chemistry of Materials 2025 37 (1), 489-496

II One-dimensional Hydride-Ion Conduction in the Nitride-Hydride $\text{Ca}_3\text{CrN}_3\text{H}$

L. Fine, R. Lavén, Z. Wei, T. Tsumori, M. Matsuura, H. Tamatsukuri, H. Kageyama, M. M. Koza, and M. Karlsson
In Manuscript

III Mechanism of Hydride-Ion Diffusion in the Oxyhydride of Barium Titanate

R. Lavén, L. Fine, E. Naumovska, H. Guo, U. Häussermann, A. Jaworski, M. Matsuura, M. M. Koza, and M. Karlsson
The Journal of Physical Chemistry C 2025 129 (27), 12305-12311

IV Unraveling the Electronic Control of Hydride Diffusivity in Oxyhydrides from Model Studies on $\text{BaTiO}_{3-x}\text{H}_y$

L. Fine, I. Panas, M. Karlsson, and M. M. Koza
Submitted

V Localized Jump-Diffusion Dynamics of Hydride-Ions in an Oxyhydride of SrTiO_3 Studied using Inelastic and Quasielastic Neutron Scattering

L. Fine, R. Lavén, E. Naumovska, H. Guo, U. Häussermann, A. Jaworski, M. Jimenéz-Ruiz, G. J. Nilsen, M. M. Koza, and M. Karlsson
In Manuscript

Additional publications not included in this thesis:

VI Proton Diffusion in Proton Conducting $\text{Ba}_2\text{In}_{1.85}\text{M}_{0.15}\text{O}_5$ ($\text{M} = \text{In}, \text{Ga}, \text{Sc}$ and Y) Investigated with Quasielastic Neutron Scattering

E. Naumovska, L. Fine, A. Perrichon, F. Piccinelli, N. Jalarvo, F. Juranyi, M. M. Koza, and M. Karlsson
Submitted

Contribution report

My contributions to the included papers:

- I** I contributed to the planning of the INS experiments. I was the main responsible for data collection and data analysis. I was also the main responsible for the planning, execution, and analysis of the computer calculations. I was the main responsible for writing the manuscript.
- II** I contributed to the planning of the QENS experiments. I was the main responsible for data collection and data analysis. I was also the main responsible for the planning, execution, and analysis of the computer calculations. I was the main responsible for writing the manuscript.
- III** I contributed to the planning of one of the QENS experiments, for which I was the main responsible for data collection. I was co-responsible for the data analysis of all QENS experiments. I contributed to the writing of the manuscript.
- IV** I contributed to the planning of the DFT calculations. I was the main responsible for their execution and data analysis. I was the main responsible for writing the manuscript.
- V** I contributed to the planning of the QENS experiments. I was co-responsible for data collection and the main responsible for data analysis. I was the main responsible for writing the manuscript.

Contents

| | |
|---|-----------|
| Introduction | 1 |
| 1 Mixed-anion compounds | 5 |
| 1.1 The oxyhydrides $\text{ATiO}_{3-x-y}\text{H}_x\text{□}_y$ | 7 |
| 1.1.1 Transition metal oxyhydrides | 7 |
| 1.1.2 Synthesis and structure | 8 |
| 1.1.3 Hydride-ion transport | 10 |
| 1.1.4 Electronic properties | 13 |
| 1.2 The nitride-hydride $\text{Ca}_3\text{CrN}_3\text{H}$ | 15 |
| 1.2.1 Nitride-hydride materials | 15 |
| 1.2.2 Crystal structure | 15 |
| 1.2.3 Hydride-ion transport and catalytic properties | 16 |
| 2 Neutron scattering | 19 |
| 2.1 Concepts of nuclear scattering | 19 |
| 2.1.1 About neutrons | 19 |
| 2.1.2 Scattering kinematics | 20 |
| 2.1.3 Dynamical structure factor | 21 |
| 2.1.4 Coherent and incoherent scattering | 22 |
| 2.1.5 Uniaxial polarization analysis | 25 |
| 2.2 Inelastic neutron scattering | 26 |
| 2.2.1 Localized vibrations of hydride-ions | 26 |
| 2.2.2 Collective vibrations of hydride-ions | 28 |
| 2.3 Quasielastic neutron scattering | 30 |
| 2.3.1 Long-range diffusion | 31 |
| 2.3.2 Localized diffusion | 31 |
| 2.3.3 Fitting analysis of QENS spectra | 32 |

| | | |
|----------|---|-----------|
| 3 | Neutron spectrometers | 35 |
| 3.1 | Time-of-flight spectrometers | 36 |
| 3.2 | Backscattering spectrometers | 39 |
| 3.3 | A modified three-axis spectrometer: IN1-LAGRANGE | 41 |
| 4 | Computational methods | 45 |
| 4.1 | Density functional theory | 45 |
| 4.1.1 | Modeling vibrational motions with DFT | 48 |
| 4.1.2 | Modeling diffusional motions with DFT | 49 |
| 4.2 | Ab initio molecular dynamics | 51 |
| 4.3 | Machine learning-based molecular dynamics | 52 |
| 4.3.1 | Modeling vibrational motions with MLMD | 55 |
| 4.3.2 | Modeling diffusional motions with MLMD | 55 |
| 5 | Summary of results | 57 |
| 5.1 | Hydride-ion dynamics in $\text{Ca}_3\text{CrN}_3\text{H}$ | 57 |
| 5.1.1 | Coordination environment and dynamics of hydride-ions in $\text{Ca}_3\text{CrN}_3\text{H}$ (Paper I) | 57 |
| 5.1.2 | Hydride-ions transport properties of $\text{Ca}_3\text{CrN}_3\text{H}$ (Paper II) . . | 60 |
| 5.2 | Hydride-ion dynamics in $\text{ATiO}_{3-x-y}\text{H}_x\text{□}_y$ | 63 |
| 5.2.1 | Mechanism of hydride-ion transport in $\text{BaTiO}_{3-x-y}\text{H}_x\text{□}_y$ (Paper III) | 63 |
| 5.2.2 | Effects of electron localization on hydride-ion transport in $\text{BaTiO}_{3-x-y}\text{H}_x\text{□}_y$ (Paper IV) | 66 |
| 5.2.3 | Localized diffusion of hydride-ions in $\text{SrTiO}_{3-x-y}\text{H}_x\text{□}_y$ (Paper V) | 68 |
| 6 | Conclusions | 73 |
| A | Catalytic activity of $\text{Ca}_3\text{CrN}_3\text{H}$ | 77 |
| B | Data reduction for a TOF spectrometer | 79 |
| | Acknowledgements | 83 |
| | Bibliography | 83 |

List of abbreviations

| | |
|------|---|
| AIMD | Ab. Initio Molecular Dynamics |
| DFT | Density Functional Theory |
| EISF | Elastic Incoherent Structure Factor |
| FWHM | Full Width at Half Maximum |
| GDOS | Generalized Density Of States |
| INS | Inelastic Neutron Scattering |
| MD | Molecular Dynamics |
| MEP | Minimum Energy Path |
| MLIP | Machine Learning Interatomic Potential |
| MLMD | Machine Learning-based Molecular Dynamics |
| NEB | Nudged Elastic Band |
| NMR | Nuclear Magnetic Resonance |
| PES | Potential Energy Surface |
| PDOS | Partial Density Of States |
| PSD | Position Sensitive Detector |
| PXRD | Powder X-Ray Diffraction |
| QENS | Quasielastic Neutron Scattering |
| TAS | Three-Axis Spectrometer |
| TOF | Time Of Flight |
| XRD | X-Ray Diffraction |
| ZPE | Zero Point Energy |

Introduction

A fundamental understanding of the physics of solid-state materials drives the rational design of the next-generation technologies across diverse fields of materials science, including, for example, electronics, optics, nanotechnology, energy, and catalysis. Traditionally, research in these fields has focused on *single-anion* compounds, such as pure metal oxides, fluorides, and nitrides, with the diversity of their properties largely determined by the choice of metal cations. Notable examples of technologically important single-anion materials include for instance barium titanate (BaTiO_3), widely used in capacitors for its ferroelectric properties [1]; yttria-stabilized zirconia (YSZ), employed in solid oxide fuel cells (SOFCs) due to its high oxide-ion conductivity [2]; and lithium manganese oxide (LiMnO_2), used in lithium-ion batteries for its high energy density [3].

As this cation-centered research approaches saturation, an emerging class of *mixed-anion* materials, compounds containing more than one type of anion, remains largely unexplored. These materials offer the potential for novel functionalities and improved performance through anion-driven design principles [4–6]. Understanding the structure-property relationships in mixed-anion systems is therefore crucial for predicting and designing materials that may outperform their single-anion counterparts.

This thesis focuses in particular on exploring the structure–property relationships in mixed-anion materials with potential for energy and catalysis applications, both critical to the transition toward a decarbonized economy [7–9]. Examples of such applications include SOFCs, which are among the promising technologies for converting decarbonized energy between chemical and electrical forms [10, 11], and the catalytic synthesis of ammonia (NH_3), which is essential for global food production and increasingly considered as a potential green fuel [12–14]. However, both SOFCs and traditional ammonia catalysts face significant challenges due to their high operating temperatures (typically 600–1000 °C for SOFCs and 400–500 °C for ammonia synthesis) and, in the case of ammonia production, high pressures (150–300 bar). Together, these conditions result in considerable energy consumption and motivate

the development of more efficient materials [2, 10, 12, 14].

Recent research has increasingly focused on hydride-ion-containing mixed-anion materials, particularly oxyhydride and nitride-hydride compounds, which exhibit unique properties that may help address these challenges [5, 15]. The hydride-ion (H^-) is highly polarizable and size-flexible, making it adaptable to various local structural environments. It also possesses a moderate electronegativity, enabling it to participate in covalent, metallic, and ionic bonding [4, 5, 16, 17]. These characteristics are favorable for fast hydride-ion transport in solids, an essential feature for reducing the high operating temperatures and pressures of energy and catalytic devices [18–23].

For instance, hydride-ion transport was demonstrated in an all-solid-state electrochemical cell using the oxyhydride electrolyte La_2LiHO_3 , which exhibits a conductivity of approximately 10^{-5} S/cm at 300°C [20]. In this setup, the electrolyte is sandwiched between a Ti anode, where the discharge reaction is $\text{Ti} + x \text{H}^- \longrightarrow \text{TiH}_x + xe^-$, and a TiH_2 cathode, where the reverse reaction occurs: $\text{TiH}_2 + xe^- \longrightarrow \text{TiH}_{2-x} + x \text{H}^-$ [Figure 1(a)]. The cell demonstrated a steady discharge current of $0.5 \mu\text{A}$ at 300°C , highlighting the feasibility of hydride-ion conduction in oxyhydride systems at relatively low temperature.

Hydride-ion transport is also of interest for ammonia synthesis, which occurs *via* the reaction $\text{N}_2 + 3 \text{H}_2 \longrightarrow 2 \text{NH}_3$. Recent efforts toward mild synthesis conditions (1 bar, $< 300^\circ\text{C}$) often rely on ruthenium (Ru)-based catalysts, which promote the cleavage of the strong $\text{N} \equiv \text{N}$ triple bond, the rate-limiting step in ammonia formation [13]. Recent developments using Ru nanoparticles supported on oxyhydride or nitride-hydride substrates have demonstrated reduced activation energies, attributed to the participation of lattice hydride-ions in the catalytic process [19, 24–27]. For instance, the catalyst $\text{Ru}/\text{BaCeO}_{3-x}\text{N}_y\text{H}_z$ outperformed its oxide-only counterpart Ru/BaCeO_3 by one order of magnitude in synthesis rate, and under milder conditions (300°C , 9 bar) [24]. In this system, the hydride-ions participate *via* a Mars–van Krevelen mechanism: a lattice hydride-ion reacts with a neighboring nitride ion or an adsorbed N_2 molecule, and the resulting vacancy is subsequently refilled either by diffusion of another lattice hydride-ion or by a H_2 molecule from the reactant atmosphere [Figure 1(b)].

Despite the demonstrated performance of oxyhydride and nitride-hydride in energy and catalytic applications, the microscopic mechanisms governing hydride-ion transport in these systems remain largely unknown. In this context, the present thesis aims to contribute to the fundamental understanding of hydride-ion transport in such mixed-anion systems. It focuses on two representative compounds: $\text{ATiO}_{3-x-y}\text{H}_x\Box_y$ (with $\text{A} = \text{Ba}, \text{Sr}, \text{Ca}$, where \Box denotes oxygen vacancies and

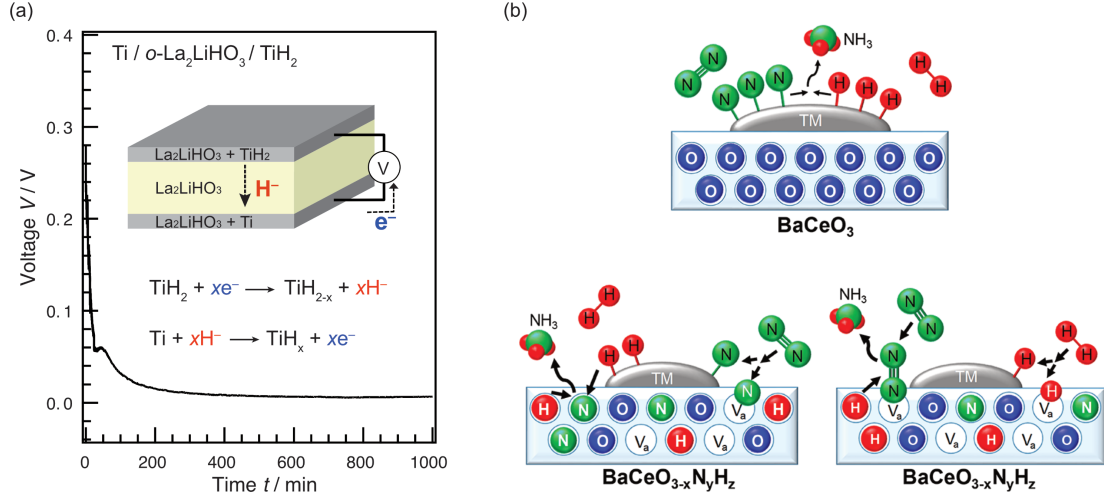


Figure 1: Hydride-ion-containing mixed-anion materials for energy and catalysis applications. (a) Discharge curve of an all-solid-state electrochemical cell using an oxyhydride electrolyte. Reproduced from [20] with permission from AAAS. (b) Schematic illustration of a possible reaction mechanism for ammonia synthesis on a pure oxide support (top) and on an oxide–nitride–hydride support (bottom), both supporting a transition metal (TM, typically ruthenium) nanoparticle. Reproduced with permission from [24]. Copyright 2019 American Chemical Society.

$x < 0.6$), and $\text{Ca}_3\text{CrN}_3\text{H}$, both exhibiting hydride-ion conductivity and catalytic activity under mild conditions [27–29]. Notably, $\text{ATiO}_{3-x-y}\text{H}_x\text{O}_y$ adopts a perovskite structure where hydride and oxide ions are randomly distributed over the same anion sublattice. In contrast, $\text{Ca}_3\text{CrN}_3\text{H}$ features a one-dimensional channel structure that hosts hydride-ions and guides their transport. The relatively simple structures of these compounds make them ideal model systems for investigating hydride-ion dynamics in mixed-anion materials.

This thesis addresses the following questions:

What are the underlying mechanisms governing the hydride-ion transport in $\text{Ca}_3\text{CrN}_3\text{H}$ and $\text{ATiO}_{3-x-y}\text{H}_x\text{O}_y$?

What are the structural and chemical requirements for enabling such hydride-ion transport?

How can hydride-ion conductivity be enhanced in these systems?

Neutrons are particularly well suited for these investigations due to their high sensitivity to hydrogen species. In this work, quasielastic neutron scattering (QENS) is employed to probe hydride-ion diffusional dynamics, which relate to hydride-ion transport, and inelastic neutron scattering (INS) is used to probe hydride-ion vibrational dynamics, which reflect the local coordination environment of hydride ions. These experimental techniques are complemented by atomistic simulations, including density functional theory (DFT) and molecular dynamics (MD).

Chapter 1

Mixed-anion compounds

Mixed-anion materials are a class of compounds that incorporate two or more distinct types of anions within a single crystalline phase, offering more opportunities for tuning their physical and chemical properties, compared to single-anion materials. Among them, the most extensively studied systems are oxide-based mixed-anion compounds, including oxyhydrides (oxide-hydrides), oxynitrides (oxide-nitrides), and oxyfluorides (oxide-fluorides), but other families, such as nitride-hydrides, are also gaining attention [4–6, 15].

Combining anions with varying anionic characteristics, such as charge, ionic radii, electronegativity, and polarizability, enables greater flexibility in materials design. The introduction of chemically distinct anions at different lattice sites can lead to unusual coordination environments that serve as structural “building blocks” for novel crystal structures with new properties, as illustrated in Figure 1.1(a) [4, 5, 15]. Several examples of such emergent features resulting from anion mixing are described below and illustrated in Figure 1.1(b).

Notably, replacing oxide ions (O^{2-}) with other anions can alter bond strengths and bonding character, potentially enhancing chemical reactivity and facilitating anionic diffusion. For example, the oxyhalides LaOCl and LaOBr exhibit Cl^- and Br^- ion conduction, respectively, due to the weaker La-Cl and La-Br bonds compared to La-O bonds in the parent oxides [30, 31]. Another example is the synthesis of the nitride-hydride $\text{BaTiO}_{3-x}\text{N}_{2x/3}$ *via* an ammonia gas exchange reaction with the oxyhydride precursor $\text{BaTiO}_{3-x}\text{H}_x$ [32]. Anion substitution also influences electronic structures. In particular, introducing anions with lower electronegativity than O^{2-} raises the valence band maximum in oxide-based semiconductors, narrowing the band gap. This effect is used in compounds like the oxynitride TaON , which enables visible-light water splitting catalysis due to its reduced band gap [33]. In

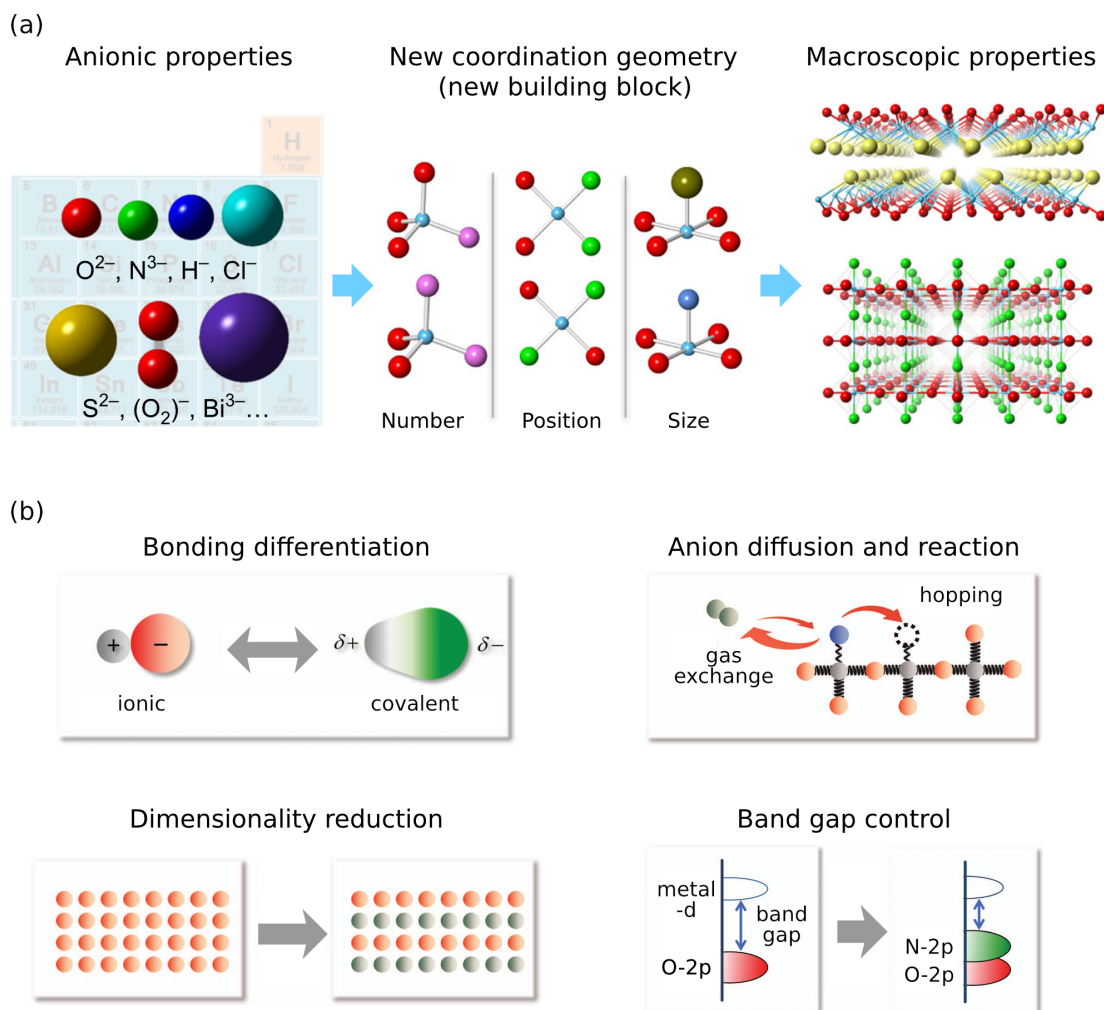


Figure 1.1: Principles and characteristics of mixed-anion compounds. (a) Schematic illustration of novel local coordination environments (*building blocks*) formed in mixed-anion compounds, which can give rise to emergent macroscopic properties. (b) Selected examples of structural and functional characteristics enabled by anion mixing. Adapted from [5], open access.

cases where substituted anions differ substantially in size or electronegativity, they may order over long ranges within the structure, resulting in reduced dimensionality compared to the parent oxides. For instance, in the oxyhalides $\text{Sr}_2\text{CuO}_2\text{F}_{2+\delta}$ and

(Ca, Na)₂CuO₂Cl₂, the substitution of apical O²⁻ ions with F⁻ or Cl⁻ induces two-dimensional electronic states in the CuO₂ layers and give rise to superconductivity with critical temperatures (T_c) of 46 K and 26 K, respectively [34, 35].

Among the variety of mixed-anion compounds, those incorporating hydride-ions are relatively rare but exhibit remarkable properties due to the unique characteristics of the hydride-ion. Unlike conventional p-block anions, the hydride-ion consists of a single proton and two electrons and lacks valence p orbitals. This fundamental difference strongly influences its bonding behavior and magnetic interactions. Notably, its bipolar nature and moderate electronegativity enable hydride-ions to participate in covalent, metallic, and ionic bonding with other elements [17]. In addition, hydrogen can readily gain or lose an electron, converting between the proton (H⁺) and H⁻ forms, making it highly adaptable to its local chemical environment. Unlike a proton, which can be considered as a point charge, the hydride-ion has a flexible spatial extent due to its low charge density. Its effective ionic radius ranges from approximately 1.27 to 1.52 Å, whereas oxide ions (O²⁻) typically have a more consistent radius of about 1.40 Å [17].

These distinctive properties open the door to various applications for hydride-ion-containing mixed-anion compounds, particularly in energy conversion and storage, as well as in catalysis. For energy storage, the high redox potential of the H⁻/H₂ couple (-2.2 V vs. SHE) is advantageous [17, 20]. In energy conversion devices, the lability of hydride ions, which is facilitated by their adaptable size and bonding characteristics, can enable low-temperature ion transport [20, 21]. The same lability is also promising for catalytic applications, most notably in ammonia synthesis [18, 19].

The transport properties (also referred to as hydride-ion lability, diffusion, or conductivity) of hydride-ions in mixed-anion compounds are the central focus of this thesis. In particular, this work investigates hydride-ion dynamics in two representative systems: the oxyhydrides ATiO_{3-x-y}H_x□_y and the nitride-hydride Ca₃CrN₃H, with the aim of clarifying the fundamental mechanisms governing their hydride-ion transport properties and establishing design principles for novel oxyhydride- and nitride-hydride-based fast hydride-ion conductors.

1.1 The oxyhydrides ATiO_{3-x-y}H_x□_y

1.1.1 Transition metal oxyhydrides

The oxyhydrides ATiO_{3-x-y}H_x□_y (with A = Ba, Sr, Ca, where □ denotes oxygen vacancies and $x < 0.6$) belong to the broader class of transition metal oxyhydrides. The first compound in this class, LaSrCoO₃H_{0.7}, was reported in 2002 by Hayward

et al. [36]. It was synthesized *via* a solid-state reaction at relatively low temperature (450 °C) between the oxide precursor LaSrCoO_4 and the reducing agent CaH_2 . This method is referred to as a topochemical reaction, as it preserves the overall framework of the parent structure while replacing some oxide ions with hydride-ions.

Following this pioneering work, the topochemical method was extended to the synthesis of other transition metal oxyhydrides such as $\text{LnSrCoO}_{3+a}\text{H}_b$ (with $\text{Ln} = \text{Pr, Nd}$) [37] and $\text{Sr}_3\text{Co}_2\text{O}_{4.33}\text{H}_{0.84}$ [38]. A significant breakthrough occurred in 2012 when Kobayashi *et al.* synthesized $\text{BaTiO}_{3-x}\text{H}_x$ with x up to 0.6 [28]. Unlike $\text{LnSrCoO}_{3+a}\text{H}_b$ and $\text{Sr}_3\text{Co}_2\text{O}_{4.33}\text{H}_{0.84}$, where the transition metal (Co) typically exhibited unusually low oxidation states, +1.7 and +1.75, respectively, the titanium in $\text{BaTiO}_{3-x}\text{H}_x$ exists in more conventional oxidation states of +3 or +4, as commonly found in titanium oxides. This discovery challenged the prevailing notion that low transition metal oxidation states were necessary for stabilizing hydride-ions, thereby opening the way for the synthesis of titanium-based oxyhydrides. Notably, the synthesis of the related compounds $\text{ATiO}_{3-x}\text{H}_x$ ¹ (with $\text{A} = \text{Ba, Sr, Ca}$) came shortly after [39, 40]. Later on, alternative synthesis methods involving high-pressure and high-temperature conditions enabled the preparation of additional oxyhydride phases such as SrVO_2H [41] and SrCrO_2H [42].

1.1.2 Synthesis and structure

The $\text{ATiO}_{3-x-y}\text{H}_x\Box_y$ systems are synthesized *via* a topochemical reduction route, as illustrated in Figure 1.2. As a result, there is a topotactic relationship between the parent oxide and its reduced form, meaning that the reduced oxyhydride inherits its crystal structure from the original perovskite-type oxide ATiO_3 (Figure 1.3). The crystal structure of the system depends on the A-site cation. At room temperature, both CaTiO_3 and its reduced form $\text{CaTiO}_{3-x-y}\text{H}_x\Box_y$ adopt an orthorhombic structure, while SrTiO_3 and $\text{SrTiO}_{3-x-y}\text{H}_x\Box_y$ are cubic. In contrast, BaTiO_3 is tetragonal, but its reduced form $\text{BaTiO}_{3-x-y}\text{H}_x\Box_y$ is cubic. This difference arises from the reduction of Ti^{4+} to Ti^{3+} , which eliminates the ferroelectric distortion responsible for the tetragonal symmetry in BaTiO_3 [39].

In their discovery, Kobayashi *et al.* demonstrated that the hydride-ion content (x) in $\text{BaTiO}_{3-x}\text{H}_x$ can be tuned by adjusting the reaction conditions, specifically the temperature and reaction time, with a maximum hydride content of $x = 0.6$ observed before the decomposition of the sample occurs [28]. Subsequent studies further revealed the presence of oxygen vacancies and achieved the synthesis of a

¹Note, in these reports, the samples did not contain any significant amount of oxygen vacancies, and the compositions were considered stoichiometric.

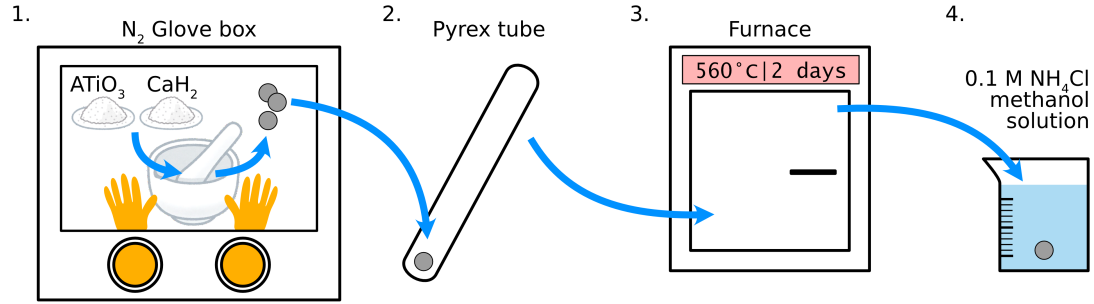


Figure 1.2: Topochemical synthesis of $\text{ATiO}_{3-x-y}\text{H}_x\text{O}_y$ oxyhydrides. The ATiO_3 precursor and the reducing agent (here CaH_2) are mixed in a mortar and pelletized (1), within an inert gas atmosphere (here, N_2). The pellets are sealed in Pyrex glass tubes under vacuum (2) and heated at 500-600 °C for a few days. Finally, the products are washed with 0.1 M NH_4Cl methanol solution to remove excess CaH_2 and CaO , and dried in a vacuum oven at 120 °C.

series of $\text{BaTiO}_{3-x-y}\text{H}_x\text{O}_y$ compounds with $x \approx 0.1$ and y ranging from 0 to 0.38, by varying the reaction temperature between 300 and 600 ° [43, 44]. Notably, these studies also demonstrated that a variety of reducing agents, such as LiH , MgH_2 , NaAlH_4 , and NaBH_4 , could be used in place of CaH_2 , each resulting in samples with different compositions. However, despite these advances, the influence of synthesis conditions on the resulting oxyhydride composition remains poorly understood, and

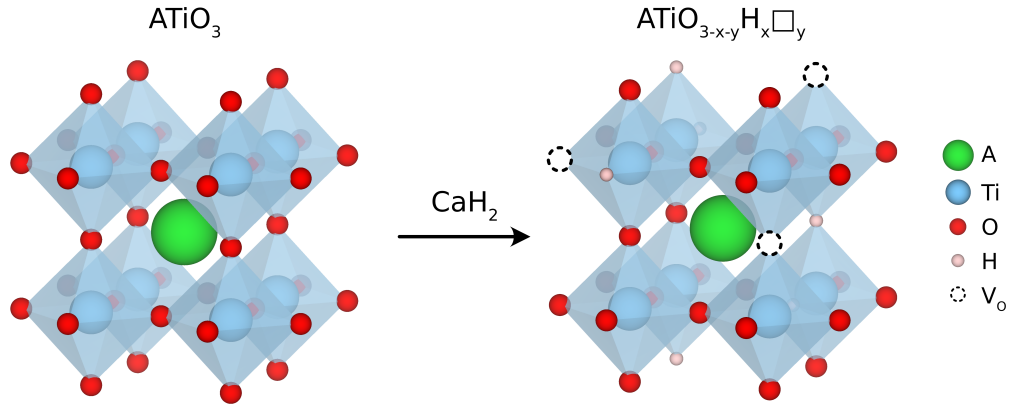


Figure 1.3: Reduction of an ATiO_3 perovskite to its oxyhydride form $\text{ATiO}_{3-x-y}\text{H}_x\text{O}_y$. The hydride-ions are disordered on the oxide ion sites.

predicting the final stoichiometry from synthesis parameters remains challenging. Yet, the hydride-ion and oxygen vacancy contents are crucial for the application of these systems in energy and catalytic devices, as they govern their hydride-ion transport properties.

1.1.3 Hydride-ion transport

The first demonstration of hydride-ion transport in transition metal oxyhydrides was reported in 2006 by Bridges *et al.* in the compound $\text{LaSrCoO}_3\text{H}_{0.7}$ [50]. Using QENS, they detected a hydride-ion diffusion signal interpreted as jump-diffusion between oxygen vacancies. Notably, this signal was observed only at temperatures above 400 °C, i.e., close to the decomposition point of the material, and was accompanied by the release of H_2 . These findings raised the question: can hydride-ion transport also occur below the decomposition temperature, within the thermodynamically stable regime of oxyhydrides? If so, these materials could serve as practical hydride-ion conductors. A similar observation was made in $\text{ATiO}_{3-x-y}\text{H}_x\Box_y$ systems, where H_2 release upon heating was reported around 400–500 °C, depending on sample composition [28, 39]. While such thermal desorption indicates hydride-ion lability near the decomposition limit, these studies did not directly probe hydride-ion transport mechanisms, as in the QENS study on $\text{LaSrCoO}_3\text{H}_{0.7}$.

Hydride-ion transport mechanism in $\text{ATiO}_{3-x-y}\text{H}_x\Box_y$ systems was further investigated *via* H/D exchange experiments, secondary ion mass spectrometry (SIMS) profiling experiments, QENS experiments, solid-state nuclear magnetic resonance (NMR) experiments, and DFT calculations. The key results of these studies are summarized in Table 1.1.

As with $\text{LaSrCoO}_3\text{H}_{0.7}$, these results have been interpreted in terms of hydride-ion jump-diffusion between neighboring oxygen vacancies. Due to the perovskite structure, two types of vacancy sites are considered: nearest-neighbor (NN) and second-nearest-neighbor (2NN) sites. NN sites are separated by approximately 2.8 Å, while 2NN sites are about 4 Å apart, which makes NN jumps more favorable due to their shorter distances. However, given that each hydride-ion is surrounded by 8 NN sites, at least 25% of the anion sublattice must be composed of hydride-ions or vacancies (randomly distributed) to establish a percolation pathway for NN hydride-ion transport. This corresponds to the condition $x + y \geq 0.75$, which is relatively demanding since the hydride-ion content does not exceed $x < 0.6$. Consequently, in most compositions, NN transport pathways formed by hydride-ion or vacancy may be incomplete or unavailable. Nevertheless, hydride-ion transport has been observed in samples with $x + y < 0.75$, suggesting that other transport pathways contribute.

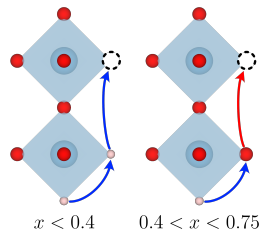
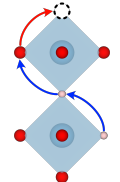
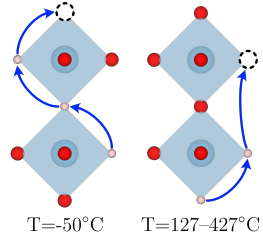
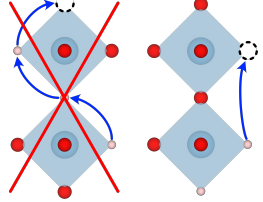
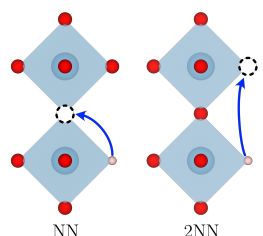
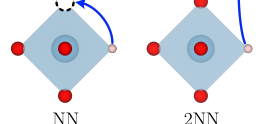

| Sample | Technique | T (°C) | E_a (eV) | Interpretation | Ref. |
|---|---------------------------------------|----------|---|---|------|
| $\text{BaTiO}_{3-x}\text{H}_x$ $x = 0.35\text{--}0.6$ | H/D exchange + Kissinger method | 400–600 | 3.8–2.3 |  | [45] |
| $\text{SrTiO}_{3-x}\text{H}_x$ $x = 0.35, 0.45$ | H/D exchange + SIMS profiling | 350–450 | 0.45–0.47 |  | [46] |
| $\text{BaTiO}_{3-x-y}\text{H}_x\Box_y$ $x = 0.1, y = 0.1\text{--}0.66$ | QENS | -50–427 | ≈ 0.1 |  | [47] |
| $\text{BaTiO}_{3-x-y}\text{H}_x$ $x = 0.13\text{--}0.31$ | NMR | -173–147 | - |  | [48] |
| $\text{BaTiO}_{3-x-y}\text{H}_x\Box_y$ $x, y = 0.125$ | DFT | - | ≈ 1 eV (NN) ≈ 3 eV (2NN) |  | [45] |
| $\text{BaTiO}_{3-x-y}\text{H}_x\Box_y$ $x, y = 0.037$ | DFT | - | ≈ 0.28 eV (NN) |  | [49] |
| $\text{SrTiO}_{3-x-y}\text{H}_x\Box_y$ $x, y = 0.037$ | DFT | - | ≈ 0.17 eV (NN) |  | [46] |

Table 1.1: Summary of key literature results on hydride-ion transport in $\text{ATiO}_{3-x-y}\text{H}_x\Box_y$ systems, as investigated using various techniques. In the schematics, blue arrows represent hydride-ion jumps, while red arrows indicate oxide-ion jumps.

These include 2NN hydride-ion jumps, and oxide-ion jumps (of both NN and 2NN types). Owing to the longer jump distances and higher mass of oxide ions, these processes are generally slower and associated with higher activation energies (E_a).

As shown in Table 1.1, no clear consensus has yet been reached regarding the dominant transport mechanism in $\text{ATiO}_{3-x-y}\text{H}_x\Box_y$ systems. This lack of agreement arises from several factors. First, the compositions of the studied samples vary significantly. Second, different temperature ranges are probed, with some studies focusing on diffusion near the decomposition temperature and others at much lower temperatures. Finally, the techniques employed probe transport at vastly different spatial and temporal scales: H/D exchange experiments probe diffusion over $0.1\ \mu\text{m}$ and minute timescales, QENS probes atomic-scale ($1\ \text{\AA}$) dynamics on the nanosecond timescale, and NMR probes over picosecond to millisecond timescales. These differences can lead to substantial discrepancies in reported results. Notably, H/D exchange techniques capture bulk transport, including grain boundary effects, which may significantly hinder ion mobility, whereas QENS and NMR primarily probe local (bulk) jump events.

Further insight comes from DFT studies. Some proposed a mechanism in which a hydride-ion transiently transforms into a proton that diffuses interstitially [51, 52]. However, this mechanism has been less supported, as QENS and INS studies have not observed such proton species [47, 53]. Other DFT calculations estimated the activation energies for NN and 2NN jumps, but their value significantly varies on computational settings, and discrepancies also exist between theoretical and experimental E_a values (see Table 1.1).

Despite the inconsistencies, several key trends are emerging: (i) Hydride-ion transport is possible at relatively low temperatures, even near $0\ ^\circ\text{C}$. (ii) At elevated temperatures, 2NN jumps and oxide-ion can contribute to the transport. (iii) The composition of the sample influences the nature of the transport mechanism: higher hydride-ion and vacancies contents seem to enhance hydride-ion transport.

One of the goals of this thesis is to clarify these trends and clarify the discrepancies in the literature by developing a more complete and detailed picture of hydride-ion transport mechanisms in $\text{ATiO}_{3-x-y}\text{H}_x\Box_y$ systems.

This knowledge will provide a more comprehensive understanding of the structural and chemical requirements that enable fast hydride-ion transport in oxyhydrides and may guide the development of next-generation energy and catalytic devices based on these materials [18–21, 26, 27, 54].

1.1.4 Electronic properties

The reduction of ATiO_3 oxides to their oxyhydride phases, $\text{ATiO}_{3-x-y}\text{H}_x\Box_y$, is accompanied by a color change. For instance, BaTiO_3 is white, and turns dark blue upon reduction to $\text{BaTiO}_{3-x-y}\text{H}_x\Box_y$ [Figure 1.4(a)]. This change is attributed to the reduction of Ti^{4+} to Ti^{3+} , indicating that the electronic structure is modified in the reduction process [28].

When an oxide ion is replaced by a hydride-ion or removed (creating a vacancy), the valence electrons originally associated with the O^{2-} ion can adopt two configurations (Figure 1.5). They may either localize in the vacancy of near a Ti^{4+} cation, forming so-called electron polarons, which create in-gap states between the valence band (VB) and conduction band (CB), leading to semiconducting behavior. Alternatively, the electrons may delocalize across the Ti sublattice, populating the CB and giving rise to a bandstate, leading to metallic behavior. Indeed, both semiconductor-like and metallic behavior have been observed in $\text{BaTiO}_{3-x-y}\text{H}_x\Box_y$. Kobayashi *et al.* reported semiconducting behavior in pelletized powder samples with $0.1 < x < 0.6$ [28]. In contrast, epitaxial thin films of $\text{ATiO}_{3-x}\text{H}_x$ ($A = \text{Ba}, \text{Sr}, \text{Ca}$) in the range $0.25 < x < 0.6$ exhibited metallic conductivity [40]. A systematic study further revealed that $\text{SrTiO}_{3-x}\text{H}_x$ films remain metallic across the entire compositional range $0.05 < x < 0.6$, whereas $\text{BaTiO}_{3-x}\text{H}_x$ has a semiconducting behavior for $x < 0.2$ and a metallic behavior for $x > 0.2$ [Figure 1.4(b)] [56].

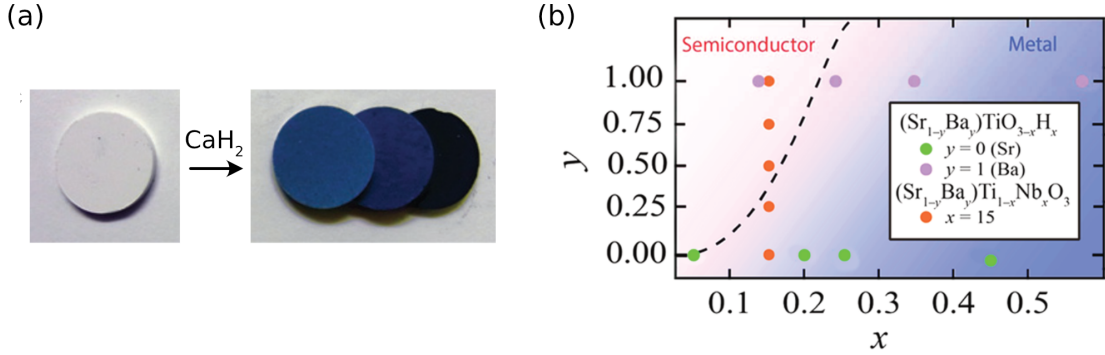


Figure 1.4: (a) Color change after reduction of a BaTiO_3 sample by CaH_2 . The three dark blue pellets are of compositions (from left to right): $\text{BaTiO}_{2.9}\text{H}_{0.1}$, $\text{BaTiO}_{2.7}\text{H}_{0.3}$ and $\text{BaTiO}_{2.5}\text{H}_{0.5}$. Reproduced from [28] with permission from Springer Nature. (b) Electrical properties as a function of the composition in $\text{ATiO}_{3-x}\text{H}_x$ ($A = \text{Ba}, \text{Sr}$) thin films. Data of $\text{Sr}_{1-y}\text{Ba}_y\text{Ti}_{1-x}\text{Nb}_x\text{O}_3$ from [55] (red dots) is included for comparison. Reproduced from [56] with permission. Copyright 2015 American Chemical Society.

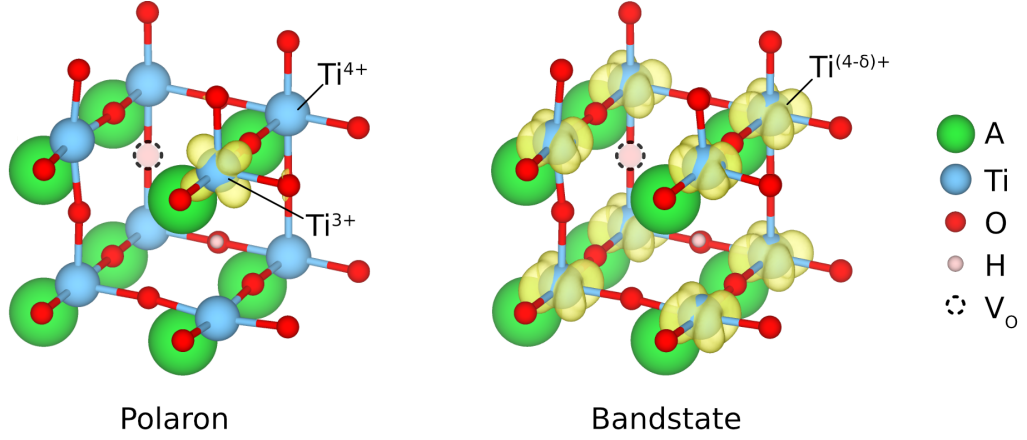


Figure 1.5: Illustration of an electronic polaron and a bandstate in $\text{ATiO}_{3-x-y}\text{H}_x\Box_y$. The yellow isosurfaces indicate the electron density of each specific state.

These findings show that it is challenging to predict electronic behavior in these systems based on their composition. To clarify the electronic structure, various studies have directly probed the presence of bandstates and polarons. For example, diffuse reflectance UV–VIS spectroscopy on $\text{BaTiO}_{3-x-y}\text{H}_x\Box_y$ with $x \approx 0.1$ and $0 < y < 0.38$ suggested that the bottom of the conduction band is occupied, consistent with bandstates [44]. Similarly, solid-state NMR studies on samples with $0.13 < x < 0.31$ concluded that bandstates are prevalent across this range [48].

A particularly relevant investigation by Granhed *et al.* combined DFT calculations and INS experiments to study $\text{BaTiO}_{2.82}\text{H}_{0.1}\Box_{0.08}$ [57]. Their analysis showed that the vibrational spectrum of hydride-ions is sensitive to the presence of nearby polarons, due to the local structural distortion they induce. The experimental data were more consistent with bandstate electrons than with polarons. However, their DFT calculations also revealed that the energy difference between polaron and bandstate configurations is relatively small (-0.15 to 0.12 eV), depending on hydride concentration and computational parameters. Therefore, as also suggested by resistivity measurements, the conclusion that doping electrons always form bandstates cannot be generalized to all compositions of $\text{ATiO}_{3-x-y}\text{H}_x\Box_y$, leaving the question open.

An additional open question concerns a potential coupling between electronic and hydride-ion transport properties. In various transition metal oxides, such as LiV_3O_8 [58] and LiV_2O_5 [59], electron polarons have been shown to significantly affect ionic transport by altering activation barriers. As described throughout this chapter, electronic and ionic transport in $\text{ATiO}_{3-x-y}\text{H}_x\Box_y$ systems have so far been

studied independently.

One of the goals of this thesis is therefore to investigate whether the presence of polarons or bandstates in $ATiO_{3-x-y}H_x\Box_y$ systems influence their hydride-ion transport properties.

This knowledge will provide a more comprehensive understanding of the interplay between electronic and hydride-ion conductivity in oxyhydrides, offering insights into how ionic transport can be tuned by controlling electronic properties, and may be critical for the design of electrochemical devices requiring high ionic conductivity but low electronic conductivity.

1.2 The nitride-hydride Ca_3CrN_3H

1.2.1 Nitride-hydride materials

Systems containing both nitrogen and hydrogen have been studied for several decades, particularly Li–N–H systems, which are known for their relatively high hydrogen storage capacity (up to 11.5 wt%) [60]. However, materials featuring both nitrogen and hydrogen anions, i.e., nitride-hydrides, remain largely unexplored. Until the past decade, only a few such compounds had been reported, including Li_4NH [61], Ca_2NH [62], Ba_2NH [63], and Sr_2NH [63]. More recently, with the advent of mixed-anion chemistry, new compositions have been discovered, such as Sr_2LiH_2N [64], $BaCeO_{3-x}N_yH_z$ [24], and Ba_5CrN_4H [65].

These materials have attracted interest as potential catalysts for ammonia synthesis under mild conditions. Notably, the hydride-ion has been found to play a critical role in systems such as Ca_2NH combined with Ru nanoparticles, in Ba_5CrN_4H , and in $BaCeO_{3-x}N_yH_z$, where it suppresses hydrogen poisoning of Ru surfaces and directly participates as a hydrogen source in the catalytic reaction [19, 24, 65]. These behaviors have been attributed to the high lability of hydride-ions in these compounds.

Of particular relevance to this thesis is the novel nitride-hydride Ca_3CrN_3H , discovered in 2022 by Cao *et al.*, which also exhibits efficient catalytic activity for ammonia synthesis under mild conditions, likely promoted by the mobility of its hydride-ions [29, 66].

1.2.2 Crystal structure

Ca_3CrN_3H can be synthesized *via* a topochemical route by exposing the parent ni-

tride, Ca_3CrN_3 , to H_2 gas at 400 °C [66]. Its crystal structure, refined using powder X-ray diffraction (PXRD), was found to belong to the space group $P6_3/m$ and can be described as a hexagonal X_3BA -type antiperovskite, where $\text{X} = \text{Ca}^{2+}$, $\text{B} = \text{H}^-$, and $\text{A} = [\text{CrN}_3]^{5-}$. The Ca^{2+} ions form face-sharing octahedra along the crystallographic c -axis, each centered by a hydride-ion. These vertically aligned octahedra create unidirectional, channel-like structures hosting the hydride-ions. In the ab -plane, these channels are separated by triangular planar $[\text{CrN}_3]^{5-}$ units (Figure 1.6).

Thermogravimetric and mass spectrometric (TG-MS) analyses revealed that $\text{Ca}_3\text{CrN}_3\text{H}$ remains stable under an inert atmosphere up to approximately 400 °C, at which point it begins to release H_2 gas. Interestingly, PXRD measurements showed that the compound retains its hexagonal structure after dehydrogenation, whereas its parent nitride, Ca_3CrN_3 , originally crystallizes in an orthorhombic structure. Moreover, when the dehydrogenated hexagonal Ca_3CrN_3 is re-exposed to H_2 gas at 400 °C, it reversibly converts back to $\text{Ca}_3\text{CrN}_3\text{H}$ [66]. These results therefore indicate that the hydrogen-free hexagonal phase is structurally robust and suggest that partial hydride-ion site occupancy in $\text{Ca}_3\text{CrN}_3\text{H}$ may be possible.

However, due to the low X-ray scattering power of hydrogen, the PXRD patterns of $\text{Ca}_3\text{CrN}_3\text{H}$ and hexagonal Ca_3CrN_3 are nearly indistinguishable, making it difficult to determine the hydride-ion content or its local coordination environment directly. In fact, Rietveld refinement of the PXRD data, combined with TG-MS analysis, suggested that $\text{Ca}_3\text{CrN}_3\text{H}$ is nonstoichiometric and better described by the formula $\text{Ca}_3\text{CrN}_3\text{H}_x$, where x lies between 0.7 and 1.

One of the goals of this thesis is therefore to investigate the local coordination environment of the hydride-ions in $\text{Ca}_3\text{CrN}_3\text{H}$ and to reduce the uncertainty surrounding their exact concentration.

This knowledge will be essential for elucidating the hydride-ion transport properties of the material and understanding the role of hydride-ions in its catalytic behavior.

1.2.3 Hydride-ion transport and catalytic properties

$\text{Ca}_3\text{CrN}_3\text{H}$ exhibits catalytic ammonia synthesis activity, i.e., $\text{N}_2 + 3 \text{H}_2 \longrightarrow 2 \text{NH}_3$, without the need for metallic nanoparticles. Its synthesis rate was measured at 865 $\mu\text{mol/g/h}$ at ambient pressure and 400°C, comparable to traditional catalysts such as $\text{Co}_3\text{Mo}_3\text{N}$ (796 $\mu\text{mol/g/h}$), $\text{Fe-K}_2\text{O-Al}_2\text{O}_3$ (330 $\mu\text{mol/g/h}$), and Ru-Ba/C (148 $\mu\text{mol/g/h}$) [14, 29]. As discussed below, this notable catalytic performance may be closely linked to the hydride-ion transport properties of the material.

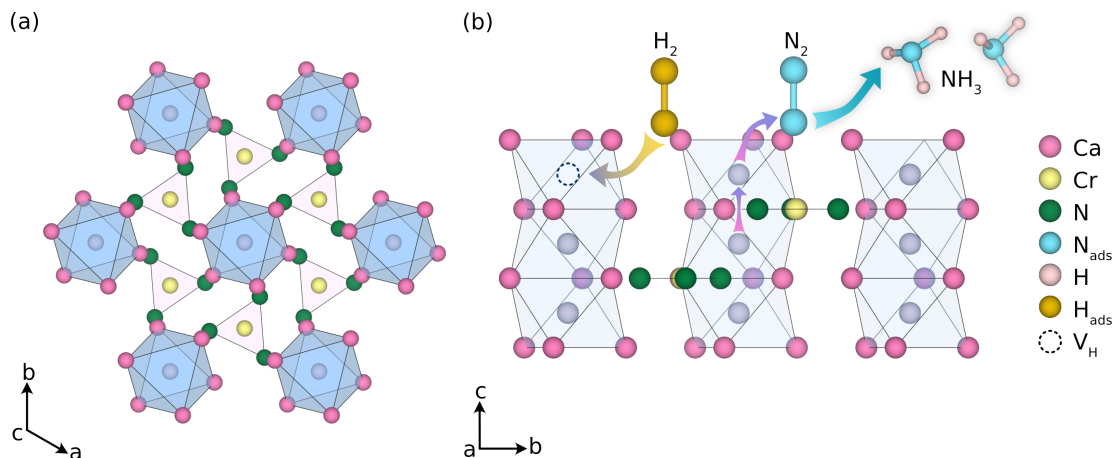


Figure 1.6: Crystal structure and ammonia synthesis mechanism of $\text{Ca}_3\text{CrN}_3\text{H}$. (a) Crystal structure of $\text{Ca}_3\text{CrN}_3\text{H}$, viewed along the c -axis. (b) Crystal structure of $\text{Ca}_3\text{CrN}_3\text{H}$, viewed along the a -axis, with a schematic illustration of the catalytic ammonia synthesis mechanism proposed by Cao *et al.* [29].

As with oxyhydrides, the first hint of hydride-ion mobility in $\text{Ca}_3\text{CrN}_3\text{H}$ came from the observation of H_2 release at 400 °C. H/D exchange experiments were conducted, and approximately 60% of the hydride-ions were replaced by deuterium anions, demonstrating that even bulk hydride-ions, and not only surface hydride-ions, are mobile and may participate in the catalytic turnover. Indeed, the H/D exchange rate was found to be significantly higher than the rate of ammonia synthesis: the hydride-ion turnover frequency was measured at 275.4 s^{-1} , compared to 2.1 s^{-1} for ammonia production. This suggests that during catalysis, hydride-ion sites within the lattice are continuously and rapidly replenished, thus establishing a key role for mobile hydride-ions in delivering hydrogen to surface N_2 species [29].

Further insight into this process was obtained through DFT investigations of the reaction mechanism. The reaction was found to follow an associative pathway, in which the N_2 molecule undergoes stepwise hydrogenation prior to cleavage of the $\text{N} \equiv \text{N}$ triple bond. Crucially, the hydrogen required to form N_2H originates from the lattice rather than $\text{H}_2(\text{g})$. The resulting hydride-ion vacancy is subsequently replenished either by migration of another lattice hydride-ion or by incorporation of a hydrogen atom from the gas phase [see Figure 1.6(b), and Appendix A for details]. This mechanism is characteristic of a Mars–van Krevelen process.

Together, these results have underscored the central role of hydride-ion transport in enabling the catalytic activity of $\text{Ca}_3\text{CrN}_3\text{H}$, but the detailed mechanism by

which hydride-ions migrate within the structure remains unknown.

One of the goals of this thesis is therefore to investigate the mechanism of hydride-ion transport in $\text{Ca}_3\text{CrN}_3\text{H}$.

This knowledge will contribute to the understanding of the catalytic mechanisms of the material and provide guidance for its application as a catalyst for ammonia synthesis, including strategies to optimize its performance.

Chapter 2

Neutron scattering¹

2.1 Concepts of nuclear scattering

2.1.1 About neutrons

Neutrons are quantum particles characterized by several key physical properties: mass, momentum, kinetic energy, wavelength, frequency, and spin. A particularly important feature is that neutrons are electrically neutral. Because they carry no electric charge, they do not interact with electron clouds and can penetrate deeply into materials (typically several centimeters). Specifically, neutrons interact with atomic nuclei *via* the strong nuclear force. This makes them ideal probes for investigating the bulk properties of matter in a non-destructive way. In contrast, X-rays are scattered by electrons and typically penetrate much less deeply, on the order of 10^{-2} to 10^{-5} cm. Note that neutrons carry a magnetic dipole moment and can interact with the magnetic moment of unpaired electron, but magnetic neutron scattering was not used in this thesis and will not be discussed further.

In scattering experiments neutrons typically have wavelengths in the range of 1–10 Å, which conveniently matches typical interatomic distances in solids. Larger wavelengths of this range correspond to the so-called *cold neutrons*.² Wavelengths near ~ 2 Å correspond to *thermal neutrons*.³ Shorter wavelengths correspond to more energetic *hot neutrons*.⁴ This wavelength range allows neutrons to produce

¹This chapter is partly based on my Licentiate thesis [67], and on the textbook references [68, 69].

²Cold neutrons have kinetic energies in the range of 0–26 meV.

³A thermal neutron is in equilibrium with a thermal bath at room temperature, $T = 300$ K, and has a kinetic energy of $E \approx k_B T \approx 26$ meV.

⁴Hot neutrons have kinetic energies in the range of 26–500 meV.

constructive and destructive interference when scattered by a crystal lattice, resulting in *Bragg peaks*. This phenomenon, known as diffraction, provides detailed information about the atomic structure of materials. In addition to structural information, neutrons can also probe atomic and molecular dynamics. Because their kinetic energies are on the order of thermal excitations in solids, neutrons can gain or lose energy by interacting with vibrational modes (phonons) or other excitations in the sample. This energy exchange can be measured, enabling the study of dynamic processes such as lattice vibrations, molecular rotations, and diffusion. This technique is called neutron spectroscopy and is discussed in more details below.

Finally, neutrons have a spin angular momentum of $\pm \frac{1}{2}\hbar$. During scattering, the neutron spin may flip ($+\frac{1}{2}\hbar \rightarrow -\frac{1}{2}\hbar$ or vice versa), and analyzing of such spin-flip processes can yield additional information about the nature of the neutron-sample interaction. For example, in this thesis, spin-flip analysis was specifically employed to distinguish the contributions from hydride-ions from those of other atomic species.

2.1.2 Scattering kinematics

Neutrons are quantum particles, and an incident monochromatic neutron beam is described by a wave function: $\Psi(\mathbf{r}) = A \exp(i\mathbf{k}_i \cdot \mathbf{r})$, where \mathbf{k}_i is the incident neutron wavevector (related to its wavelength λ_i by $k_i = 2\pi/\lambda_i$), and A is a normalization factor. In this formalism, $|\Psi(\mathbf{r})|^2 dV$ represents the probability of finding the neutron within the volume element dV at position \mathbf{r} , highlighting its wave-particle dual nature. After scattering by a nucleus, the neutron wave function becomes a spherical wave: $\Psi_{sc}(\mathbf{r}) = -Ab/r \exp(ik_f r)$. Here, b , the *bound scattering length*, quantifies the strength of the interaction between the neutron and the nucleus. It has the dimension of length and can take positive or negative values. In general, b is a complex quantity: its real part governs scattering processes, while its imaginary part is associated with neutron absorption by the nucleus. Far from the nucleus and after the scattering event, the spherical wavefront can be approximated by a plane wave with a scattered wavevector \mathbf{k}_f forming an angle θ with the incident wavevector \mathbf{k}_i (see Figure 2.1). The scattering vector is defined as:

$$\mathbf{Q} = \mathbf{k}_i - \mathbf{k}_f, \quad (2.1)$$

which relates to the *momentum transfer* between the neutron and the sample, given by $\hbar\mathbf{Q}$. The energy transferred from the incident neutron to the sample is:

$$\hbar\omega = E_i - E_f = \frac{\hbar^2 k_i^2}{2m_n} - \frac{\hbar^2 k_f^2}{2m_n}, \quad (2.2)$$

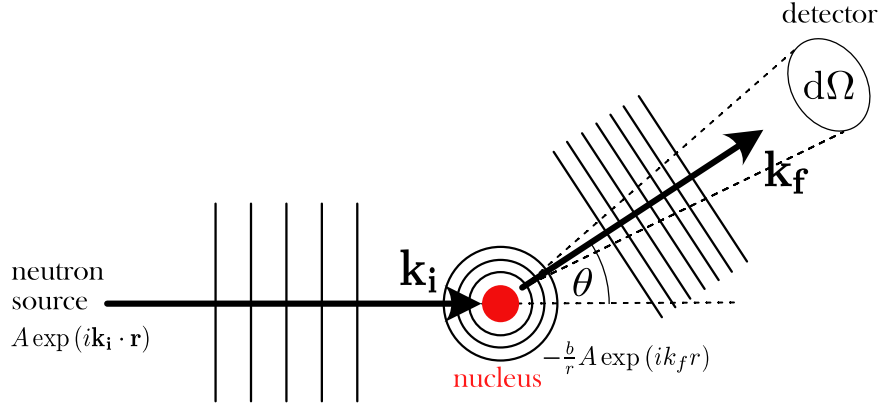


Figure 2.1: Schematic description of a neutron scattering process by a single nucleus. The vertical lines perpendicular to \mathbf{k}_i and \mathbf{k}_f , and the circles around the nucleus represent the wavefronts. $d\Omega$ is the solid angle covered by the detector.

where m_n is the neutron mass. If $\hbar\omega = 0$, the scattering is called *elastic*; if $\hbar\omega \neq 0$, it is referred to as *inelastic* scattering. Combining eq. (2.1) and (2.2), one gets

$$Q^2 = k_i^2 + k_f^2 - 2k_i k_f \cos \theta = \frac{2m_n}{\hbar^2} (2E_i - \hbar\omega - 2\sqrt{E_i(E_i - \hbar\omega)} \cos \theta) \quad (2.3)$$

Therefore, momentum and energy transfer are not independent quantities. In a neutron scattering experiment, one must fix either E_i or E_f , and, as a result, eq. (2.2) imposes a constraint on the accessible $(Q, \hbar\omega)$ space (see Figure 2.2).

2.1.3 Dynamical structure factor

The neutron flux in a detector solid angle $d\Omega$ and with a final energy comprised between $E_f + dE_f$ is represented by the so-called *partial differential scattering cross section*, $d^2\sigma/d\Omega dE_f$, which is proportional to the *dynamical structure factor*⁵, $S(\mathbf{Q}, \omega)$:

$$\frac{d^2\sigma}{d\Omega dE_f} = \frac{k_f}{k_i} S(\mathbf{Q}, \omega) \quad (2.4)$$

$S(\mathbf{Q}, \omega)$ is a fundamental property of the sample and, in principle, is independent of the instrument geometry and the incident neutron wavelength.⁶ Physically, $S(\mathbf{Q}, \omega)$

⁵Sometimes referred to as *scattering function* or *scattering law*.

⁶However, in practice, instrumental effects arising from geometry, resolution, and detector efficiency, can influence the measured signal.

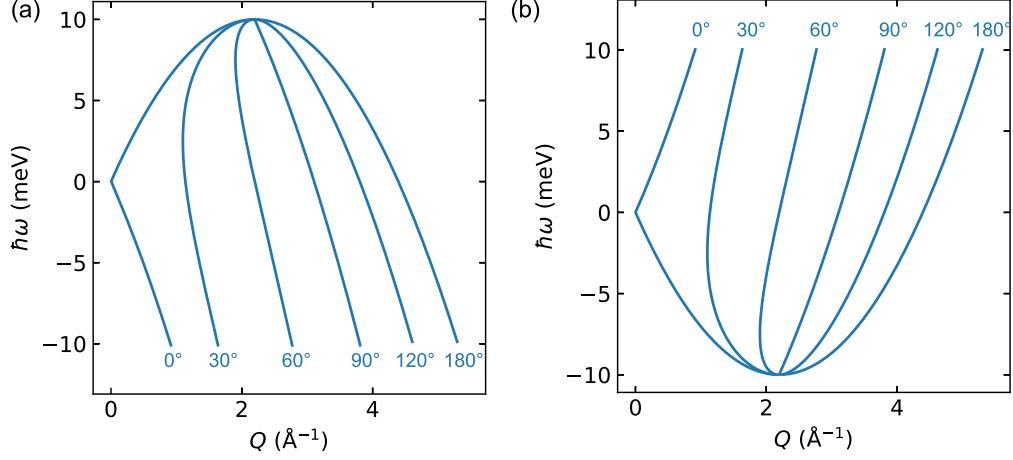


Figure 2.2: Accessible dynamic range for a scattered neutron with fixed E_i or E_f . (a) Eq. (2.3) plotted for $E_i = 10$ meV at selected scattering angles θ . (b) Eq. (2.3) plotted for $E_f = 10$ meV at the same angles.

acts as a response function: it characterizes how the system responds to the perturbation introduced by the neutron probe. More specifically, it provides information about the space- and time-dependent correlations in atomic positions due to spontaneous fluctuations occurring in the system. In the formalism introduced by van Hove, this response function is expressed as:

$$S(\mathbf{Q}, \omega) = \frac{1}{2\pi\hbar} \sum_{j,k} \overline{b_k b_j} \int_{-\infty}^{\infty} \left\langle \exp(-i\mathbf{Q} \cdot \mathbf{r}_j(0)) \exp(i\mathbf{Q} \cdot \mathbf{r}_k(t)) \right\rangle \exp(-i\omega t) dt, \quad (2.5)$$

where $\overline{b_j}$ is the bound scattering length of atom j (the bar represents an isotope and spin average), $\mathbf{r}_j(t)$ is the position in space of atom j at time t , and $\langle \dots \rangle$ represents a thermal average.

2.1.4 Coherent and incoherent scattering

As seen in eq. (2.5), $S(\mathbf{Q}, \omega)$ includes an average over scattering lengths, $\overline{b_k b_j}$. This is because the scattering length depends on the isotope and, in some cases, on the nuclear spin state. In practice, a material typically contains a natural isotopic mixture, where isotopes are randomly distributed throughout the sample. Since different isotopes have different scattering lengths, neutrons are scattered with varying amplitudes from atom to atom. These random variations alter the interference conditions and introduce a background in the scattering pattern. This effect

is known as *isotopic-incoherent scattering*. Similarly, due to the neutron spin of $\pm\frac{1}{2}$, the scattering length of a nucleus with spin S depends on the total spin state of the neutron-nucleus system, which can be either $S + \frac{1}{2}$ or $S - \frac{1}{2}$. In a sample, the orientations of nuclear spins are typically randomly distributed and therefore the scattering length varies depending on each spin configuration. This randomness, analogous to the case of isotopic disorder, leads to *spin-incoherent scattering*.

Assuming a random distribution of isotopes and spin orientations, $\overline{b_k b_j}$ can be simplified by:

$$\begin{aligned}\overline{b_k b_j} &= \overline{|b_j|^2} \text{ if } j = k, \\ &= \overline{b_k} \overline{b_j} \text{ if } j \neq k,\end{aligned}\tag{2.6}$$

and eq. (2.5) can be rewritten as a sum of *coherent* and an *incoherent* contribution defined as:

$$S_{\text{coh}}(\mathbf{Q}, \omega) = \frac{1}{2\pi\hbar} \sum_{j,k} \overline{b_k} \overline{b_j} \int_{-\infty}^{\infty} \left\langle \exp(-i\mathbf{Q} \cdot \mathbf{r}_j(0)) \exp(i\mathbf{Q} \cdot \mathbf{r}_k(t)) \right\rangle \exp(-i\omega t) dt \tag{2.7}$$

and

$$\begin{aligned}S_{\text{inc}}(\mathbf{Q}, \omega) &= \frac{1}{2\pi\hbar} \sum_j (\overline{|b_j|^2} - |\overline{b_j}|^2) \int_{-\infty}^{\infty} \left\langle \exp(-i\mathbf{Q} \cdot \mathbf{r}_j(0)) \exp(i\mathbf{Q} \cdot \mathbf{r}_j(t)) \right\rangle \\ &\quad \times \exp(-i\omega t) dt\end{aligned}\tag{2.8}$$

Although purely mathematical, incoherent and coherent scattering have a physical interpretation, as illustrated in Figure 2.3. Eq. (2.7) shows that coherent scattering depends on the average scattering length \overline{b} and eq. (2.8) shows that incoherent scattering arises from deviations from this average (note that this includes both isotope and spin incoherence). Notably, it can be seen that incoherent scattering arises from the self-correlation of the position of each individual nucleus at different times, while coherent scattering includes both self-correlations and pair-correlations between the positions of different nuclei. It means that incoherent scattering provides information about individual atomic motions, regardless of their spatial arrangement, while coherent scattering reflects collective behaviors, such as the periodic structure of a crystal and its collective vibrational modes.

In practice, the isotope- and spin-averaged bound scattering length of each element is tabulated and provided in terms of coherent and incoherent *cross sections*, defined as $\sigma_{\text{inc}} = 4\pi(\overline{|b|^2} - |\overline{b}|^2)$ and $\sigma_{\text{coh}} = 4\pi|\overline{b}|^2$. Cross sections have the dimension of area and are typically given in units of barn (where 1 barn = 10^{-28} m²).

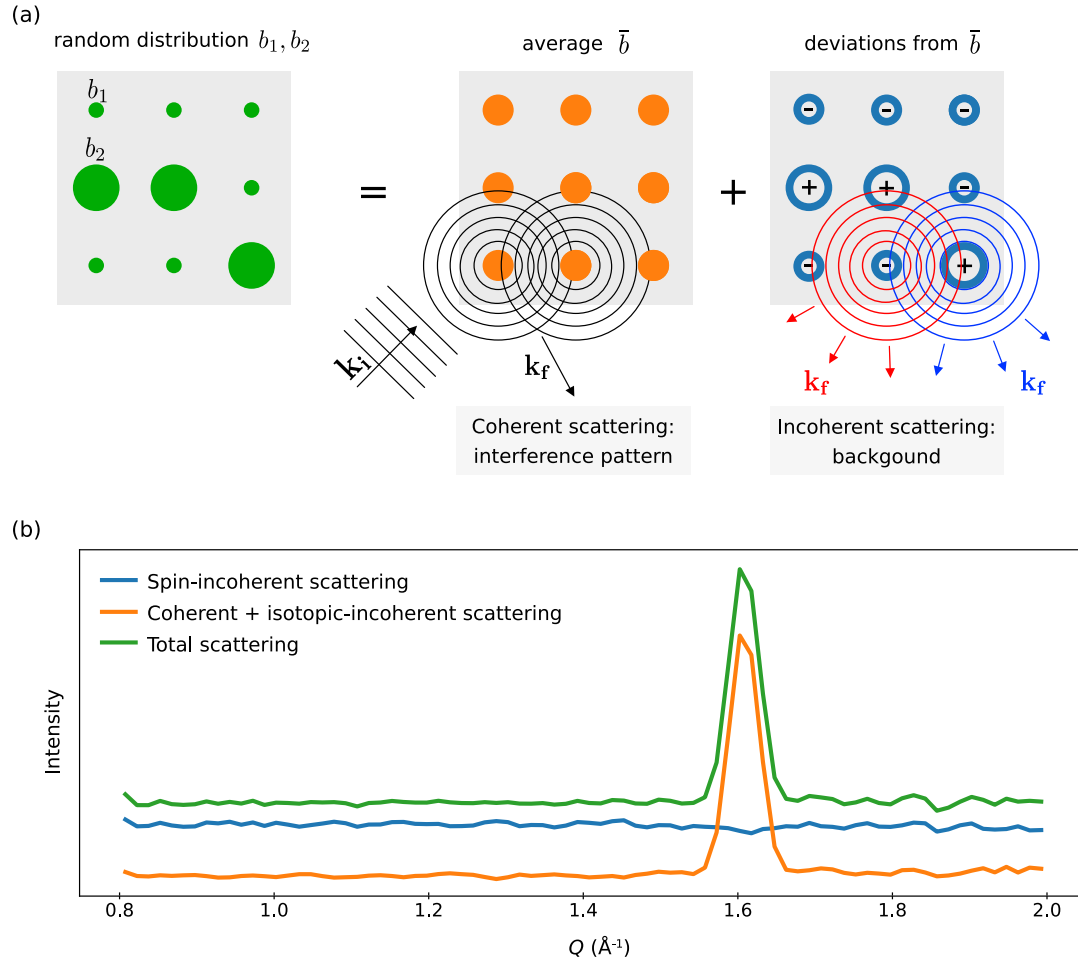


Figure 2.3: Illustration of coherent and incoherent scattering. (a) A random distribution of two scattering lengths, b_1 and b_2 , can be decomposed into an average value \bar{b} and deviations from that average. \bar{b} gives rise to coherent scattering, while the deviations contribute to incoherent scattering. (b) Elastic scattering profile of a powder sample of $\text{SrTiO}_{2.8}\text{H}_{0.13}\square_{0.07}$, measured on the LET spectrometer at the ISIS Pulsed Neutron and Muon Source. The signal is separated into coherent and spin-incoherent components.

The case of hydrogen

Hydrogen has the largest incoherent scattering cross section of any element, of 80.26 barns, along with a relatively small coherent cross section of 1.757 barns. Notably,

hydrogen has three isotopes: ^1H , ^2H (deuterium), and ^3H (tritium), with respective relative abundances of 99.985%, 0.015%, and a negligible amount of tritium. Due to the predominance of ^1H , the incoherent cross section of hydrogen arises almost entirely from spin-incoherence. While incoherent scattering was described in the previous paragraphs as a background in the scattering pattern, hindering the Bragg peak analysis, it is particularly useful for the study of oxide- and nitride-hydride systems, for two main reasons. First, the very large total cross section of hydrogen makes neutrons highly sensitive to the presence of hydride-ions, allowing their scattering signal to be detected even at low concentrations. Second, the small coherent cross section implies that the scattered intensity originates predominantly from individual hydride-ions rather than from their spatial distribution. This enables the probing of their self-diffusive motions, for example, *via* quasi-elastic neutron scattering.

2.1.5 Uniaxial polarization analysis

Because incoherent scattering from hydrogen arises from spin-incoherence, it can be separated from the coherent scattering contribution by using polarized neutron beams. This separation is particularly useful for distinguishing scattering from hydride-ions from that of other species, which may complicate data analysis. Uniaxial polarization analysis for non-magnetic samples exploits the neutron spin–nuclear spin interaction by measuring whether the neutron spin flips upon interaction with the sample. Crucially, coherent (coh) and isotopic-incoherent (iso) scattering do not flip the spin state of an incident neutron, while spin-incoherent (spin) scattering does. Formally, the neutron scattering intensities associated with spin-flip (SF) and non-spin-flip (NSF) processes obey to:

$$\begin{aligned} I_{\text{NSF}} &= I_{\text{coh}} + I_{\text{inc}}^{\text{iso}} + \frac{1}{3} I_{\text{inc}}^{\text{spin}} \\ I_{\text{SF}} &= \frac{2}{3} I_{\text{inc}}^{\text{spin}} \end{aligned} \tag{2.9}$$

In an experiment using uniaxial polarization analysis, the incident neutron beam is polarized along an axis x , meaning the neutron spin orientation is selected, e.g., the $+\frac{1}{2}$ orientation along x . The polarization of the scattered beam is then analyzed along this same axis in terms of SF and NSF events, i.e, the number of scattered neutron with $+\frac{1}{2}$ and $-\frac{1}{2}$ are counted separately. The coherent plus isotopic-incoherent and spin-incoherent intensities are subsequently separated using eqs. (2.9). For example, see Figure 2.3(b).

2.2 Inelastic neutron scattering

INS investigates neutron-sample interactions that involve an exchange of energy. A neutron energy gain ($\hbar\omega < 0$) corresponds to an energy loss by the sample, whereas a neutron energy loss ($\hbar\omega > 0$) indicates a gain in sample energy (see Figure 2.4). INS thus probes the vibrational excitation states of materials, and is very complementary to infrared and Raman spectroscopy because that there are no selection rules in INS, allowing all modes to be seen.

The typical vibrational motions probed by INS in condensed matter lie in the energy range of 1–500 meV. These correspond to small-amplitude oscillatory motions (relative to interatomic distances) of atoms around their equilibrium positions. In oxide- and nitride-hydride materials, INS reveals both collective atomic vibrations, referred to as *phonons*, and localized vibrational modes associated with hydride-ions. This section provides a brief overview of the vibrational dynamics of hydride-ions in oxide- and nitride-hydride systems.

2.2.1 Localized vibrations of hydride-ions

In $\text{BaTiO}_{3-x}\text{H}_x$, hydride-ions are randomly distributed over the oxygen sub-lattice and are present at relatively low concentrations. As a result, they do not interact with each other, and their vibrational dynamics can be approximated as those of independent harmonic oscillators. This approximation places the study of hydride-ions vibrational modes in $\text{BaTiO}_{3-x}\text{H}_x$ within the framework of *molecular spectroscopy*, which is typically used to probe localized, non-collective vibrational modes in molecular systems.

Dynamical structure factor

The harmonic potential trapping the hydride-ions can be considered as anisotropic, such as each hydride-ion has 3 distinct fundamental vibrational modes with fundamental frequency ω_0^x , ω_0^y , ω_0^z . The dynamical structure factor, $S(\mathbf{Q}, \omega)$ is thus featured by sharp peaks at $\omega = p\omega_0^x$, $p\omega_0^y$, and $p\omega_0^z$, with p the transition order. $p = 1$ is the *fundamental transition*, and $p = 2, 3, \dots$ are *higher-order transitions*.

The intensity of each mode $\nu = x, y, z$ is proportional to:

$$S(\mathbf{Q}, \omega_\nu)_p \propto \frac{\sigma_{tot,H}}{4\pi} \exp(-[\mathbf{Q} \cdot \sum_{\nu=\{x,y,z\}} \mathbf{u}_\nu]^2) \frac{[\mathbf{Q} \cdot \mathbf{u}_\nu]^{2p}}{p!} \quad (2.10)$$

where \mathbf{u}_ν is the root mean square displacement vector of the mode ν .

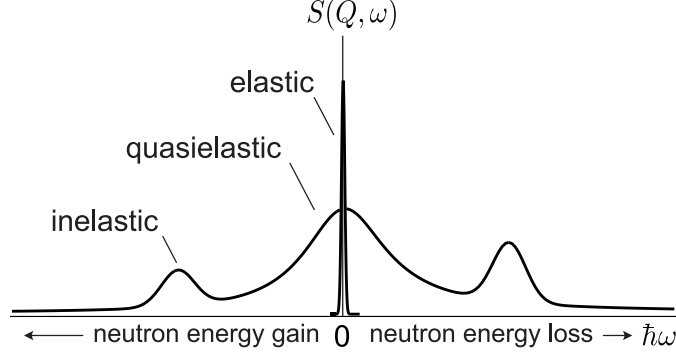


Figure 2.4: Illustration of the dynamical structure factor measured in a neutron scattering experiment. Adapted from ref. [68] with permission of The Licensor through PLSclear.

Note that $\text{BaTiO}_{3-x}\text{H}_x$ is synthesized in powder form; therefore, the measured INS intensity corresponds to the powder-averaged form of eq. (2.10), which is given by:

$$S(Q, \omega_\nu)_p \approx \frac{\sigma_{\text{tot,H}}}{4\pi} \exp(-Q^2 \alpha_\nu^{(p)}) \frac{[Qu_\nu]^{2p}}{p!} \quad (2.11)$$

where u_ν is the square mean square displacement (MSD) of mode ν , and $\alpha_\nu^{(p)}$ is a coefficient related to the transition order:

$$\alpha_\nu^{(1)} = \frac{1}{5}(u^2 + 2u_\nu^2) \quad \text{and} \quad \alpha_\nu^{(2)} = \frac{1}{7}(u^2 + 4u_\nu^2) \quad (2.12)$$

with $u^2 = u_{\nu_x}^2 + u_{\nu_y}^2 + u_{\nu_z}^2$, the total MSD.

Note that the term $\exp(-Q^2 \alpha_\nu^{(p)})$ in eq. (2.11) is known as the *Debye–Waller factor*. This factor decreases with increasing Q and with increasing MSD u^2 . Physically, it reflects the effect of thermal fluctuations of the hydride-ions, which, instead of appearing as a point-like scatterers, are seen as a spatially diffuse objects. This thermal motion reduces the coherent scattered intensity, and the effect becomes more pronounced at higher temperatures, as u^2 increases with temperature.

Since localized vibrational modes are non-dispersive, that is, ω_ν does not depends on Q , neutron spectrometers can be specifically optimized for molecular spectroscopy by integrating neutron counts over a wide range of momentum transfers Q and analyzing only their energy distribution. These spectrometers, such as LAGRANGE at the ILL, produce a Q -independent spectrum, $S(\omega)$. Figure 2.5 shows an example of such an INS spectrum obtained for a powder sample of $\text{BaTiO}_{2.9}\text{H}_{0.1}$.

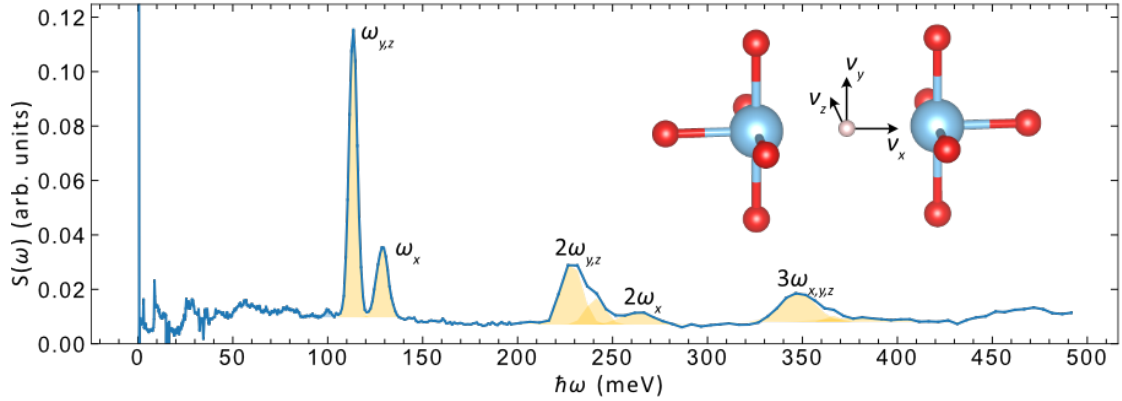


Figure 2.5: INS spectrum of a powder sample of $\text{BaTiO}_{2.9}\text{H}_{0.1}$ as measured on LA-GRANGE at the ILL. Hydrogen peaks are fitted (shaded areas) and the corresponding vibrational modes are assigned. Inset: illustration of the directions of the three vibrational modes in $\text{BaTiO}_{3-x}\text{H}_x$. The fundamental modes, first, and second overtones of hydride-ion vibrations can be identified at 120 meV, 230 meV, and 350 meV.

2.2.2 Collective vibrations of hydride-ions

In $\text{Ca}_3\text{CrN}_3\text{H}$, hydride-ions are arranged in linear chains along the crystallographic c -axis (see Section 1.2) and, in contrast to $\text{BaTiO}_{3-x}\text{H}_x$, cannot be treated as independent harmonic oscillators due to their mutual interactions. Instead, their coupled vibrations within harmonic potentials give rise to a set of collective modes known as *phonons*, states of motion in which all atoms oscillate coherently at the same frequency.⁷ In contrast to localized vibrations, phonons are generally dispersive, that is, the mode frequencies depend on \mathbf{Q} and are related through a *dispersion relation*, denoted $\omega(\mathbf{Q})$. Thus, instead of being featured by sharp peaks, as it is the case of localized vibration, $S(\mathbf{Q}, \omega)$ generally shows a continuum in intensity characteristic of the dispersion relation. When $\omega(\mathbf{Q} = 0) = 0$ and increases with increasing Q , the corresponding phonon mode is referred to as an *acoustic* mode. In contrast, if $\omega(\mathbf{Q} = 0)$ has a finite value, the phonon mode is called an *optical* mode. Figure 2.6(a) schematically illustrates a typical phonon dispersion relation featuring one acoustic and one optical branch. Note that the frequencies of optical modes generally exhibit a weaker \mathbf{Q} -dependence compared to those of acoustic modes, and they often appear as localized peaks in the INS spectrum, within the limits of the instrumental resolution. In $\text{Ca}_3\text{CrN}_3\text{H}$, the acoustic modes correspond to in-phase oscillations of all

⁷The formalism of phonons is not described here, details can be found in [68].

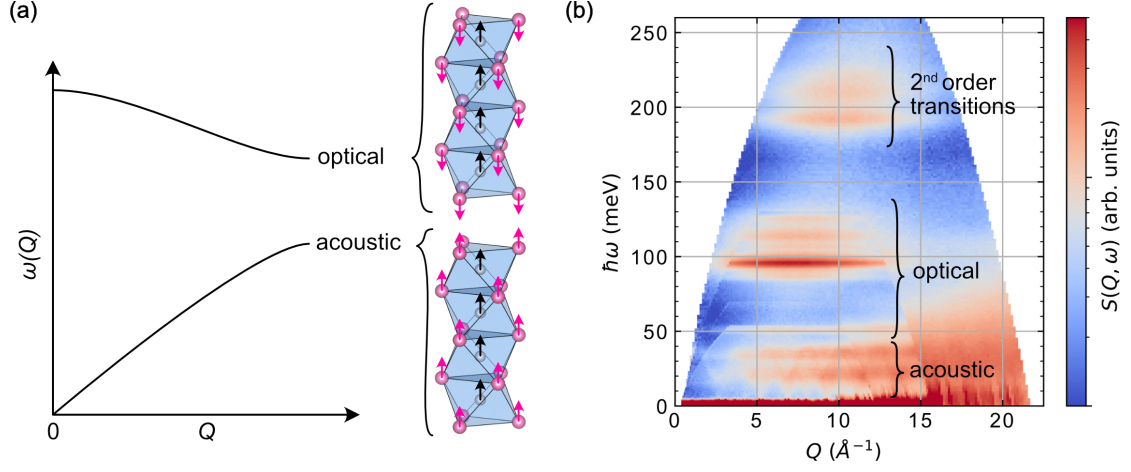


Figure 2.6: Optical and acoustic phonons in $\text{Ca}_3\text{CrN}_3\text{H}$. (a) Schematic phonon dispersion relation together with illustration of representative optical and acoustic modes in $\text{Ca}_3\text{CrN}_3\text{H}$. Pink and gray spheres indicate Ca and H, respectively. Arrows indicate the displacement direction of atoms at the same instant. (b) INS spectrum of a powder sample of $\text{Ca}_3\text{CrN}_3\text{H}$ measured with 4SEASONS at J-PARC.

ions, within an energy range between 0 and 50 meV. In contrast, the typical optical modes involve out-of-phase vibrations between the hydride-ions and calcium ions, with energies ranging from 90 to 130 meV, as shown in Figure 2.6.

Dynamical structure factor

Since $\text{Ca}_3\text{CrN}_3\text{H}$ is synthesized in powder form, only the powder-averaged dynamical structure factor, $S(Q, \omega)$, can be measured. Moreover, at relatively large Q —that is, when $Q \gg 2\pi/d$, with d being the nearest-neighbor distance—the coherent scattering intensity becomes smoothed out due to the finite Q resolution of the instrument. In this condition, interatomic interference effects can be neglected, and each atom can be treated as scattering independently of the others. This is known as the incoherent approximation, which significantly simplifies the expression of $S(Q, \omega)$, and it can be written as:

$$S(Q, \omega) = \sum_a \frac{\sigma_{\text{tot},a}}{4\pi} \frac{Q^2}{3m_a} \exp(-2W_a) \frac{\text{PDOS}_a(\omega)}{2\omega} (n(\omega) + 1), \quad (2.13)$$

where a indexes the atoms, m_a is the atomic mass, and $2W_a = Q^2 u_a^2$ is the Debye-Waller exponent, with u_a^2 being the MSD of atom a . $\text{PDOS}_a(\omega)$ denotes

the partial vibrational density of states associated with atom a , and $n(\omega) = 1/[\exp(\hbar\omega/k_{\text{B}}T) - 1]$ is the Bose–Einstein phonon occupation factor. Note that eq. (2.14) resembles eq. (2.11), but it is defined for any frequency ω , rather than for discrete modes ω_ν . Crucially, the PDOS, which is specific to each material, reflects both the relative intensity of different phonon modes and the contribution of each atom to each mode. It is defined as the number of phonon modes within the frequency range ω to $\omega + d\omega$. In practice, an INS measurement cannot distinguish between the different atomic contributions to $S(Q, \omega)$, and rather measures a so-called *generalized density of state* (GDOS), $G(\omega)$, defined as:

$$S(Q, \omega) = G(\omega) \frac{Q^2}{2\omega} (n(\omega) + 1), \quad (2.14)$$

with

$$G(\omega) = \sum_a \frac{\sigma_{\text{tot},a}}{4\pi} \frac{\exp(-2W_a)}{3m_a} \text{PDOS}_a(\omega). \quad (2.15)$$

The GDOS is the key quantity measured in an INS experiment, as it encapsulates the vibrational properties of the material. It can be computed relatively easily, as outlined in Chapter 4.

2.3 Quasielastic neutron scattering

QENS is a specific case of inelastic scattering that occurs when a system undergoes random rearrangements between configurations of equal energy. In oxide- and nitride-hydride systems, QENS typically arises from the stochastic diffusional motion of hydride-ions. This process produces a characteristic broadening at the base of the elastic peak (see Figure 2.4), which is inversely proportional to the characteristic timescale τ of the fluctuations, i.e., $\propto 1/\tau$, and thus requires high energy resolution for proper detection.

Due to the large incoherent cross section of hydrogen, hydride-ion diffusion is typically observed in $S_{\text{inc}}(Q, \omega)$, which reflects single-particle, or self-diffusion, of hydride-ions. In practice, a QENS spectrum is analyzed by fitting $S_{\text{inc}}(Q, \omega)$ with a physically motivated diffusion model. Typical models used for oxide- and nitride-hydride systems include long-range (translational) jump-diffusion and localized (spatially restricted) jump-diffusion. Both models are described below.

2.3.1 Long-range diffusion

In oxide- and nitride-hydride systems, long-range diffusion of hydride-ions occurs *via* consecutive and random jumps between stable sites, where the residence time τ at a site is much longer than the time required for a jump. A simple model developed by Chudley and Elliott is well suited to describe such diffusional behavior [70]. In this model, the jump distance d is fixed, and the dynamical structure factor for a powder sample is given by:

$$S_{\text{inc}}(Q, \omega) = \frac{1}{\pi} \frac{\hbar\Gamma(Q)}{(\hbar\omega)^2 + (\hbar\Gamma(Q))^2}, \quad (2.16)$$

with

$$\Gamma(Q) = \frac{1}{\tau} \left(1 - \frac{\sin(Qd)}{Qd} \right) \quad (2.17)$$

As can be seen in eq. (2.16), $S_{\text{inc}}(Q, \omega)$ is a Lorentzian function of full-width at half-maximum in energy (FWHM) $2\hbar\Gamma(Q)$, and eq.(2.17) shows how the broadening is related to the microscopic diffusion parameters τ and d . Figure 2.7(a) illustrates the evolution of a Lorentzian's FWHM according to the Chudley-Elliott model.

Note that long-range diffusion, as probed by QENS, extends over characteristic distances on the order of the inverse of the minimum momentum transfer, i.e., $r_{\text{max}} \propto 2\pi/Q_{\text{min}}$. QENS spectrometers typically have $Q_{\text{min}} \approx 0.3 \text{ \AA}^{-1}$, corresponding to $r_{\text{max}} \approx 20 \text{ \AA}$, which is on the scale of a few unit cells.

2.3.2 Localized diffusion

Oxide- and nitride-hydride systems can also exhibit spatially restricted, localized hydride-ion diffusion. This occurs when hydride ions can only jump between a limited number of available sites. In the simplest case, they undergo back-and-forth jumps between two sites separated by a distance d , with an average residence time τ at each site. The dynamical structure factor for a powder sample is given by:

$$S_{\text{inc}}(Q, \omega) = \frac{1}{2} \left(1 + \frac{\sin(Qd)}{Qd} \right) \delta(\hbar\omega) + \frac{1}{2} \left(1 - \frac{\sin(Qd)}{Qd} \right) \frac{1}{\pi} \frac{2\hbar/\tau}{(\hbar\omega)^2 + (2\hbar/\tau)^2} \quad (2.18)$$

Note the Dirac delta function in eq.(2.18), which is absent in eq.(2.16). It reflects a non-zero probability of finding the hydride-ion at either of the two sites even after infinite time, in contrast to long-range diffusion. A Lorentzian function describes the quasielastic signal, as in eq. (2.16), with the notable difference of a constant FWHM over Q . The FWHM is related to τ as $\text{FWHM} = 4\hbar/\tau$.

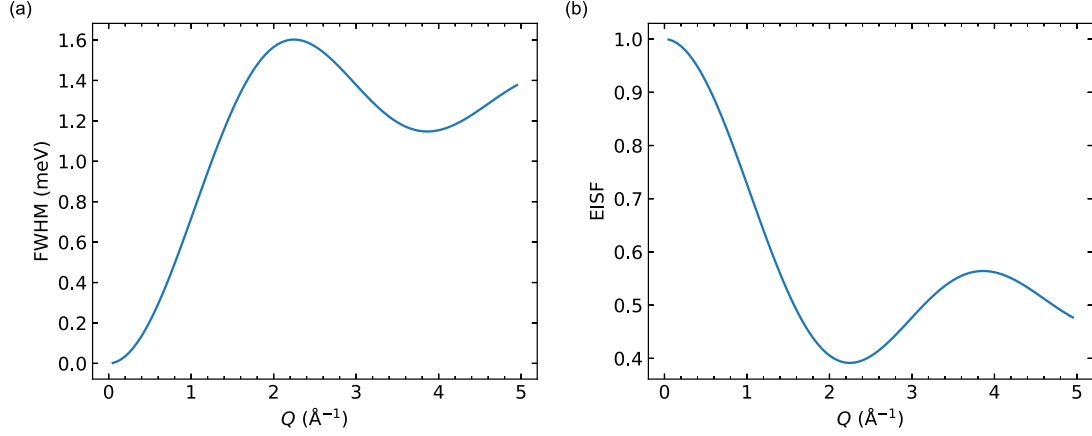


Figure 2.7: Theoretical models associated with long-range and localized jump-diffusion. (a) FWHM from the Chudley-Elliott model [eq. (2.17)] for $d = 2 \text{ \AA}$ and $\tau = 1 \text{ ps}$. (b) EISF from the jump model over two sites for $d = 2 \text{ \AA}$.

Unlike in long-range diffusion, the pre-factors of both the Dirac delta and the Lorentzian functions depend on Q . The pre-factor of the Dirac delta function is called the *elastic incoherent structure factor* (EISF). The EISF is a so-called *form factor*, as it corresponds to the squared modulus of the Fourier transform of the average distribution of hydride-ions over the sites. It therefore encodes the geometry of the diffusion process. For the two-site jump model, it oscillates with a period $2\pi/d$, as shown in Figure 2.7(b).

2.3.3 Fitting analysis of QENS spectra

The general approach used to analyze QENS spectra of oxide- and nitride-hydride systems consists of fitting the measured dynamical structure factor to a function of the form:

$$S_{\text{inc}}(Q, \omega) = \left[a_D(Q) \delta(\hbar\omega) + a_L(Q) \frac{1}{\pi} \frac{\hbar\Gamma(Q)}{(\hbar\omega)^2 + (\hbar\Gamma(Q))^2} \right] \otimes R(Q, \omega) + \text{bkg}(Q), \quad (2.19)$$

where $\otimes R(Q, \omega)$ denotes convolution with the instrumental resolution, and $\text{bkg}(Q)$ is a background arising from the instrument, the sample environment, or phonon scattering within the sample. An example fit is shown in Figure 2.8(a). The fitted parameters $a_D(Q)$, $a_L(Q)$, $\Gamma(Q)$, and $\text{bkg}(Q)$ are analyzed in terms of localized or long-range diffusion, as described above. Notably, the measured EISF is defined

as $\text{EISF} = a_D(Q) / (a_D(Q) + a_L(Q))$, where the denominator includes contributions that affect the overall spectral intensity but are not part of the form factor, such as the Debye-Waller factor, which is not included in eq. (2.19). When analyzing the EISF, one must also consider contributions to $a_D(Q)$ from immobile scatterers not participating in the diffusion. This is accounted for by adding a factor ϵ to the theoretical EISF to represent the presence of such immobile species:

$$\text{EISF}_{2\text{sites}} = \frac{\epsilon + \frac{1}{2} [1 + \sin(Qd)/(Qd)]}{1 + \epsilon}.$$

Figure 2.8(b) shows an example fit of the EISF to the two-site jump model.

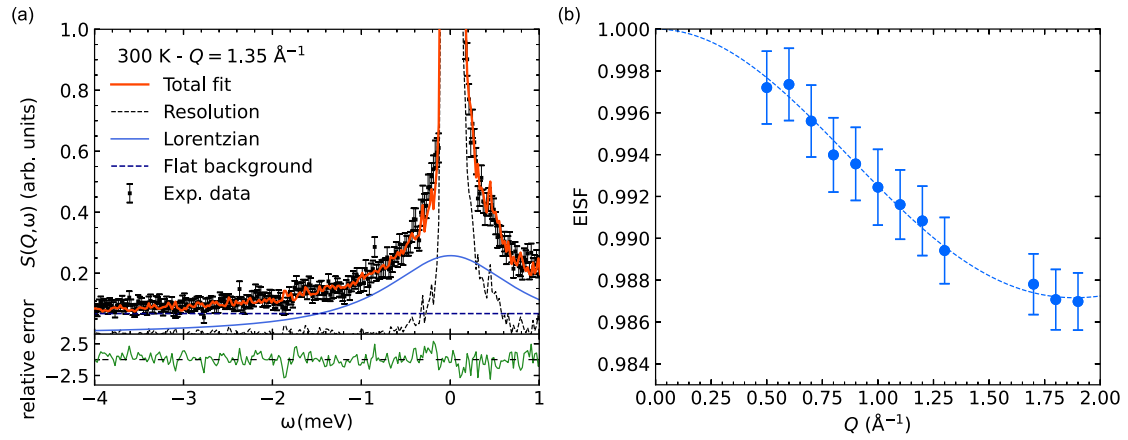


Figure 2.8: QENS data of a powder sample of $\text{SrTiO}_{2.8}\text{H}_{0.13}\square_{0.07}$ measured at 300 K on IN5 at the ILL. (a) $S(Q, \omega)$ together with fitting components of eq. (2.19). (b) EISF as obtained from the fitting analysis of $S(Q, \omega)$, together with a fit to eq. (2.3.3).

Chapter 3

Neutron spectrometers

Neutron spectrometers measure the scattering intensity from a sample as a function of energy and momentum transfer. Different spectrometer designs enable the exploration of a broad region in the $(\mathbf{Q}, \hbar\omega)$ space, typically ranging from 10^{-4} to 10^4 meV in energy transfer, and from 10^{-2} to 10^2 Å⁻¹ in momentum transfer (see Figure 3.1). Depending on the $(\mathbf{Q}, \hbar\omega)$ region of interest, a specific spectrometer design is chosen accordingly. For example, the study of optical phonons or molecular vibrations, which occur on sub-picosecond timescales, typically employs three-axis (TAS) and time-of-flight (TOF) spectrometers. In contrast, diffusional motions, which occur on longer timescales (picoseconds to nanoseconds), are better probed using backscattering techniques.

Since the energy transfer is defined as $\hbar\omega = E_i - E_f$, it can be measured via two approaches corresponding to two categories of instruments: *direct* geometry instruments, where the incident neutron energy is fixed (selected) and the scattered neutron energy is measured; and *indirect* geometry instruments, where the scattered neutron energy is fixed and the incident neutron energy is measured. This is achieved with two main components: a *primary* spectrometer, which fixes or measures the incident neutron energy, and a *secondary* spectrometer, which fixes or measures the scattered neutron energy.

The following sections describe spectrometers used in this thesis: IN5, 4SEASONS and LET (TOF spectrometers); IN1-LAGRANGE (a modified TAS spectrometer); IN16B and DNA (backscattering spectrometers).

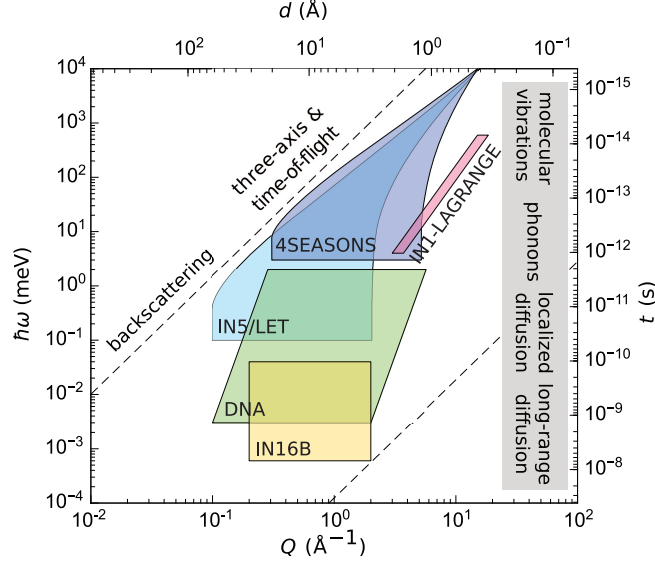


Figure 3.1: $(Q, \hbar\omega)$ space probed by the different neutron spectrometers in their typical configurations used in this thesis, along with the associated length (d) and time (t) scales, and representative types of dynamical processes occurring in different regions of the $(Q, \hbar\omega)$ space. The dashed lines indicate the typical region accessible by neutron spectroscopy.

3.1 Time-of-flight spectrometers

The TOF design enables a rapid coverage of a broad region in the $(\mathbf{Q}, \hbar\omega)$ space by simultaneously measuring all accessible \mathbf{Q} and $\hbar\omega$ values. TOF instruments use a pulsed incident neutron beam and determine the velocity, and thus the energy, of neutrons by measuring their flight time over a known distance. This distance typically refers to the path from the source of neutron pulse to the detectors. The flight time is measured relative to the moment the neutron pulse is generated, which serves as the time origin.

Direct and indirect geometries

The TOF design can be implemented with either a direct or indirect geometry:

- Direct geometry instruments: The incident neutron energy is fixed by using the flight time from the source to a monochromator *chopper* (described below). The energy of the scattered neutrons is determined by measuring the flight time

source-detectors and subtracting the known flight time source-monochromator chopper.

- Indirect geometry instruments: The energy of the scattered neutrons is fixed using crystal analyzers. The incident neutron energy is determined by measuring the flight time source-detectors and subtracting the known flight time sample-detectors.

Primary spectrometer

Direct geometry instruments, such as IN5 at the ILL [71], LET at the ISIS Neutron and Muon Source [72], or 4SEASONS at the Japan Proton Accelerator Research Complex (J-PARC) [73, 74], typically use a system of *choppers*, consisting of a series of rotating disks placed perpendicularly to the neutron beam prior to the sample. These disks are coated with a neutron-absorbing material and contain one or more windows that periodically allow the beam to pass through. The choppers rotate at frequencies that are usually integer multiples of the neutron source pulse frequency. Figure 3.2(a) illustrates the chopper system of IN5 as an example. In the case of IN5, neutrons are produced in the reactor source of the ILL and are then slowed down to energies on the order of 1 meV in a moderator (the cold source) before reaching the chopper system. The first chopper is a pair of counter-rotating disks known as the *pulsing chopper*, which creates short neutron pulses from the continuous beam. After the pulsing chopper, another pair of disks forms the *frame overlap chopper*, which reduces the effective pulse frequency by selectively blocking certain pulses. This avoids contamination from slower neutrons from pulse n entering the detection window for pulse $n + 1$. This timing logic is illustrated in the time-distance diagram in Figure 3.2(b). Finally, a third pair of disks, the *monochromator chopper*, fixes the desired E_i by opening at the precise moment when neutrons of that energy arrive at the chopper position, and remaining closed for the rest of the pulse duration. By adjusting the rotation speed and phase of this chopper, one can control the energy bandwidth of transmitted neutrons, and tune the energy resolution of the instrument. Before reaching the sample, the neutron beam passes through a *monitor* that measures the incident neutron flux for later normalization.

LET has a geometry very similar to that of IN5 but uses neutrons from the spallation source at ISIS, which is a pulsed source. As a result, it does not require a pulsing chopper.

Similarly, 4SEASONS shares a comparable geometry with IN5 and LET and operates with neutrons from the spallation (pulsed) source at J-PARC, and does not require a pulsing chopper. A notable distinction, however, is that 4SEASONS

employs a different type of monochromator chopper, called a *Fermi chopper*, which consists of a rotating cylinder containing an array of curved slits. Similarly to a monochromator chopper, a Fermi chopper opens at the moment when neutrons of

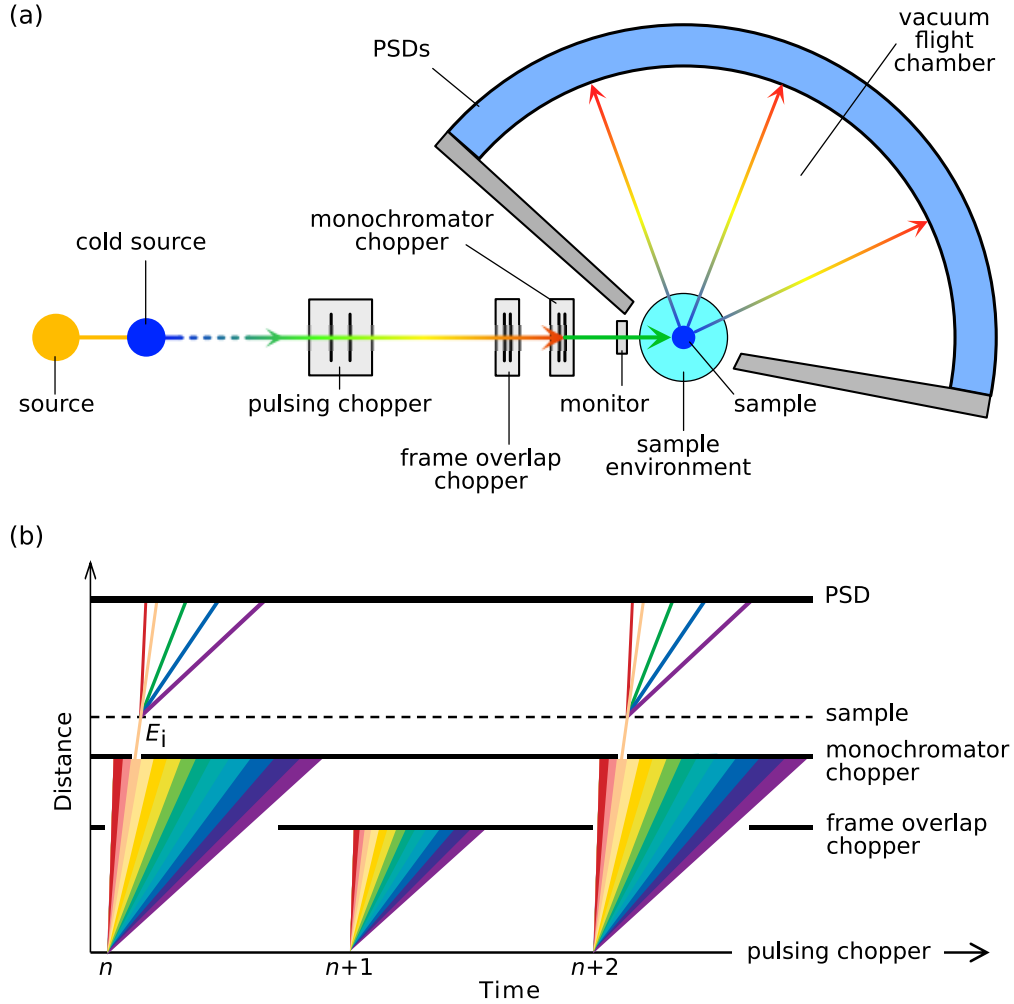


Figure 3.2: (a) Schematic view of the spectrometer IN5 at the ILL. (b) Time-distance diagram illustrating the TOF technique for a direct-geometry spectrometer at a reactor source (adapted from [68] with permission of The Licensor through PLSclear). In both diagrams, the neutron energy is represented with colors ranging from red (high energies) to purple (low energies).

the desired energy arrive at the chopper position and remains closed the rest of the time, thus fixing E_i to the desired value.

Secondary spectrometer

After being scattered by the sample, neutrons reach a large, pixelated detector array, consisting of position sensitive detector (PSD) tubes filled with ^3He gas. The energy of the scattered neutrons is determined by measuring their flight time between the sample and the PSD tubes [see Figure 3.2(b)].

Note that the raw data produced by a TOF instrument required a conversion of the flight time and scattering angle to energy and momentum transfer. Appendix B provides details on the typical data reduction routine for TOF spectrometers.

The indirect geometry is described in the following section, with the example of a hybrid TOF-backscattering spectrometer.

3.2 Backscattering spectrometers

Backscattering instruments are characterized by the use of monochromating and/or analyzing crystals arranged in a backscattering geometry, that is, at a scattering angle close to 180° . This configuration provides a very high energy resolution, typically on the order of $\sim 1 \mu\text{eV}$. The origin of this high resolution becomes evident by considering the differential form of Bragg's law:

$$(\Delta\lambda)^2 = (2\Delta d \sin \theta)^2 + (2d\Delta\theta \cos \theta)^2 \quad (3.1)$$

At $\theta = 90^\circ$, $\cos \theta = 0$ and $\Delta\lambda$ is minimal and only due to the crystal imperfections Δd .

Primary spectrometer

At continuous neutron sources, such as the ILL, instruments like IN16B employ backscattering monochromators and analyzers [75]. The incident neutron energy, E_i , is modulated using a *Doppler monochromator*, a curved crystal that oscillates linearly along the beam direction. This motion introduces a Doppler shift, allowing a precise control of E_i as a function of the oscillation speed.

At pulsed neutron sources, backscattering spectrometers typically adopt a hybrid design that combines TOF techniques with a backscattering crystal analyzer. One example is the DNA spectrometer at J-PARC [73, 76], illustrated in Figure 3.3(a). This instrument operates in an indirect geometry, where E_i is analyzed *via* the flight

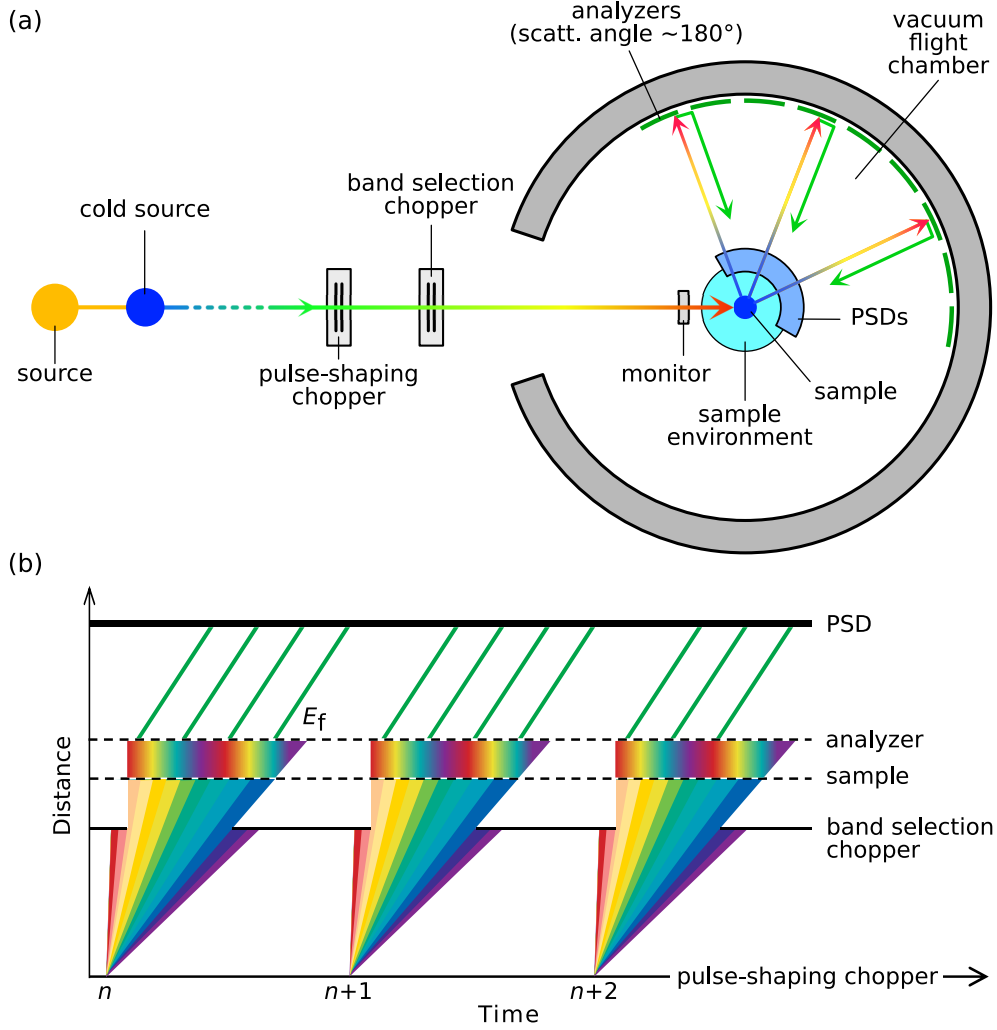


Figure 3.3: (a) Schematic view of the spectrometer DNA at J-PARC. (b) Time-distance diagram illustrating the TOF technique for a backscattering spectrometer at a pulsed source (adapted from [68] with permission of The Licensor through PLSclear). In both diagrams, the neutron energy is represented with colors ranging from red (high energies) to purple (low energies).

time of the incoming neutron pulses. Even though E_i is not fixed, the primary spectrometer of DNA uses a chopper system. It includes a *pulse-shaping chopper*, which reduces the duration of the neutron pulse from the moderator, from approximately

200 μs to 30 μs . This reduction improves the time resolution for TOF analysis but limits the accessible $\hbar\omega$ -range. The spectrometer can also be operated without the pulse-shaping chopper (by stopping it in a position where the slits are open) to increase the $\hbar\omega$ -range, at the cost of energy resolution. Another chopper, the *band selection chopper*, removes very fast and very slow neutrons from frame n that might otherwise arrive at the sample at the same time as neutrons from earlier or later frames, thereby avoiding frame overlap [see Figure 3.3(b)].

Secondary spectrometer

For both IN16B and DNA, after scattering by the sample, only neutron with a specific energy E_f are reflected by the analyzers with a scattering angle close to 180° , and collected in the PSD tubes. The PSD tubes are typically positioned slightly above and below the sample to avoid detecting neutrons scattered directly after the sample, before they are reflected by the analyzers.

In a classical backscattering instrument such as IN16B, the intensity of backscattered neutrons is measured as a function of the incident neutron energy, which is directly varied via a Doppler monochromator. This type of instrument directly measures $S(\theta, \hbar\omega)$. In contrast, a hybrid TOF-backscattering instrument like DNA measure the intensity of backscattered neutrons as a function of the total flight time from the neutron pulse source to the PSDs. This instrument measures $S(\theta, t)$, and require a conversion of the flight time t to incident neutron energy, as described in Appendix B.

Note that in both cases, converting the scattering angle to the momentum transfer is necessary.

3.3 A modified three-axis spectrometer: IN1-LAGRANGE

TAS use monochromating and analyzing crystals whose orientation is adjusted to probe specific points in the $(\mathbf{Q}, \hbar\omega)$ space. IN1-LAGRANGE (Large Area GRaphite ANalyser for Genuine Excitations), at the ILL, features a modified design, of indirect geometry, that allows simultaneous collection of data over a wide range of scattering angles, significantly reducing measurement time [see Figure 3.4(a)]. However, this comes at the expense of Q resolution, as the instrument cannot analyze the scattering angle [77]. This design is particularly well suited for studying molecular vibrations or hydride-ion vibrations in oxide- and nitride-hydride systems, which are typically

non-dispersive and do not require a Q analysis [78].

IN1-LAGRANGE is located after of the hot neutron source at the ILL, which produces neutrons with energies on the order of 500 meV. This contrasts with the TOF and backscattering spectrometers discussed earlier, which operate with cold

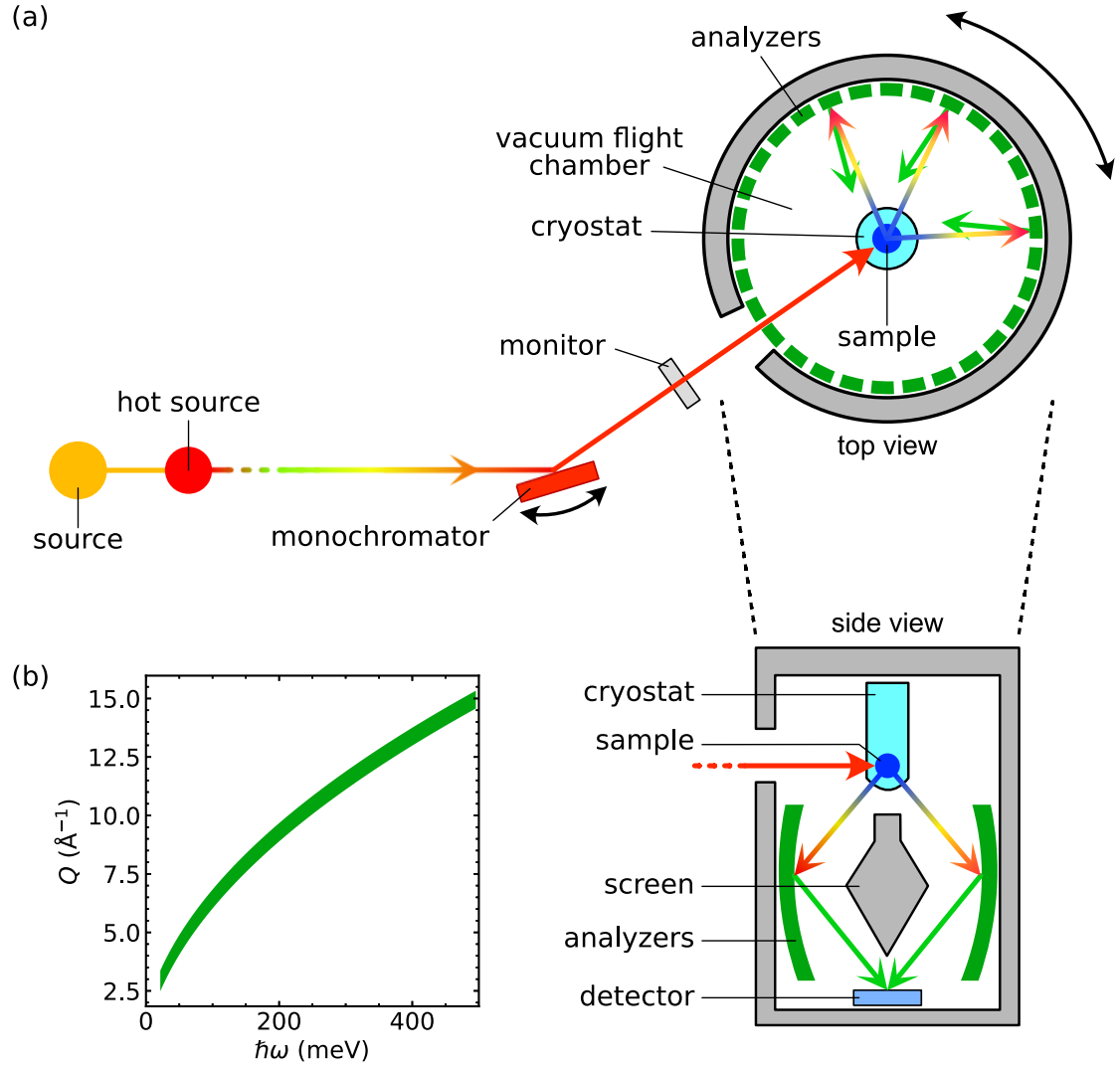


Figure 3.4: (a) Schematic view of the spectrometer IN1-LAGRANGE at the ILL. (b) $(Q, \hbar\omega)$ range probed by the instrument.

neutrons in the range of 1 meV. This distinction has important implications for the measurement of vibrational modes: IN1-LAGRANGE probes only positive energy transfers, meaning that the incident neutrons deposit the energy $\hbar\omega$ into the sample. As a result, the vibrational modes do not need to be thermally populated to be detected. Consequently, measurements can be performed at very low temperatures (typically a few kelvins), yielding spectra with sharp and well-defined peaks.

Primary spectrometer

The instrument begins with a monochromator, where either copper or silicon crystals can be chosen. The orientation of the crystal relative to the incident beam is varied during the measurement to determine the value of E_i via the Bragg's law. The choice of monochromator depends on the desired energy window: Si(111) covers an E_i range of 4.5–20 meV, Si(311) covers 16.5–60 meV, and Cu(220) covers 26–500 meV. Typically, the energy resolution of these monochromators is proportional to E_i (1–3% of E_i).

Secondary spectrometer

After scattering from the sample, neutrons are collected by a barrel-like assembly of pyrolytic graphite crystals arranged around the sample. These crystals are oriented to reflect neutrons with a fixed final energy of 4.5 meV toward a single detector. Because it collects neutrons over a limited solid angle, IN1-LAGRANGE probes a narrow, curved region in $(Q, \hbar\omega)$ space [see Figure 3.4(b)].

Note, IN1-LAGRANGE directly measures the intensity of scattered neutrons as a function of the incident neutron energy, providing $S(\hbar\omega)$ without need for further conversion.

Chapter 4

Computational methods

Theoretical approaches such as DFT and *ab initio* molecular dynamics (AIMD) are powerful tools for the calculation of neutron spectroscopy observables. While DFT allows for precise static calculations of vibrational frequencies and diffusion barriers, AIMD complements it by simulating finite-temperature time-dependent atomic motions. This allows for the observation of anharmonic vibrational effects and real-time diffusion processes that more closely reflects the thermal behavior of the system, and which can be directly compared to QENS and INS experimental data. However, DFT and AIMD are limited by relatively low computational efficiency, restricting simulations to systems of a few hundred atoms over timescales of only a few tens of picoseconds. In recent years, the development of machine learning-based molecular dynamics (MLMD) techniques has significantly advanced the ability to overcome this limitation.

This chapter provides a brief introduction about the fundamental aspects of DFT, AIMD, and MLMD, and how these methods have been applied in this thesis.¹

4.1 Density functional theory

Modeling vibrational or diffusional motions of atoms in a solid requires knowledge of the interatomic forces governing their interactions. These forces can be computed using DFT, which models the electronic structure of the solid, since electrons act as a “glue” that binds atoms together. DFT computes electronic structures based on the time-independent Schrödinger equation:

$$\hat{H}\Psi(\mathbf{r}, \mathbf{R}) = E\Psi(\mathbf{r}, \mathbf{R}), \quad (4.1)$$

¹The provided formalism is mainly based on the textbook references [79] and [80].

where \mathbf{r} and \mathbf{R} denote the positions of the electrons and nuclei, respectively, \hat{H} is the Hamiltonian of the electron-ion system, and Ψ is its corresponding wave function. The power of DFT lies in two key approximations that make the solution of eq. (4.1) computationally tractable, as outlined in the following.

1. Born-Oppenheimer approximation

Since ions are much heavier than electrons, they move on significantly slower timescales. Consequently, the electrons can be assumed to respond instantaneously to the motion of the ions. This separation of timescales justifies the Born-Oppenheimer approximation, which allows the total Hamiltonian to be separated into electronic and ionic components. In practice, the ionic positions are treated as fixed parameters in the electronic Hamiltonian, which can thus be written as:

$$\hat{H}_{\text{el}} = -\frac{\hbar^2}{2m_e} \sum_{i=1}^N \nabla_i^2 - \sum_{i=1}^N \sum_{k=1}^P \frac{Z_k e^2}{|\mathbf{r}_i - \mathbf{R}_k|} + \frac{1}{2} \sum_{i=1}^N \sum_{\substack{j=1 \\ j \neq i}}^N \frac{e^2}{|\mathbf{r}_i - \mathbf{r}_j|} \quad (4.2)$$

with N the number of electrons, i indexing electrons, P the number of ions, k indexing ions, e the elementary charge, Z_k the charge of ion k , and m_e the electron mass. The three sum in eq. (4.2) correspond to the kinetic energy of electrons, the electron-nuclei interactions, and the electron-electron interactions, respectively.

2. Hohenberg-Kohn-Sham formulation

Solving the full many-body electronic wavefunction is intractable in practice, as the memory demand grows exponentially with the number of electrons². Instead, DFT reformulates the problem in terms of the electron density $n(\mathbf{r})$, based on the Hohenberg-Kohn theorems [81]. These demonstrate that the ground-state properties of a many-electron system are uniquely determined by its electron density. They assert the existence of a universal energy functional $E[n]$ such that the ground-state energy of the system is obtained by minimizing this functional with respect to $n(\mathbf{r})$. Although this reformulation is exact in principle, the Hohenberg-Kohn theorems do not provide an explicit form for the energy functional $E[n]$. Notably, there is no known expression to calculate the kinetic energy directly from the density—except through the electronic wavefunction itself, which is too computationally demanding.

²Storing the many-body wavefunction of 5 electrons on a $10 \times 10 \times 10$ grid would require $\sim 10^{15}$ bytes!

This challenge is addressed by the Kohn-Sham approach [82], which maps the interacting many-electron system onto an auxiliary system of non-interacting electrons moving in an effective potential V_{eff} . In this formulation, the complex many-body wavefunction $\Psi(\mathbf{r})$ is replaced by a set of single-particle wavefunctions $\{\psi_i(\mathbf{r})\}_i$, and the effects of electron–electron interactions are incorporated through the so-called exchange–correlation functional, $E_{\text{xc}}[n]$. In the Kohn-Sham formalism, the electron density is easily computed as:

$$n(\mathbf{r}) = \sum_{i=1}^N |\psi_i(\mathbf{r})|^2, \quad (4.3)$$

and the total energy functional is then expressed as:

$$\begin{aligned} E_{\text{KS}}[n(\mathbf{r})] &= T_s[n(\mathbf{r})] + E_{\text{Hartree}}[n(\mathbf{r})] + E_{\text{xc}}[n(\mathbf{r})] + \int d\mathbf{r} V_{\text{ext}}(\mathbf{r})n(\mathbf{r}) \\ &= T_s[n(\mathbf{r})] + \int d\mathbf{r} V_{\text{eff}}(\mathbf{r})n(\mathbf{r}), \end{aligned} \quad (4.4)$$

where T_s is the kinetic energy functional of the non-interacting electrons, E_{Hartree} the classical Coulomb (Hartree) interaction functional, E_{xc} the exchange–correlation functional, and V_{ext} the potential due to the presence of ions or any external field. Except for the term $E_{\text{xc}}[n]$, all energy contributions are known exactly and possess analytical expressions. $E_{\text{xc}}[n]$ accounts for the many-body electron–electron interactions that are not captured by the non-interacting kinetic energy and classical Coulomb terms. The central challenge of DFT lies in finding accurate and computationally efficient approximations for $E_{\text{xc}}[n]$. Over the years, many exchange–correlation functionals have been developed and are commonly used in practice [83]. In this thesis, the PBE (Perdew-Burke-Ernzerhof) [84] and PBEsol (PBE for solids) [85] functionals were employed, both of which belong to the class of generalized gradient approximations. These functionals are known to provide a good description of vibrational properties in crystalline solids [86].

Finding the ground-state density

A practical DFT calculation consists in finding the the ground-state density that minimize E_{KS} . This is done numerically by a scheme called *self-consistent cycle* that successively update V_{eff} and n . In practice, self-consistency is reached when two consecutive densities fall below a threshold value: $|n_p - n_{p+1}| < \epsilon$. The self-consistent cycle is described in Figure 4.1.

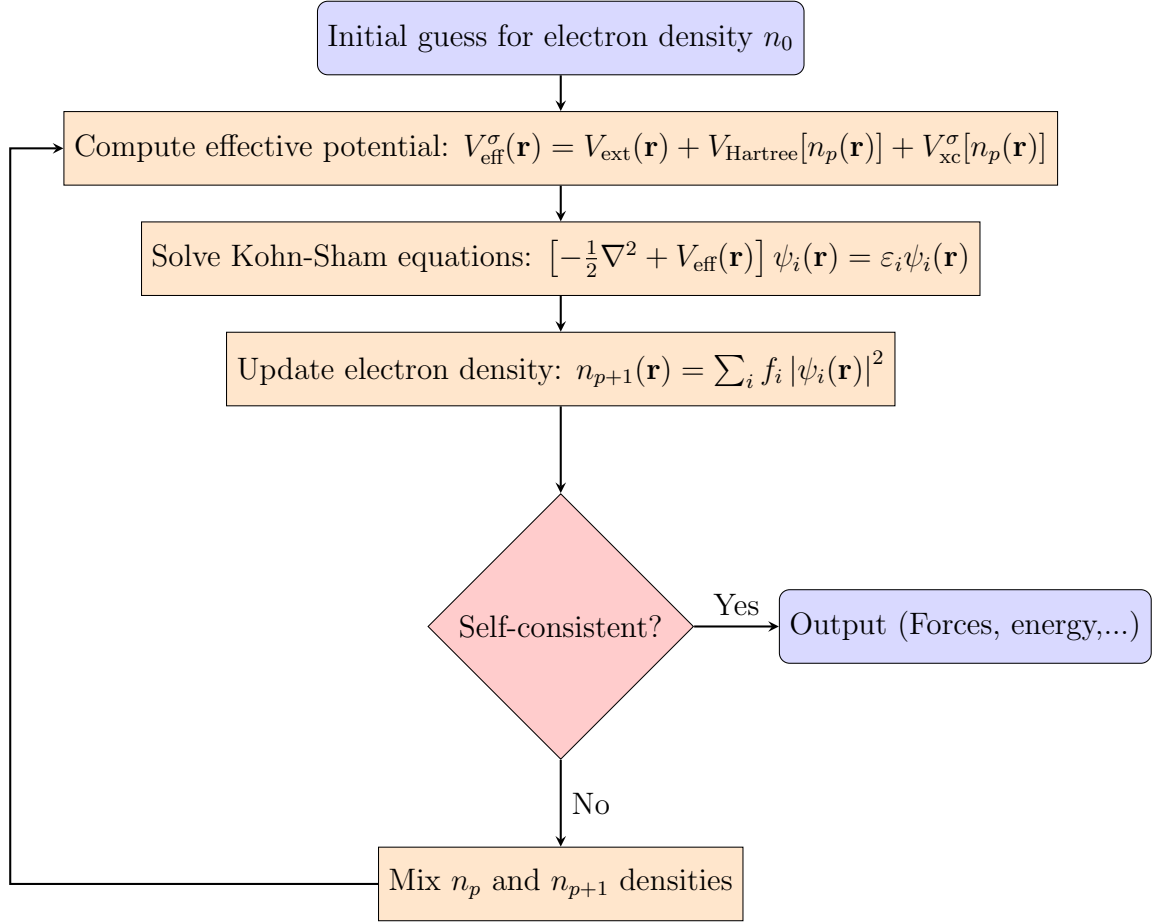


Figure 4.1: Self-consistent cycle used in DFT to calculate the ground state density. Adapted from ref. [79] with permission of The Licensor through PLSclear.

4.1.1 Modeling vibrational motions with DFT

DFT is particularly well suited to compute vibrational motions observables, such as PDOS and phonon dispersion relations. This is typically done with a so-called *finite displacement method*, which models phonons within the harmonic approximation, i.e, it assumes that atomic displacements are small compared to interatomic distances and that the potential energy V near equilibrium can be approximated as harmonic. In that case, V of the ionic system, depending on the atomic positions $(\mathbf{R}_1, \dots, \mathbf{R}_n)$,

can be expressed as a Taylor expansion around the equilibrium positions:

$$V(\{\mathbf{R}\}) = V(\{\mathbf{R}_{eq}\}) + \frac{1}{2} \sum_{i,\alpha,j,\beta} \frac{\partial^2 V(\{\mathbf{R}_{eq}\})}{\partial R_{i,\alpha} \partial R_{j,\beta}} dR_{i,\alpha} dR_{j,\beta} \quad (4.5)$$

with $\{\mathbf{R}_{eq}\}$ the equilibrium positions, and α and β indexing the cartesian coordinates $\alpha, \beta = (x, y, z)$. The so-called *second-order force constants* (FCs) are defined and numerically approximated as:

$$\Phi_{i,\alpha,j,\beta} = \frac{\partial^2 V(\{\mathbf{R}_{eq}\})}{\partial R_{i,\alpha} \partial R_{j,\beta}} = -\frac{\partial F_{j,\beta}}{\partial R_{i,\alpha}} \simeq -\frac{F_{j,\beta}(\Delta R_{i,\alpha}) - F_{j,\beta}}{\Delta R_{i,\alpha}}, \quad (4.6)$$

with $F_{j,\beta}$ the force on atom j in direction β due to the displacement of atom i in direction α , $R_{i,\alpha}$. In the numerical approximation, the atom i is slightly displaced in direction α and “frozen” at the position $R_{i,\alpha} + \Delta R_{i,\alpha}$ ($\Delta R_{i,\alpha}$ is usually between 0.1 Å and 0.3 Å), and the forces $F_{j,\beta}$ and $F_{j,\beta}(\Delta R_{i,\alpha})$ are evaluated by DFT using the Hellmann-Feynman theorem [87], providing:

$$F_i = -\frac{dE}{d\mathbf{R}_i} = -\left\langle \psi \left| \frac{d\hat{H}}{d\mathbf{R}_i} \right| \psi \right\rangle, \quad (4.7)$$

with ψ the ground state electronic wave function.

Within the harmonic approximation, the FC matrix and the equilibrium ionic positions are the only required inputs to solve the equations of motion for the ions and obtain the phonon dispersion relations and the PDOS. In this thesis, the software Phonopy was used to perform this final step, although details are not described here. Information on its implementation can be found in refs [88, 89].

4.1.2 Modeling diffusional motions with DFT

For studying diffusional motions, DFT can be used to accurately map out the potential energy surface (PES) of a system. The PES governs the dynamics of a chemical system, analogous to a ball rolling over a hilly landscape: local minima correspond to stable configurations, while crossing a local maximum, referred to as a transition state, leads to a structural transformation. Among the available methods to explore the PES, the nudged elastic band (NEB) method [90] was used in this thesis.

To be applicable, the NEB method requires the prior knowledge of both the initial and final states of the structural transformation. For example, in the case of hydride-ion migration in $\text{ATiO}_{3-x-y}\text{H}_x\Box_y$, the initial and final states correspond to the starting and ending positions of the migrating hydride-ion. Based on these

boundary conditions, a series of intermediate configurations (commonly referred to as *images*) are generated by linearly interpolating the atomic positions between the two endpoints. These images are then interconnected by artificial springs, constraining them to remain between their neighboring configurations, thereby forming an elastic band [see Figure 4.2(a)]. In the example of $\text{ATiO}_{3-x-y}\text{H}_x\text{□}_y$, only position of the hydride-ion varies between different images.

The diffusion pathway, or minimum energy path (MEP), is obtained by relaxing this elastic band, that is, by simultaneously optimizing the positions of atoms in all images, using an algorithm such as the steepest gradient descent algorithm. During this optimization, only the component of the true atomic force that is perpendicular to the reaction path is considered for each image (\mathbf{F}_i^\perp). Along the reaction path, it is the spring force between images ($\mathbf{F}_i^{\text{S||}}$) that governs the optimization. The total NEB force acting on image i is thus given by $\mathbf{F}_i^{\text{NEB}} = \mathbf{F}_i^\perp + \mathbf{F}_i^{\text{S||}}$. The calculation is considered converged once the magnitude of the total forces across all images falls below a predefined threshold.

When combined with DFT, the NEB method becomes computationally expensive, as it requires the simultaneous calculation of forces for all images. This typically

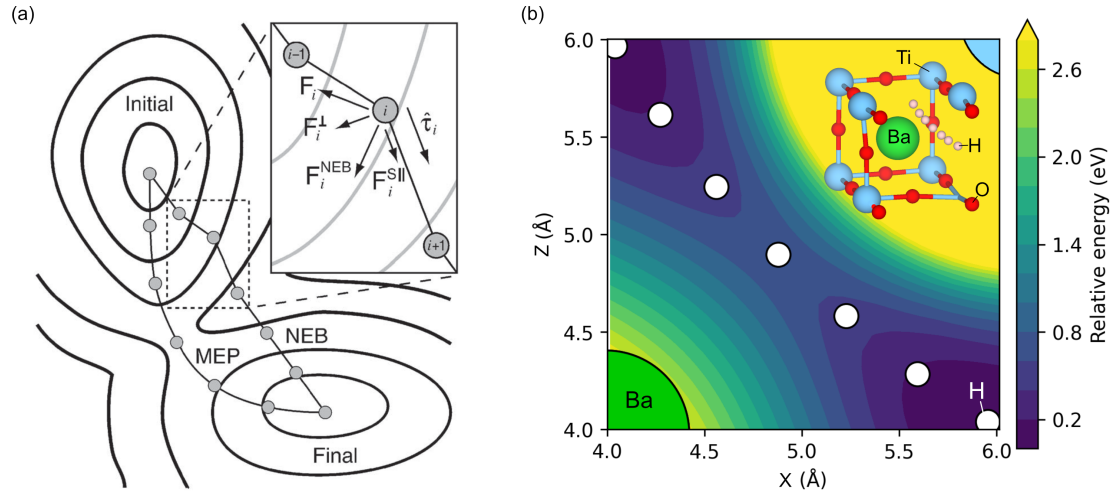


Figure 4.2: The NEB method. (a) Schematic illustration of the NEB method used to determine the MEP between an initial and a final state. Reproduced from [91] with permission. (b) PES associated with the migration of a hydride-ion in $\text{BaTiO}_{3-x-y}\text{H}_x\text{□}_y$, with its MEP overlaid (white spheres). The inset displays the unit cell with the MEP.

limits the number of images to only a few. However, it provides an accurate estimation of the energy barrier of the reaction.

4.2 Ab initio molecular dynamics

AIMD, as a molecular dynamics technique, involves computing atomic trajectories over time by solving the classical equations of motion for each atom. At each time step t of the simulation, the position and velocity of atom i (with mass m_i) for the time step $t + \Delta t$ ($\mathbf{r}_i(t + \Delta t)$ and $\mathbf{v}_i(t + \Delta t)$, respectively) are numerically integrated according to Newton’s second law using the Verlet algorithm:

$$\mathbf{r}_i(t + \Delta t) \approx \mathbf{r}_i(t) + \mathbf{v}_i(t)\Delta t + \frac{1}{2} \frac{\mathbf{F}_i(t)}{m_i} (\Delta t)^2 \quad (4.8)$$

$$\mathbf{v}_i(t + \Delta t) \approx \mathbf{v}_i(t) + \frac{\mathbf{F}_i(t) + \mathbf{F}_i(t + \Delta t)}{2m_i} \Delta t \quad (4.9)$$

As shown in eqs. (4.8) and (4.9), the only quantities required to propagate the system from time step t to $t + \Delta t$ are the forces $\mathbf{F}_i(t)$ and $\mathbf{F}_i(t + \Delta t)$. In AIMD, these forces are computed *ab initio*, i.e., by performing a DFT calculation at the current state of the system. Specifically, at each time step, the procedure is as follows: (i) $\mathbf{F}_i(t)$ is obtained *via* DFT; (ii) eq. (4.8) is used to compute the updated positions $\mathbf{r}_i(t + \Delta t)$; (iii) $\mathbf{F}_i(t + \Delta t)$ is calculated from a DFT evaluation of the system with positions $\mathbf{r}_i(t + \Delta t)$; and (iv) eq. (4.9) is applied to determine the velocities $\mathbf{v}_i(t + \Delta t)$.

Thermostats

As described above, the simulation is performed in a closed system that does not exchange energy or particles with its surroundings, i.e., in a NVE ensemble. Such ensemble is typically used when the system is already in thermodynamic equilibrium. Conversely, to bring a system to a desired temperature, a NVT ensemble is employed, where the system can exchange energy with a thermostat. These are implemented in different algorithms, such as the Berendsen thermostat, which rescales atomic velocities at each time step to match the desired temperature [92], or the Nosé-Hoover thermostat, which couples the system to an additional degree of freedom that acts as a thermal reservoir [93, 94]. Finally, an NPT ensemble can be used to control both temperature and pressure by allowing energy exchange and volume fluctuations. In this case, pressure is controlled *via* a barostat such as the Berendsen barostat, which adjusts the volume by rescaling the simulation cell dimensions at

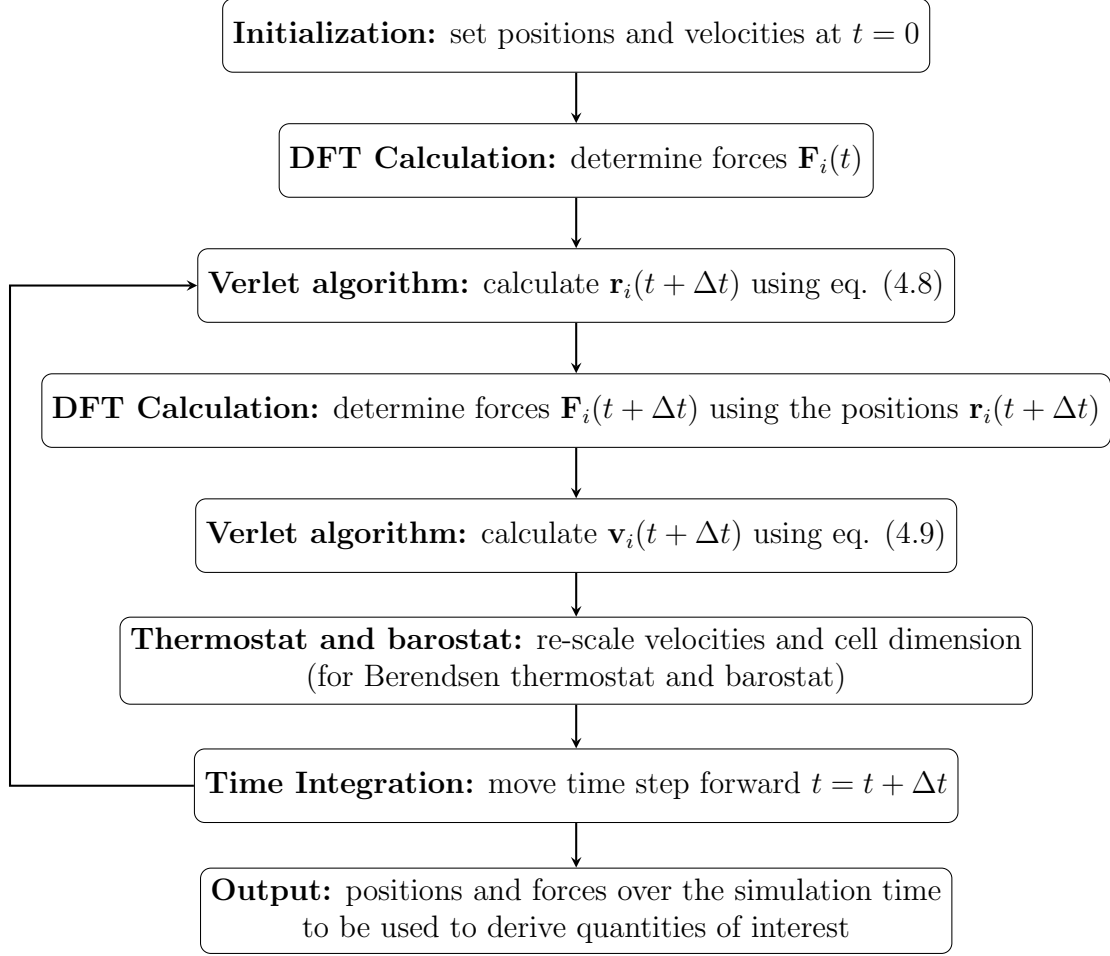


Figure 4.3: Flow chart for an AIMD simulation.

each time step [92], in combination with a thermostat.

The general algorithm used in an AIMD simulation is illustrated in Figure 4.3.

4.3 Machine learning-based molecular dynamics

AIMD has limited efficiency due to the computationally demanding DFT calculations performed at each simulation step. When the system size and/or the number of time steps becomes too large to be tractable with AIMD, MLMD can be employed

to drastically reduce the computational cost. MLMD relies on machine learning interatomic potentials³ (MLIPs), which, once trained, replace the DFT calculations for deriving the forces acting on each atom. MLIPs are constructed using a reference dataset from which the model learns the relevant structure–property relationships—such as energy, forces, and stresses—typically obtained from DFT simulations. This machine learning process can be achieved with different approaches. In this thesis, an approach based on artificial neural networks implemented in the Graphics Processing Units Molecular Dynamics (GPUMD) package was used [95–97]. This approach is briefly described in the following.

MLIP training procedure

1. A reference dataset containing a sufficiently large number of atomic configurations, and for which the energy, forces, and stresses are known from DFT calculations, is generated. The size of this dataset depends on the complexity of the system and the intended application of the MLIP. In this thesis, approximately 500 structures were used. These structures were extracted from preliminary AIMD simulations of the system, each a few picoseconds in duration. This approach ensures that the reference dataset captures the diversity of atomic environments that the MLIP is expected to encounter.
2. The reference dataset is divided into a training set, comprising 90% of the structures, and a testing set, comprising the remaining 10%. This separation ensures that the accuracy of the trained MLIP can be evaluated on structures that were never seen during training.
3. GPUMD employs a neural network architecture consisting of a *descriptors layer*, a *hidden layer*, and an *output layer* (see Figure 4.4). The descriptors layer transforms the atomic structure into a basis set constructed from atomic pair and angular correlation functions which are restricted to a cutoff radius around each atom i . Based on this, the model is further trained to predict the local energy contribution E_i for an atom as a function of its local coordination environment, and the total energy of the system is obtained as $E = \sum_i E_i$. The training process consists in updating the weights connecting the neurons between the layers in order to minimize the error between the MLIP-predicted and DFT-reference values of energies, forces, and stresses. This optimization can be performed using, for instance, gradient descent-based strategies, although the specific methods are not detailed here.

³Or, alternatively, machine learning force fields (MLFF).

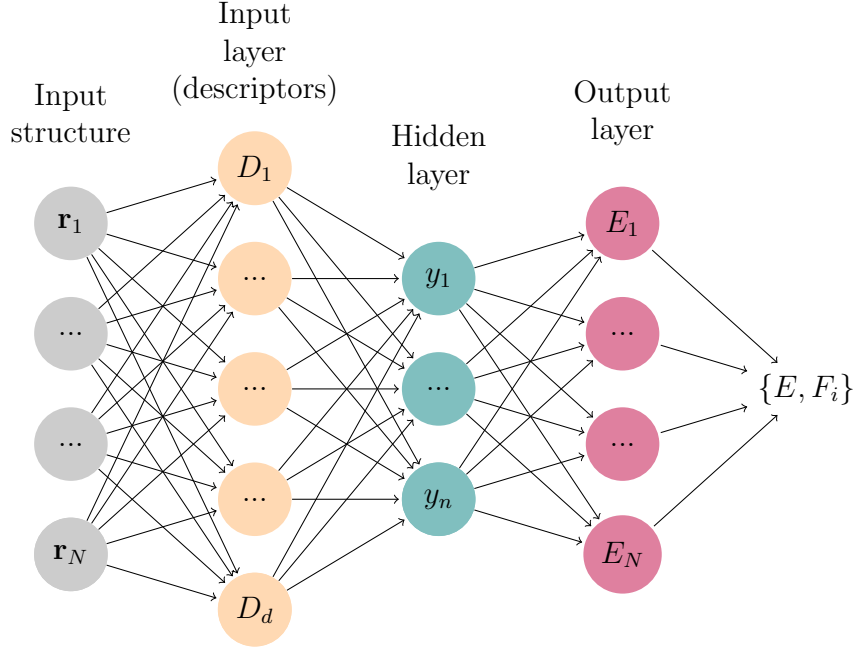


Figure 4.4: Structure of the neural network used in GPUMD. The input structure contains N atoms, d descriptors, and the hidden layer containing n neurons.

4. The MLIP is validated by comparing the MLIP-predicted and DFT-reference values of energies, forces, and stresses in the testing set. A significant deviation between these quantities usually require to train the MLIP with a more complete reference dataset, modify the cutoff radius of the descriptors, or tune the so-called hyperparameters of the neural network such as the number of neurons in the hidden layer.

Utilization of the MLIP

Once the MLIP has reached satisfactory accuracy, it can be used for production runs with larger number of atoms and/or time steps with high computational efficiency. This thesis involved preparing structures of the composition $\text{Ca}_3\text{CrN}_3\text{H}_x$ with varying amount of hydride-ion x , training a MLIP, and further using it to model vibrational and diffusional motions in this material, as outlined below.

4.3.1 Modeling vibrational motions with MLMD

AIMD or MLMD provide the positions, velocities, and forces of all atoms at each time step of the simulation, which can subsequently be used to compute various structural and dynamical properties of interest. In this thesis, MLMD was employed to calculate the GDOS in $\text{Ca}_3\text{CrN}_3\text{H}$ in cases where the system size was too large to apply the finite displacement method.

The GDOS is obtained *via* the velocity autocorrelation function, $C_{ii}(t)$:

$$C_{ii}(t) = \frac{1}{3} \langle v_i(t_0) v_i(t_0 + t) \rangle_{t_0} \quad (4.10)$$

where $\langle \rangle_{t_0}$ denotes an average over times t_0 . The Fourier transform of $C_{ii}(t)$ yields the GDOS:

$$\text{GDOS}(\omega) = \sum_i w_i \tilde{C}_{ii}(\omega) \quad (4.11)$$

with w_i a weighting factor for each atom defined as $w_i = \sigma_{i,inc} \exp(-2W_i)/4\pi m_i$, in order to allow direct comparison with INS experiments, as done in Paper II.

4.3.2 Modeling diffusional motions with MLMD

Ionic diffusion can be directly visualized either as a “movie” of the simulation or through a “cloud plot”, in which the positions of the diffusing ions are overlaid to reveal their trajectories over the course of the simulation, as illustrated in Figure 4.5(a). Ionic diffusion can also be seen in the distinct part of the van Hove correlation function, which gives the probability density of finding a particle j different from i at time t knowing that the particle i was at the origin at time $t = 0$. It is calculated over the trajectory using:

$$G^d(\mathbf{r}, t) \propto \sum_{\substack{j \\ j \neq i}} \langle \delta[\mathbf{r} - \mathbf{r}_j(t + t_0) + \mathbf{r}_i(t_0)] \rangle_{t_0} \quad (4.12)$$

Figure 4.5(b) shows $G^d(\mathbf{r}, t)$ calculated for hydride-ions in $\text{Ca}_3\text{CrN}_3\text{H}$. The pronounced increase in correlation near $r = 0$ after a few picoseconds of simulation indicates that some hydride-ions have moved from their initial positions and have been replaced by other hydride-ions, which is a characteristic signature of jump-diffusion.

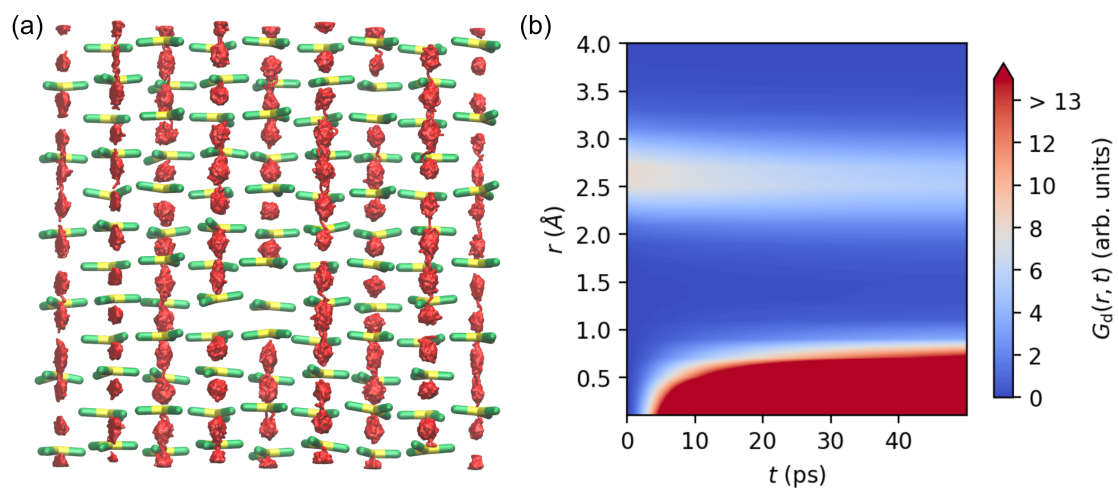


Figure 4.5: Hydride-ion diffusion in $\text{Ca}_3\text{CrN}_3\text{H}$ seen in a MLMD calculation. (a) “Clouds plot” showing the space visited by hydride-ions (in red) during 20 ps of simulation. (b) Distinct part of the van Hove correlation function for hydride-ions.

Chapter 5

Summary of results

5.1 Hydride-ion dynamics in $\text{Ca}_3\text{CrN}_3\text{H}$

This section summarizes and discusses the results on $\text{Ca}_3\text{CrN}_3\text{H}$, reported in Paper I and II. They take up the remaining open questions introduced in Chapter 1 and aim to:

1. *Investigate the local coordination environment of the hydride-ions in $\text{Ca}_3\text{CrN}_3\text{H}$ and reduce the uncertainty surrounding their exact concentration* (Paper I).
2. *Investigate the mechanism of hydride-ion transport in $\text{Ca}_3\text{CrN}_3\text{H}$* (Paper II).

5.1.1 Coordination environment and dynamics of hydride-ions in $\text{Ca}_3\text{CrN}_3\text{H}$ (Paper I)

As introduced in Section 1.2, the recently discovered nitride-hydride $\text{Ca}_3\text{CrN}_3\text{H}$ shows promise as a catalyst for ammonia synthesis, with its hydride-ions playing a central role in enabling efficient catalytic activity [29, 66]. However, both the local coordination environment of these hydride-ions and their exact content within the material remain unclear. In this study, I and my colleagues addressed these questions using INS experiments in combination with MLMD simulations. Specifically, experimentally determined vibrational frequencies of hydride-ions in $\text{Ca}_3\text{CrN}_3\text{H}$ were compared to computed spectra, enabling us to identify vibrational fingerprints that characterize the local coordination environments and dynamics of the hydride-ions present in the sample.

INS measurements were conducted at the 4SEASONS spectrometer at J-PARC and at IN1-LAGRANGE at the ILL. MLMD simulations were based on a MLIP

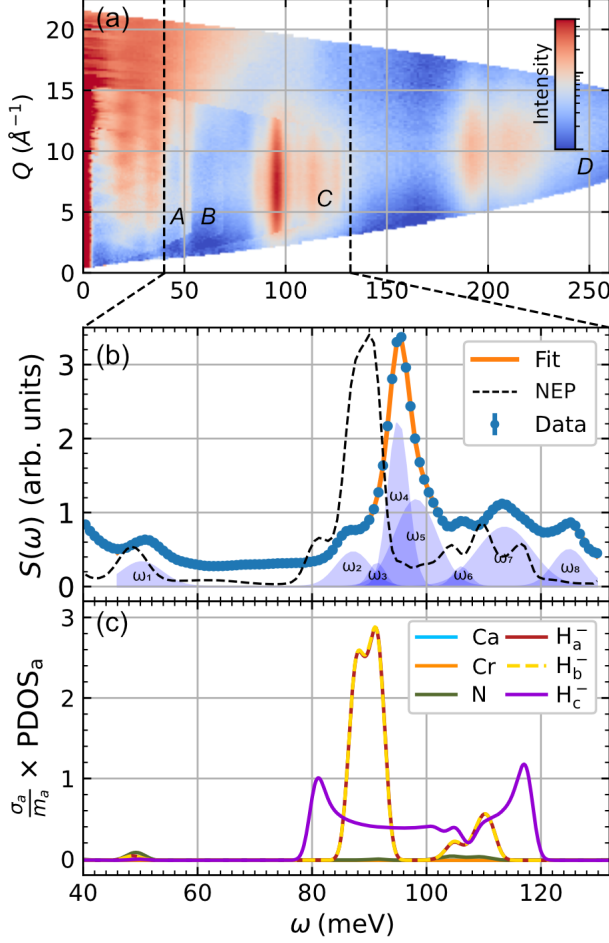


Figure 5.1: (a) INS spectra of $\text{Ca}_3\text{CrN}_3\text{H}$, as measured on 4SEASONS at 7 K with four incident neutron energies (A, B, C, D). (b) $S(\omega)$ obtained by Q -integration of spectrum C , together with a fit of the peaks with Gaussians (shaded areas) and a harmonic calculation of the INS spectrum of $\text{Ca}_3\text{CrN}_3\text{H}$, using the NEP. (c) Calculated PDOS of $\text{Ca}_3\text{CrN}_3\text{H}$, weighted by the total neutron cross section and the atomic mass of each element.

| Band | Exp. | Calc. | Proposed assignment |
|------------|------|-------|---|
| ω_1 | 50.7 | 48.5 | Cr-N bending motions |
| ω_2 | 86.9 | 81.2 | in-phase H^- motions along c |
| ω_3 | 91.3 | - | - |
| ω_4 | 94.9 | 88.2 | H^- motions in ab -plane |
| ω_5 | 97.8 | 91.1 | H^- motions in ab -plane |
| ω_6 | 106 | 104 | H^- motions along a, b , and c |
| ω_7 | 113 | 110 | H^- motions along a, b , and c |
| ω_8 | 125 | 116 | out-of-phase H^- motions along c |

Table 5.1: Experimental vibrational energies (in meV) from fits with Gaussian components, calculated frequencies (in meV), and suggested band assignment for $\text{Ca}_3\text{CrN}_3\text{H}$. ω_3 accounts for the asymmetry of the surrounding ω_2 and ω_4 peaks, and was not calculated.

called neuroevolution potential (NEP) [97], which was specifically trained for this work. Using this NEP, MD simulations on supercells of composition $\text{Ca}_3\text{CrN}_3\text{H}_x$ were performed, with x ranging from 0.64 to 1.0. The PDOS for hydride-ions was extracted from these trajectories.

The analysis (Figure 5.1) shows that the INS spectrum can be effectively modeled as a sum of eight Gaussian components (ω_1 – ω_8). The simulated spectrum agrees well with the experimental data, indicating that the modeled structure captures the essential features of the real material. This agreement enables us to assign measured vibrational bands to specific hydride-ion motions, as summarized in Table 5.1.

As seen from the PDOS and band assignments, the in-phase and out-of-phase vibrations (ω_2 and ω_8 , respectively) of hydride-ions along the c -axis (H_c^-) occur at different energies, indicating that this vibrational mode is dispersive. This dispersion reflects significant interactions between neighboring hydride-ions due to their close spacing (2.5 Å along the c -axis). In contrast, in the hypothetical composition $\text{Ca}_3\text{CrN}_3\text{H}_{0.5}$, where every other hydride site is vacant, the distance between neighboring hydride-ions increases to 5 Å, leading to the absence of dispersion. Notably, this prediction was verified by a harmonic calculation in $\text{Ca}_3\text{CrN}_3\text{H}_{0.5}$.

These findings show that vibrational dispersion of the hydride-ions along the c -axis serves as a fingerprint for the occupancy of their surrounding sites. Thus, the hydride-ion content in $\text{Ca}_3\text{CrN}_3\text{H}$ can be probed *via* its INS spectrum. This concept was further explored using MLMD simulations of $\text{Ca}_3\text{CrN}_3\text{H}_x$ for $x = 0.64$ – 1.0 (Figure 5.2). The simulated spectra show excellent agreement with experiment at $x = 1.0$. As x decreases, the intensity of ω_8 diminishes and ω_2 shifts down in energy and broadens. The absence of such trends in the experimental spectrum and the clear presence of ω_8 indicate that our sample has a high hydride-ion occupancy, likely $x > 0.95$.

I and my colleagues suggest that this high hydride-ion occupancy may contribute to high catalytic efficiency of the material for ammonia synthesis. Moreover, the presence of a small number of hydride-ion vacancies cannot be excluded, which, as discussed in the next section, are critical for hydride-ion mobility and thus for catalytic performance.

Lastly, the temperature dependence of the INS spectrum was investigated on IN1-LAGRANGE between 10 and 300 K. With increasing temperature, a broadening of vibrational peaks was observed, consistent with phonon-phonon interactions and anharmonic behavior. Interestingly, $\text{Ca}_3\text{CrN}_3\text{H}$ is known to be an electrical conductor [66], and anharmonicity generally suppresses thermal conductivity [98]. This suggests that $\text{Ca}_3\text{CrN}_3\text{H}$ may exhibit favorable thermoelectric properties.

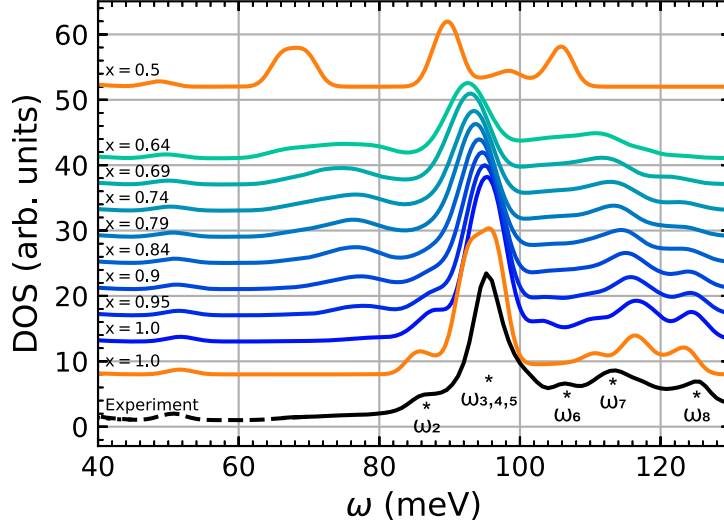


Figure 5.2: Experimental GDOS (black lines) and computed PDOS of hydride-ions for $\text{Ca}_3\text{CrN}_3\text{H}_x$ with x in the range 0.64–1, extracted from the MLMD trajectories and weighted by the total neutron cross section and atomic masses (blue lines). PDOS for $\text{Ca}_3\text{CrN}_3\text{H}$ and $\text{Ca}_3\text{CrN}_3\text{H}_{0.5}$ from the harmonic calculation, weighted by the total neutron cross section and the atomic masses are shown for comparison (orange lines). The computed PDOS lines are shifted vertically for clarity, and scaled horizontally by a factor of 1.055 in order to match the experimental data.

5.1.2 Hydride-ions transport properties of $\text{Ca}_3\text{CrN}_3\text{H}$ (Paper II)

As discussed in Section 1.2, hydride-ion transport plays a critical role in the catalytic activity of several nitride-hydride materials for ammonia synthesis, by serving as a hydrogen source for hydrogenation reactions. This behavior is also expected for $\text{Ca}_3\text{CrN}_3\text{H}$. However, while hydride-ion transport in this material has been observed at high operating temperatures (around 400 °C or 673 K), its underlying mechanism remains poorly understood. In this study, I and my colleagues investigated hydride-ion transport in $\text{Ca}_3\text{CrN}_3\text{H}$ at lower temperatures (10–300 K) using QENS on the DNA spectrometer at J-PARC and IN5 at the ILL, combined with MLMD simulations.

A preliminary analysis using a single Lorentzian fit revealed the onset of hydride-ion dynamics within the 1–10 ps timescale for temperatures above 100 K, with in-

creasing mobility at higher temperatures. However, the large uncertainties associated with this simple model limited its ability to resolve the nature of the observed dynamics. To address this, MLMD simulations were employed to better characterize the dynamics, and constrain the QENS analysis to a physically adequate model. The same MLIP as in Paper I was used to simulate hydride-ion behavior in a supercell of composition $\text{Ca}_3\text{CrN}_3\text{H}_{0.95}$. The simulations showed that at 400 K, most hydride-ions remained localized near their equilibrium positions, occasionally jumping to neighboring vacant sites, which is consistent with restricted, localized diffusion. At 600 K, however, the hydride-ions explored significantly larger regions, with multiple ions hopping across more than two sites, indicating long-range transport [Figure 5.3(a)]. This behavior is also evident in the distinct part of the van Hove correlation function [Figure 5.3(b)]. At 600 K, a strong signal at $r = 0$ Å confirms that hydride-ion sites left vacant after a jump are rapidly re-occupied by neighboring hydride-ions, confirming that hydride-ion can jump over multiple consecutive sites, without returning to their initial position.

Overall, these results reveal that hydride-ion transport occurs through a jump

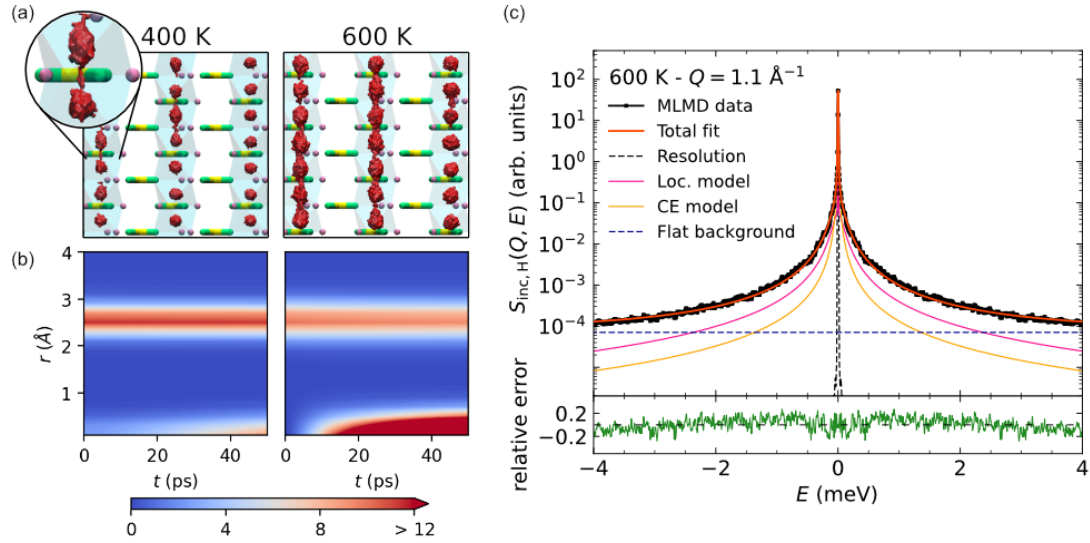


Figure 5.3: MLMD calculations for $\text{Ca}_3\text{CrN}_3\text{H}_{0.9}$. (a) Slice of the supercell at $T = 400$ K and $T = 600$ K, where the red surfaces correspond to the space visited by hydride-ions during 50 ps. The pink, yellow, and green coloring indicates Ca, Cr, and N, respectively. (b) Distinct part of the van Hove correlation function for hydride-ions. (c) Simulated QENS line at $T = 600$ K and $Q = 1.1 \text{ Å}^{-1}$ together with fits to a contained two-Lorentzian model.

mechanism involving nearest-neighbor vacancies, and that two distinct types of jump-diffusion coexist: localized back-and-forth jumps between adjacent sites, and long-range diffusion over multiple sites.

Next, based on the MLMD trajectories, QENS spectra were simulated and a constrained fitting model was applied [Figure 5.3(c)]. The model includes two Lorentzian components: one describing localized diffusion constrained by the Q -dependence of a two-site jump-diffusion model, and the other describing long-range diffusion following the Chudley–Elliott (C-E) model [70]. This model accurately reproduces the simulated QENS spectra and was then applied to experimental data.

The two-Lorentzian model successfully fit the experimental QENS spectra at all measured temperatures from 200 to 400 K. To ensure consistency, the jump distance was fixed to 2.5 Å, corresponding to the nearest-neighbor hydride-ion separation. For example, a fit at 297 K is shown in Figure 5.4(a). The fitted average residence time for long-range diffusion (τ_{CE}) decreases from 20 to 3 ps between 200 and 400 K, with an activation energy of $E_a = 52(2)$ meV. For localized diffusion, the residence time τ_{loc} similarly decreases from 5 to 1.5 ps over the same temperature range, with an activation energy of $E_a = 52(3)$ meV [Figure 5.4(b)]. This remarkable agreement

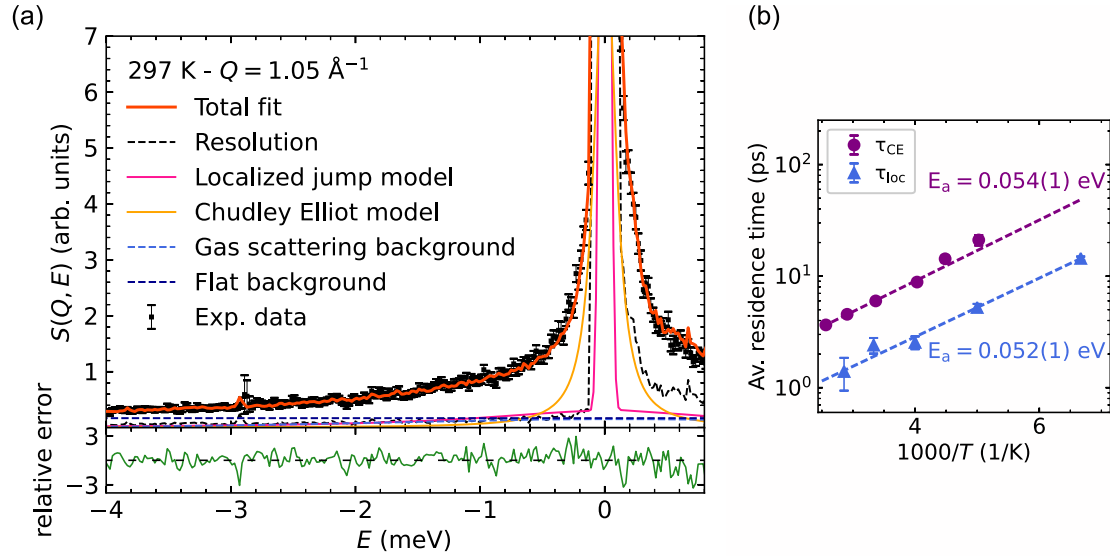


Figure 5.4: Fitting analysis of the data measured for $\text{Ca}_3\text{CrN}_3\text{H}$ with IN5 and DNA using the contained two-Lorentzian model. (a) Fit of the IN5 data. (b) Average residence times τ_{loc} and τ_{CE} , together with a fit to an Arrhenius law. Circle markers correspond to IN5 data; triangle markers correspond to DNA data.

in activation energy suggests that both diffusion processes originate from the same underlying mechanism, i.e., hydride-ion jumps between adjacent vacant sites. The corresponding hydride-ion self-diffusion coefficient (D) was found to range from $1.6 \times 10^{-5} \text{cm}^2/\text{s}$ at 200 K to $1 \times 10^{-4} \text{cm}^2/\text{s}$ at 400 K.

These results highlight the exceptional transport properties of $\text{Ca}_3\text{CrN}_3\text{H}$. Both the activation energy and self-diffusion coefficient compare very favorably to those of the best known superionic conductors (SICs). For instance, $\text{Li}_{10}\text{GeP}_2\text{S}_{12}$ [99] and $\text{Li}_{1.3}\text{Al}_{0.3}\text{Ti}_{1.7}(\text{PO}_4)_3$ [100] exhibit higher activation energies in the range of 200–300 meV [22, 101] and lower diffusion coefficients on the order of $10^{-6} \text{cm}^2/\text{s}$ at 338 K [102]. In conclusion, the remarkably low activation energy and high diffusivity of hydride-ions in $\text{Ca}_3\text{CrN}_3\text{H}$ not only underpin its high catalytic efficiency in ammonia synthesis, but also identify it as a promising candidate for future fast-ion conduction applications beyond catalysis.

5.2 Hydride-ion dynamics in $\text{ATiO}_{3-x-y}\text{H}_x\Box_y$

This section summarizes and discuss the results on $\text{ATiO}_{3-x-y}\text{H}_x\Box_y$, reported in Papers III, IV, and V. They take up the remaining open questions introduced in Chapter 1 and aim to:

1. *Clarify the discrepancies in the literature regarding the hydride-ion transport mechanism in $\text{ATiO}_{3-x-y}\text{H}_x\Box_y$ systems by developing a more complete and detailed picture of it* (Paper III and V).
2. *Investigate whether the presence of polarons or bandstates in $\text{ATiO}_{3-x-y}\text{H}_x\Box_y$ systems influence their hydride-ion transport properties* (Paper IV).

5.2.1 Mechanism of hydride-ion transport in $\text{BaTiO}_{3-x-y}\text{H}_x\Box_y$ (Paper III)

As discussed in Section 1.1, despite numerous experimental and theoretical studies, there remains no consensus on the mechanism of hydride-ion transport in $\text{BaTiO}_{3-x-y}\text{H}_x\Box_y$ systems. In this study, I and my colleagues investigated this mechanism using QENS for two samples: one with a relatively high concentration of anion vacancies, $\text{BaTiO}_{2.67}\text{H}_{0.12}\Box_{0.21}$, and one free of vacancies, $\text{BaTiO}_{2.88}\text{H}_{0.12}$. The goal was to determine whether hydride-ion transport occurs exclusively *via* a vacancy-assisted jump mechanism, and to elucidate the timescale, activation energy, and spatial characteristics of the diffusion process.

Experiments were conducted on the DNA spectrometer at J-PARC and IN16B at the ILL, across a temperature range of 50–550 K. Using both the high-resolution (HR) and low-resolution (LR) setups of DNA, probing dynamics over a ~ 1 –500 ps timescale, and for $T > 250$ K, two distinct timescales of hydride-ion diffusion were observed in the sample $\text{BaTiO}_{2.67}\text{H}_{0.12}\square_{0.21}$. Independent fits to the HR and LR datasets revealed that both diffusion processes correspond to jump-diffusion over distances of approximately 2.8 Å, the typical spacing between NN anion sites. The faster process is characterized by residence times on the order of 10 ps, while the slower process exhibits residence times on the order of 1 ps. However, due to partial overlap in the dynamic ranges of the HR and LR data, the slower process may interfere with the fitting analysis of the faster process in the LR dataset, which may influence the results.

Consequently, to improve robustness, and particularly in the temperature dependence of residence times and jump distances, a combined analysis using a shared, constrained fitting model across both datasets was performed. The HR data was modeled as:

$$S(Q, E)_{\text{HR}} = [I_{\text{el,HR}}(Q)\delta(E) + I_{\text{L1,HR}}\mathcal{L}_1(E; Q)] \otimes R_{\text{HR}}(Q, E) + \text{Bkg}_{\text{HR}}(Q), \quad (5.1)$$

where \mathcal{L}_1 is a Lorentzian constrained to follow the C-E model with a fixed jump distance of $d = 2.8$ Å. The LR data was modeled as:

$$S(Q, E)_{\text{LR}} = [I_{\text{el,LR}}(Q)\delta(E) + I_{\text{L1,LR}}\mathcal{L}_1(E; Q) + I_{\text{L2,LR}}\mathcal{L}_2(E)] \otimes R_{\text{LR}}(Q, E) + \text{Bkg}_{\text{LR}}(Q), \quad (5.2)$$

where \mathcal{L}_1 was fixed from the HR fit and \mathcal{L}_2 was also constrained to follow the C-E model with the same jump distance $d = 2.8$ Å. The results of this combined analysis are shown in Figure 5.5.

This model adequately describes both datasets up to 550 K [Figure 5.5(a–b)]. Importantly, it yields more reliable temperature dependence for the residence times compared to independent fits. The extracted average residence times range from 20–40 ps (faster diffusion) and 2–6 ps (slower diffusion), both decreasing with increasing temperature. Corresponding self-diffusion coefficients are on the order of 10^{-6} cm²/s and 10^{-5} cm²/s, respectively. The faster diffusion component follows an Arrhenius behavior with an activation energy of $E_a = 92(2)$ meV [Figure 5.5(c)].

I and my colleagues speculate that the different timescales may reflect that the respective diffusion processes occur in different local structures of the material, such as in regions of relatively high or low anion vacancy content, respectively, as illustrated in Figure 5.5(d). This idea is supported by our analysis of the PXRD data,

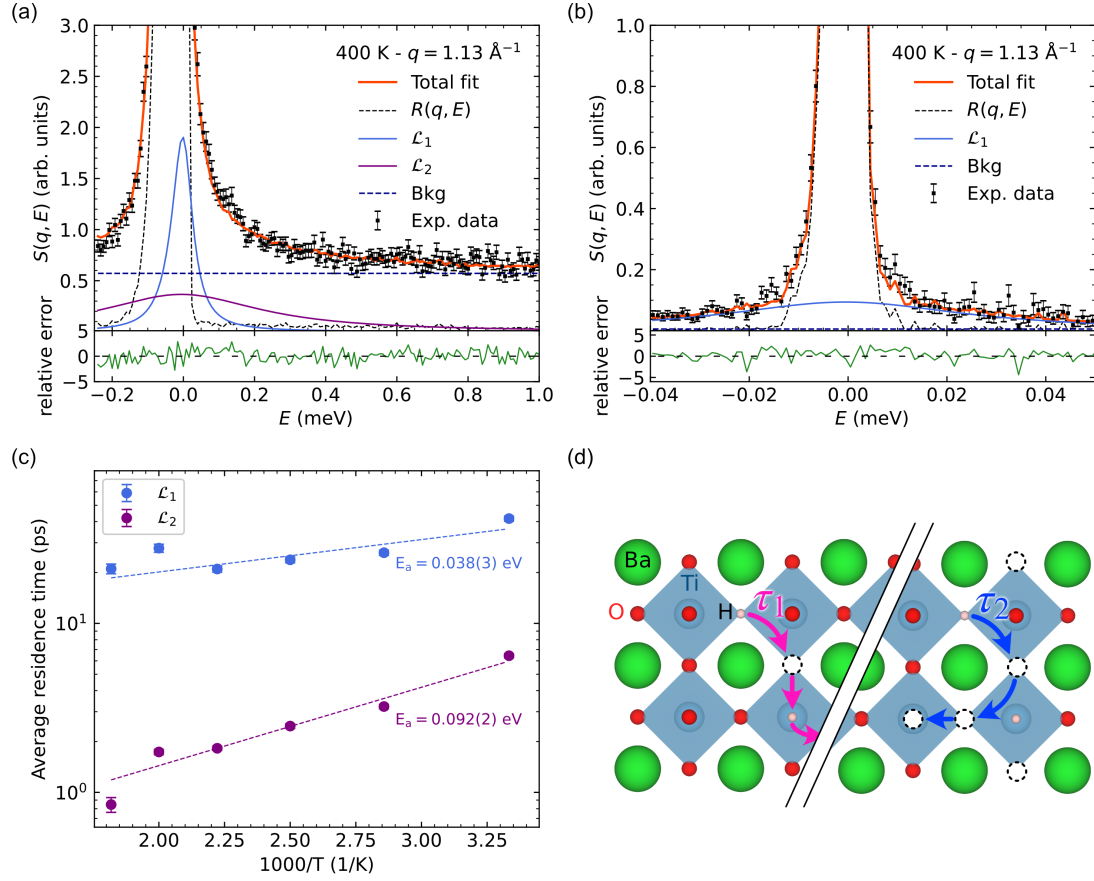


Figure 5.5: QENS data and fitting results from the combined analysis of $\text{BaTiO}_{2.67}\text{H}_{0.12}\square_{0.21}$. (a) Measured $S(Q, E)$ using the LR setup, with fit from the combined model. (b) Measured $S(Q, E)$ using the HR setup, with fit from the combined model. (c) Temperature dependence of the average residence times for the two diffusion processes. Dashed lines represent Arrhenius fits, with extracted activation energies indicated. (d) Schematic illustration of a possible microscopic interpretation of the two distinct timescales, suggesting hydride-ion diffusion in regions with different anion vacancy concentrations.

which revealed two slightly different cubic phases of the material, which may be characterized by different anion vacancy contents. Such variations may hypothetically originate near grain boundaries, where the reduction reaction could occur more efficiently than in the bulk material.

Notably, comparisons with previous QENS studies on related oxyhydrides further support this interpretation. The timescale of the faster process resembles that of hydride-ion diffusion seen in $\text{LaSrCoO}_3\text{H}_{0.7}$ [50], a compound with a high concentration of anion vacancies. Conversely, the timescale of the slower process is similar to that observed in SrVO_2H , which is nearly stoichiometric [41, 103]. These comparisons support our finding that increasing vacancy concentration enhances hydride-ion mobility.

Finally, this conclusion is corroborated by QENS measurements on the vacancy-free sample, $\text{BaTiO}_{2.88}\text{H}_{0.12}$, which did not exhibit any significant quasielastic scattering signal. This indicates that the presence of anion vacancies is essential for hydride-ion transport in $\text{BaTiO}_{3-x-y}\text{H}_x\Box_y$ and, by extension, likely in other oxyhydrides.

5.2.2 Effects of electron localization on hydride-ion transport in $\text{BaTiO}_{3-x-y}\text{H}_x\Box_y$ (Paper IV)

As shown above, the presence of anion vacancies is essential for enabling hydride-ion transport in $\text{BaTiO}_{3-x-y}\text{H}_x\Box_y$. However, introducing hydride-ions and/or vacancies into the anion sublattice of BaTiO_3 leads to n-type doping by populating the empty Ti 3d states. This doping induces both localized electrons (electron polarons) near Ti^{4+} ions or vacancies, and delocalized electrons occupying CB states. While polarons are known to influence ion transport in various transition-metal oxides (e.g. LiV_3O_8 [58]), hydride-ion and electron conductivities in $\text{BaTiO}_{3-x-y}\text{H}_x\Box_y$ have so far been studied only independently. In particular, the effects of electron localization on hydride-ion transport have remained unexplored.

In this study, I and my colleagues modeled electron polarons and bandstates in $\text{BaTiO}_{3-2x}\text{H}_x\Box_x$ using DFT, and assessed their impact on hydride-ion transport. The calculations were performed on supercells of $\text{BaTiO}_{3-x-y}\text{H}_x\Box_y$ containing one hydride-ion and one NN anion vacancy, which introduces three doping electrons. Three scenarios, corresponding to different degrees of electron localization, were considered: two (high localization), one (partial localization), and zero (full delocalization) localized electrons. For each case, the activation energy (E_a) for a migration step of the hydride-ion to the NN vacancy was calculated. The results are presented in Figure 5.6. As shown, E_a strongly depends on the degree of electron localization:

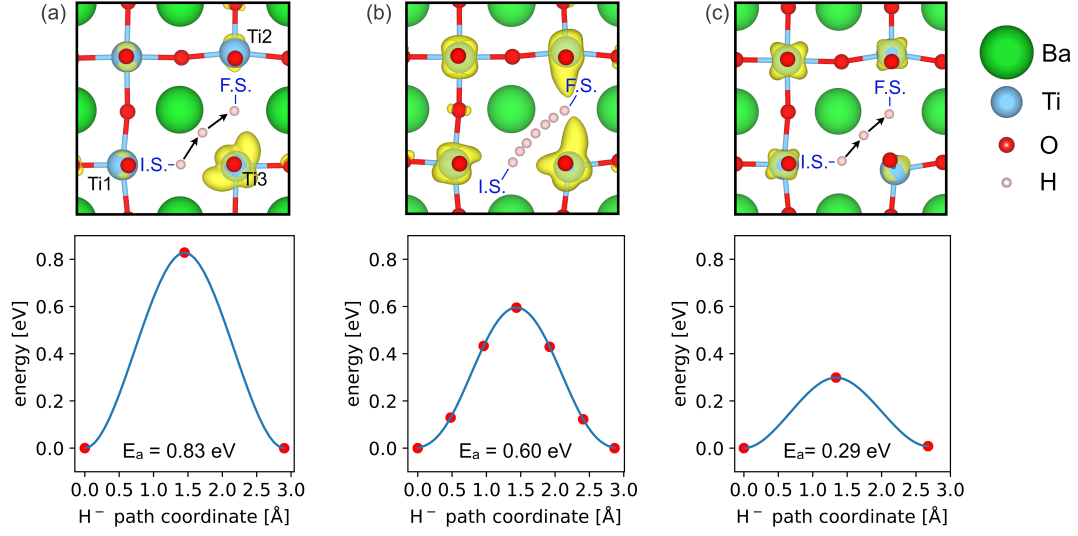


Figure 5.6: Schematic illustration of the hydride-ion migration between two neighbouring vacancies together with the energy barrier for each calculation setup (the red points represent the calculated energies, blue lines are polynomial fits). (a) High localization of doping electrons, (b) partial localization of doping electrons, and (c) full delocalization of doping electrons. The hydride-ion is shown at the initial state (I.S.), transition state, and final state (F.S.), and (b) shows, additionally, 5 intermediate states used for the calculation. In yellow is overplotted isosurfaces corresponding to the density of doping electrons at the transition state.

- In the high localization case, two of the three doping electrons are localized—one near a Ti^{4+} ion and one within the vacancy—while the third remains delocalized, both at the initial and transition states. The proximity of these localized electrons to the hydride-ion migration path increases Pauli repulsion between the e^- and the H^- , resulting in a high migration barrier of $E_a = 0.83$ eV.
- In the partial localization case, only one electron of the three doping electrons is localized, residing in the vacancy at the initial state, but becomes delocalized at the transition state. This reflects an electron transfer from the polaron state into the CB during migration, effectively “swapping” position with the hydride-ion *via* the CB. The activation energy in this case drops to $E_a = 0.60$ eV, reflecting the energetic cost of temporarily promoting the localized electron into the CB.

- In the full delocalization case, all doping electrons are delocalized and no change in the electronic structure occurs during the migration. Consequently, the barrier is reduced to $E_a = 0.29$ eV.

Overall, these results demonstrate that electron localization substantially impacts hydride-ion mobility. When a localized electron must move against the migrating hydride-ion, it incurs an additional cost in energy. Conversely, when electrons are delocalized, the barrier is lowered. These findings highlight the possibility of tuning hydride-ion conductivity *via* the electronic structure, for instance, by promoting CB delocalization through bandgap engineering.

In this study, I and my colleagues also examined a fundamental distinction between hydride-ion and proton migration by evaluating the effect of vibrational zero-point energy (ZPE) corrections on E_a . In proton conductors, ZPE corrections typically lowers E_a [104–106]. In contrast, for hydride-ion migration, ZPE corrections were found to increase the barrier by 0.01 eV. A detailed analysis suggests that this is due to the hydride-ion being more tightly bound at the transition state than at the initial state, indicating a non-adiabatic migration pathway. Unlike protons, which typically migrate on a single adiabatic PES [107], hydride-ion migration occurs *via* a transition between the intersecting PESs associated with the initial and final states. These results suggest that the migration barrier for hydride-ions is predominantly electronic in origin, and governed by non-adiabatic coupling between the PES of the initial and final states, whereas in proton conductors it is mainly dictated by ion-ion interactions.

5.2.3 Localized diffusion of hydride-ions in $\text{SrTiO}_{3-x-y}\text{H}_x\Box_y$ (Paper V)

As discussed above and in Section 1.1, hydride-ion transport in $\text{ATiO}_{3-x-y}\text{H}_x\Box_y$ systems has been primarily studied in Ba-based compounds, while their Sr-based counterparts remain less explored. In this paper, I and my colleagues investigated a sample with composition $\text{SrTiO}_{2.8}\text{H}_{0.13}\Box_{0.07}$ —which is similar to the Ba-based system studied in Paper III, $\text{BaTiO}_{2.67}\text{H}_{0.12}\Box_{0.21}$ —by probing the local hydride-ion coordination environment using INS and DFT calculations, and their diffusional dynamics using QENS. The aim was to compare the diffusion behavior in this Sr-based system to that of Ba-based systems.

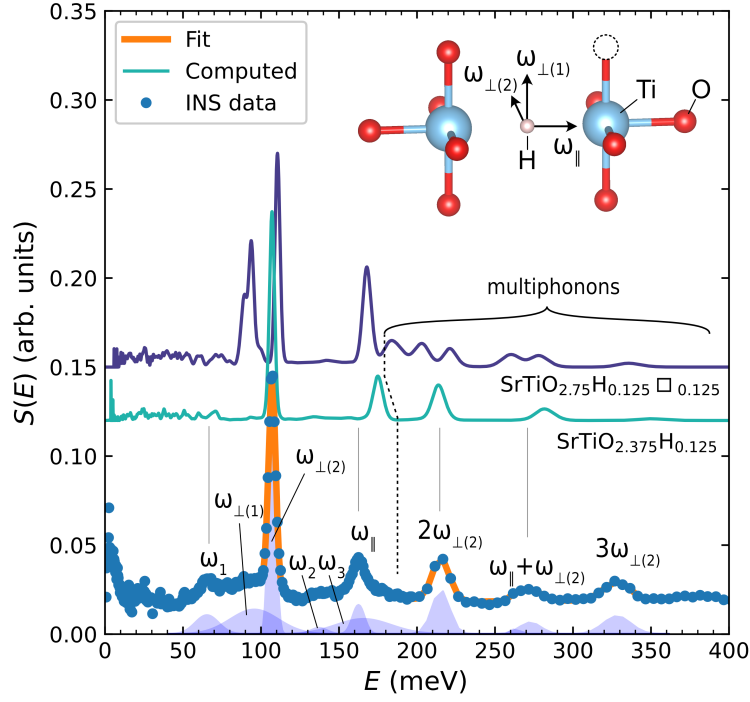
Experiments were conducted using the IN1-LAGRANGE and IN5 spectrometers at the ILL, and the LET spectrometer at the ISIS Neutron and Muon Source. Figure 5.7 shows the INS results. The experimental spectrum is well reproduced using a set of Gaussian components, and the proposed band assignments, based on

DFT calculations, are summarized in the associated table. Overall, the spectrum of $\text{SrTiO}_{2.8}\text{H}_{0.13}\square_{0.07}$ agrees well with the calculated spectrum of the vacancy-free composition $\text{SrTiO}_{2.875}\text{H}_{0.125}$. However, a weaker feature around 95 meV ($\omega_{\perp(1)}$) is present in the experimental spectrum but absent in the calculated one. In contrast, DFT calculations for $\text{SrTiO}_{2.75}\text{H}_{0.125}\square_{0.125}$ show a splitting of the Ti–H–Ti bending mode into two peaks at 85 meV and 102 meV due to a neighboring anion vacancy. Therefore, $\omega_{\perp(1)}$ is assigned to a vacancy-induced mode, suggesting that a fraction of hydride-ions are adjacent to NN anion vacancies in $\text{SrTiO}_{2.8}\text{H}_{0.13}\square_{0.07}$, which may enable NN hydride-ion transport.

Indeed, QENS measurements on IN5 and LET revealed a quasielastic signal emerging above 100 K, which was confirmed to originate from hydride-ion diffusional motions by polarization analysis on LET. The IN5 data was analyzed using a single-Lorentzian model for the hydride-ion diffusion. Figure 5.8 shows the results of this analysis. An important observation is that the FWHM of the Lorentzian component is independent of Q , typically indicating localized diffusion. The geometry of this localized motion was further analyzed using the EISF. Notably, the EISF fits a two-site jump model, yielding jump distances d between 2.25 and 3.25 Å, increasing slightly with temperature. These values correspond closely to the average NN distance (2.8 Å), indicating that the observed dynamics arise from back-and-forth jumps between NN anion vacancies. The average residence time between jumps (τ), calculated using $\tau = 4\hbar/\text{FWHM}$, ranges from 1 to 6 ps. Fitting to an Arrhenius relation yields an activation energy $E_a = 21(1)$ meV.

A key finding of this study is the observation of localized hydride-ion jump-diffusion in $\text{SrTiO}_{2.8}\text{H}_{0.13}\square_{0.07}$, in contrast to long-range jump-diffusion observed in $\text{BaTiO}_{2.67}\text{H}_{0.12}\square_{0.21}$ (Paper III). Based on our prior finding that hydride-ion transport is enabled by anion vacancies and that the diffusion rate increases with vacancy content, the localized diffusion in the present sample is attributed to an insufficient vacancy content to form continuous pathways for long-range transport. From this, the threshold vacancy content for enabling long-range diffusion in $\text{ATiO}_{2.87-y}\text{H}_{0.13}\square_y$ systems is estimated to lie between $y = 0.07$ and $y = 0.21$.

Further insight is gained by comparing the measured timescales. The τ values observed here (1–6 ps) match the slower diffusion component (2–6 ps) in $\text{BaTiO}_{2.67}\text{H}_{0.12}\square_{0.21}$, which arises from regions with lower vacancy content. However, they are significantly shorter than the faster component (20–40 ps), associated with regions of higher vacancy content. This suggests that localized and long-range diffusion can occur on similar timescales in regions with sufficient vacancy content, which may explain why localized diffusion was not distinguished from long-range diffusion in $\text{BaTiO}_{2.67}\text{H}_{0.12}\square_{0.21}$. Conversely, in regions with low vacancy content, long-range



| Band | Exp. (meV) | Calc. (meV) (\square_0) | ($\square_{0.125}$) | Proposed assignment |
|--|---------------|--------------------------------|-----------------------|-----------------------------|
| ω_1 | 65.3 | 66 | 66 | Perovskite structure |
| $\omega_{\perp(1)}$ | 95.7 | - | 85 | Ti-H-Ti bending (1) |
| $\omega_{\perp(2)}$ | 107 | 99 | 102 | Ti-H-Ti bending (2) |
| ω_2 | 137 | - | - | - |
| ω_{\parallel} | 163 | 160 | 154 | Ti-H-Ti stretching |
| ω_3 | 166 | - | - | - |
| $2\omega_{\perp(2)}$ | 215 | 198 | 204 | 2 nd order event |
| $\omega_{\perp(2)} + \omega_{\parallel}$ | 273 | 259 | 256 | 2 nd order event |
| $3\omega_{\perp(2)}$ | 328 | 297 | 306 | 3 rd order event |

Figure 5.7: (Top) INS spectrum of $\text{SrTiO}_{2.8}\text{H}_{0.13}\square_{0.07}$ measured on IN1-LAGRANGE, fitted using 9 Gaussian components. Also shown are DFT-calculated vibrational spectra for $\text{SrTiO}_{2.75}\text{H}_{0.125}\square_{0.125}$ and $\text{SrTiO}_{2.875}\text{H}_{0.125}$, vertically offset for clarity and scaled along the energy axis by a factor of 1.08. The inset schematic illustrates the directions of hydride-ion vibrational modes in $\text{SrTiO}_{2.75}\text{H}_{0.125}\square_{0.125}$. (Bottom) Table summarizing the experimental vibrational energies (in meV) extracted from the fit, alongside corresponding DFT-calculated values and the proposed mode assignments.

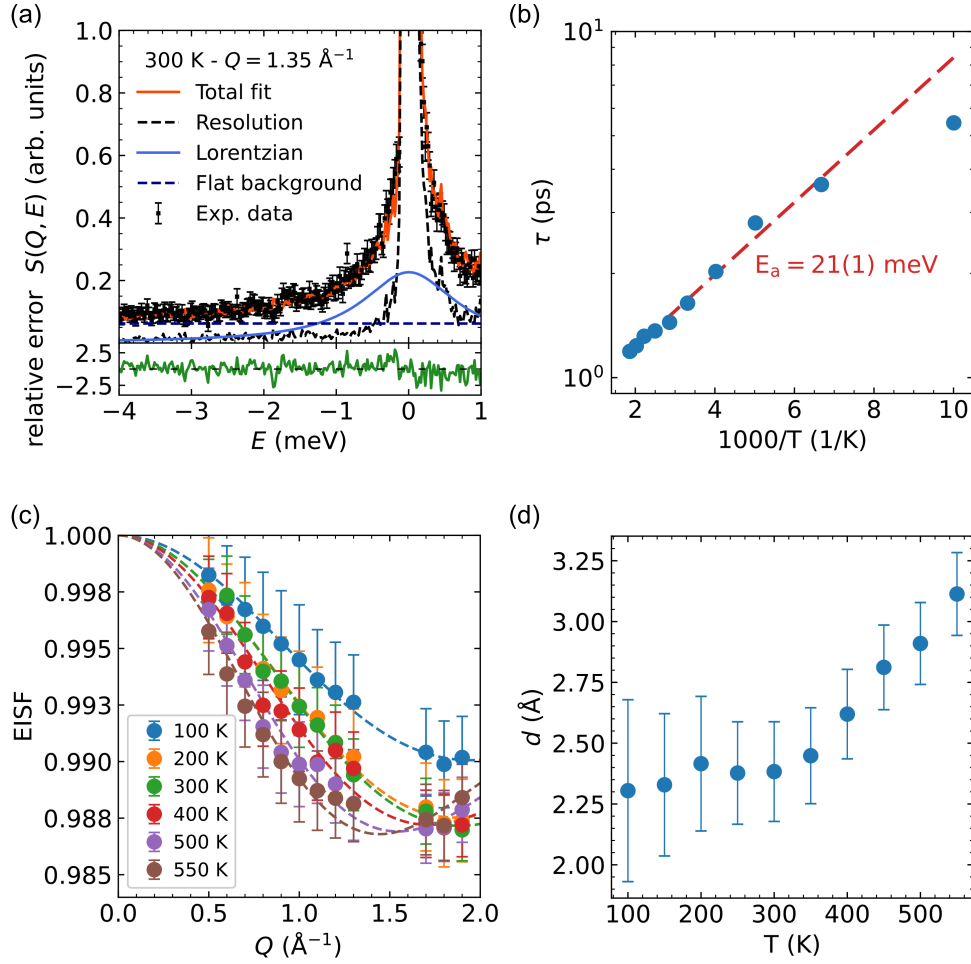


Figure 5.8: Fitting analysis of the QENS data for $\text{SrTiO}_{2.8}\text{H}_{0.13}\square_{0.07}$ measured on IN5. (a) $S(Q, E)$ with fitted components. (b) Average residence time as a function of temperature, along with a fit to an Arrhenius law (dashed red line). (c) EISF fitted to a two-site localized jump model. (d) Average jump distance extracted from the EISF fits.

diffusion is slower than localized motion due to the lack of continuous pathways of NN vacancy and hydride-ions. This interpretation is summarized schematically in Figure 5.9.

Finally, it can be noted that the apparent activation energy $E_a = 21(1)$ meV observed here is significantly lower than that for the slower diffusion process in $\text{BaTiO}_{2.67}\text{H}_{0.12}\square_{0.21}$, which was $92(2)$ meV. This difference can be attributed to the larger lattice parameter in the Ba-based system (4.02 vs. 3.91 Å for Sr), which increases the distance between neighboring vacancies. A similar trend was observed in both theoretical and experimental studies: DFT predicts $E_a = 170$ meV for Sr-based [46] and 290 meV for Ba-based systems [49]. Experimentally, oxide-ion diffusion also exhibits lower activation energy in SrTiO_3 (0.6 eV) compared to BaTiO_3 (0.7 eV) [108, 109]. These results highlight that substitution of the *A*-site cation offers a potential strategy to reduce the activation barrier and enhance hydride-ion transport in $\text{ATiO}_{3-x-y}\text{H}_x\square_y$ systems.

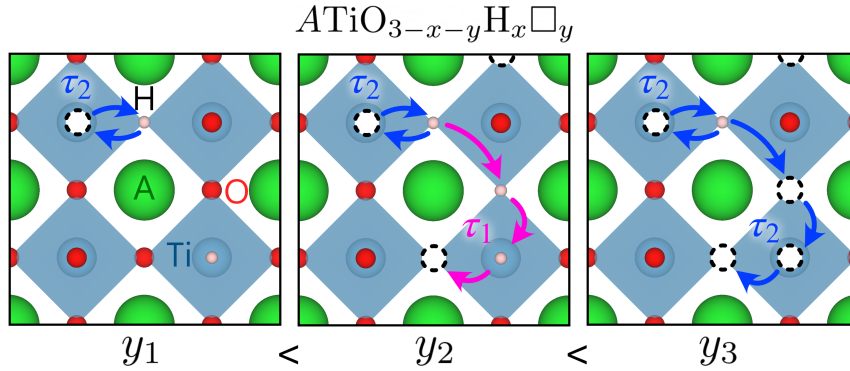


Figure 5.9: Illustration of the proposed hydride-ion diffusion mechanism in $\text{ATiO}_{3-x-y}\text{H}_x\square_y$ systems, involving two characteristic timescales: τ_2 , on the order of 1 ps, and τ_1 on the order of 10 ps.

Chapter 6

Conclusions

In conclusion, this thesis provides new insights into the fundamental mechanisms of hydride-ion transport in oxyhydride and nitride-hydride materials, which are essential for the rational design of their technological applications. By studying the oxyhydrides $\text{ATiO}_{3-x-y}\text{H}_x\Box_y$ (with $\text{A} = \text{Ba}, \text{Sr}$) and the nitride-hydride $\text{Ca}_3\text{CrN}_3\text{H}$, I and my colleagues identified key principles that likely apply broadly across similar mixed-anion systems.

Mechanisms of hydride-ion transport

To address the question *What are the underlying mechanisms governing hydride-ion transport in $\text{Ca}_3\text{CrN}_3\text{H}$ and $\text{ATiO}_{3-x-y}\text{H}_x\Box_y$?*, I and my colleagues demonstrated that hydride-ion transport is generally mediated by jump-diffusion through anion vacancies, with a geometry dictated by the host crystal structure.

In $\text{Ca}_3\text{CrN}_3\text{H}$, hydride-ions are confined into unidirectional, channel-like structures guiding their transport. Two types of diffusion were observed: (i) localized, back-and-forth jumps between adjacent NN sites, and (ii) long-range diffusion over multiple sites. Importantly, the long-range mechanism exhibits a remarkably low activation energy (50 meV) and high self-diffusion coefficients (10^{-5} – 10^{-4} cm^2/s at 200–400 K), highlighting its promise for applications in catalysis and solid-state ionics.

In $\text{ATiO}_{3-x-y}\text{H}_x\Box_y$ systems, three diffusion regimes were identified: (i) localized NN jumps featured by residence times of 1–6 ps at 100–550 K, (ii) fast long-range diffusion involving NN jumps and featured by residence times of 2–6 ps, and (iii) slower long-range diffusion involving NN jumps and featured by longer residence times of 20–40 ps at 300–550 K.

I and my colleagues also investigated the interplay between electronic and ionic transport in $\text{BaTiO}_{3-x-y}\text{H}_x\Box_y$. When electrons localize near hydride-ions (forming polarons), a strong interaction with the hydride-ions occurs, leading to increased migration barriers. This demonstrated that ionic and electronic transports are interdependent in these systems.

Structural and chemical requirements

To address the question *What are the structural and chemical requirements for enabling hydride-ion transport?*, I and my colleagues correlated our observations with the sample composition.

In $\text{ATiO}_{3-x-y}\text{H}_x\Box_y$ compounds, the presence of anion vacancies is a strict necessity for hydride-ion mobility. This suggests that it exists a threshold of vacancy content in $\text{ATiO}_{2.87-y}\text{H}_{0.13}\Box_y$ systems, lying between $y = 0.07$ and $y = 0.21$, below which transport is localized and above which percolating vacancy/hydride-ion pathways enable long-range diffusion. Moreover, the vacancy content influences the rate of diffusion, as regions with fewer vacancies exhibited slower diffusion, while higher vacancy content exhibited faster diffusion.

In $\text{Ca}_3\text{CrN}_3\text{H}$, there is a strong interactions between the hydride-ions, well visible in the vibrational spectrum of the material, and which can be interpreted in terms of average occupancy of the anionic sites. The analysis indicates the presence of a small amount (0–5%) of NN anion vacancies, enabling hydride-ion diffusion.

Strategies for enhancing hydride-ion conductivity

Based on the insights gained throughout this thesis, I now address our last research question: *How can hydride-ion conductivity be enhanced in these systems?*

Results indicate that increasing the anion vacancy content may be an effective general principle for enhancing conductivity in oxyhydrides and nitride-hydrides. However, in the $\text{ATiO}_{3-x-y}\text{H}_x\Box_y$ systems, the hydride-ion content is limited, as might be the anion vacancy content, and increasing the vacancy content might be at the cost of the hydride-ion content, which would be detrimental to the ionic conductivity. Thus, identifying an optimal balance between hydride-ion and anion vacancy content constitutes a natural extension of this work and could, for instance, be achieved with a systematic QENS study on a series of samples with varying compositions.

A second lever involves the interplay between electronic and ionic transport, particularly in $\text{ATiO}_{3-x-y}\text{H}_x\Box_y$. Results suggest that suppressing the formation of electron polarons can reduce the activation energy for hydride-ion migration. One

potential strategy to achieve this is to reduce the bandgap, thereby favoring the delocalization of doping electrons into the CB. This may be realized through cation substitution at the Ti site, effectively tuning the bandgap.

Finally, a third strategy arises from structural modifications. In $\text{ATiO}_{3-x-y}\text{H}_x\Box_y$ systems, elongation of the lattice parameter due to A-site substitution (i.e., replacing Sr with Ba) lowers the energy barrier for hydride-ion diffusion. This structural tuning presents another lever to enhance conductivity. An open question is whether a similar effect could be observed in nitride-hydride systems, such as $\text{Ca}_3\text{CrN}_3\text{H}$. This could be investigated by performing a QENS study on $\text{Ba}_3\text{CrN}_3\text{H}$, structurally similar to $\text{Ca}_3\text{CrN}_3\text{H}$ but exhibiting larger channel-like structure [110].

Appendix A

Catalytic activity of $\text{Ca}_3\text{CrN}_3\text{H}$

The reaction mechanism between H_2 and N_2 at the surface of $\text{Ca}_3\text{CrN}_3\text{H}$ was investigated using DFT calculations, with the results summarized in Figure A.1. The calculations reveal that ammonia is synthesized *via* an associative mechanism, wherein the N_2 molecule undergoes stepwise hydrogenation prior to cleavage of the $\text{N}\equiv\text{N}$ bond. The rate-determining step is identified as the initial hydrogenation of adsorbed N_2 to form N_2H , with an associated energy barrier of 0.63 eV. This is significantly more favorable than the corresponding hydrogenation involving molecular $\text{H}_2(\text{g})$, which requires 0.85 eV. Upon formation of a surface hydride-ion vacancy during this process, the site may be replenished either by hydride-ion migration from the bulk or by dissociative adsorption of a $\text{H}_2(\text{g})$ molecule, either directly at the vacancy or at a neighboring site followed by migration. Subsequent hydrogenation steps proceed *via* an alternating associative pathway, wherein the surface-bound nitrogen atom is preferentially hydrogenated over the distal nitrogen. This pathway is energetically favored by approximately 0.5 eV, leading to the formation of $\text{NH}=\text{NH}$. Further stepwise hydrogenation yields N_2H_3 and N_2H_4 ; the latter undergoes cleavage to form two NH_2 species. Finally, each NH_2 intermediate is hydrogenated to form NH_3 , completing the catalytic cycle.

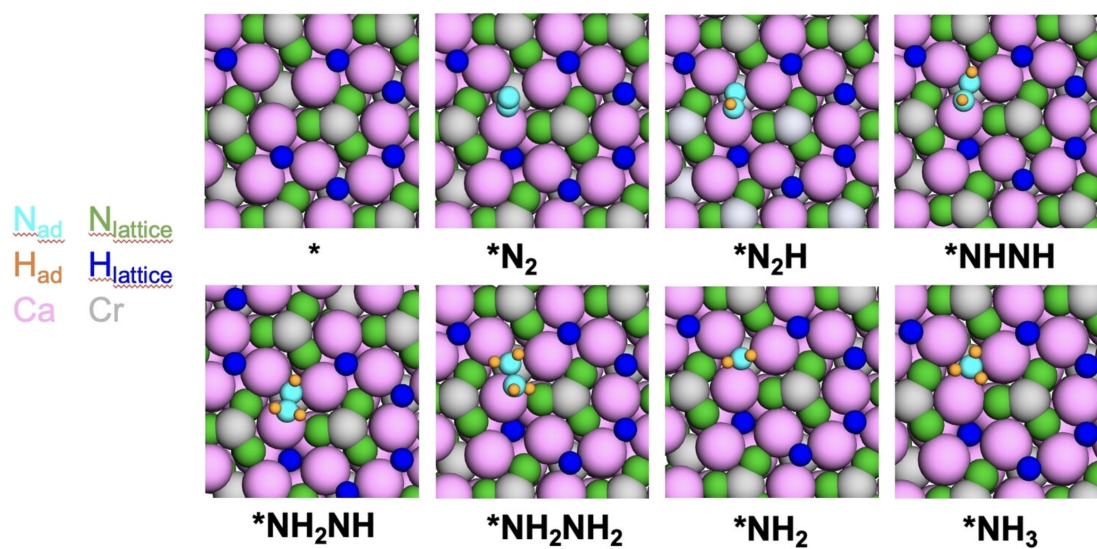


Figure A.1: Illustration of the reaction pathway for the catalytic ammonia synthesis at the surface of $\text{Ca}_3\text{CrN}_3\text{H}$. Pink, green, grey, dark blue, light blue, and orange spheres represent Ca, N, Cr, surface H, adsorbed N, and adsorbed H atoms, respectively. Reproduced with permission from [29]. Copyright 2018 John Wiley and Sons.

Appendix B

Data reduction for a TOF spectrometer¹

Data reduction

In practice, neutron scattering data must be corrected for spurious effects originating from both the instrument and the sample itself. A typical data reduction routine includes the following steps:

1. **Background noise correction.** Background noise arises from scattering events occurring before or after the sample. This includes neutrons originating from outside the instrument, as well as those scattered by the sample environment or the sample container. To subtract this background, a measurement of the empty container (C) is also performed, ideally at the same temperature as the sample measurement (X_S). The corrected signal (I) is then given by:

$$I(\theta, t) = X_S(\theta, t) - C(\theta, t) \quad (\text{B.1})$$

where t is the neutron flight time from the pulse production to the sample. This expression is only an approximation, as the sample within the container always absorbs a fraction of the incident neutrons, which are therefore not scattered. As a result, the background signal from the empty container tends to be slightly overestimated. This effect can be corrected using *self-attenuation* corrections. Another source of error is *multiple scattering*, which occurs when a single neutron is scattered more than once within the sample. Multiple scattering can be minimized by ensuring that the sample thickness is small

¹This appendix is partly based on my Licentiate thesis [67], and on the textbook reference [68].

compared to the neutron mean free path in the material. In practice, a sample transmission of approximately 90% is typically targeted.

2. **Detector normalization.** Individual detectors may have slightly different efficiencies. This variation is corrected by measuring a vanadium sample (V), which acts as a purely incoherent, elastic, and isotropic scatterer. The elastic peak of the vanadium signal is integrated over t and used to normalize the data, thereby correcting for detector-to-detector efficiency differences:

$$I_{\text{norm}}(\theta, t) = \frac{I(\theta, t)}{V(\theta)} \quad (\text{B.2})$$

3. **Converting TOF to $\hbar\omega$.** The raw data consist of neutron counts as a function of the scattering angle θ and flight time t , representing the double differential cross section in time:

$$I_{\text{norm}}(\theta, t) = \frac{d^2\sigma}{d\Omega dt} \quad (\text{B.3})$$

For direct geometry, E_i is fixed and the structure factor $S(\theta, \omega)$ is calculated *via*:

$$\hbar\omega = \frac{m_n}{2} \left(\frac{L_1^2}{t_1^2} - \frac{L_2^2}{(t - t_1)^2} \right) \quad (\text{B.4})$$

and

$$S_{\text{norm,direct}}(\theta, \omega) = \frac{k_i}{k_f} \frac{d^2\sigma}{d\Omega d\hbar\omega} = \frac{k_i}{k_f} \frac{d^2\sigma}{d\Omega dt} \frac{dt}{d\hbar\omega} = \frac{L_1(t - t_1)^4}{t_1 m_n L_2^3} \frac{d^2\sigma}{d\Omega dt}, \quad (\text{B.5})$$

with L_1 the source-sample distance, L_2 the sample-detectors distance, t_1 the source-sample flight time (fixed by E_i and L_1), $t_2 = t - t_1$ the sample-detector flight time, and m_n the neutron mass. For indirect geometry, E_f is fixed and $S(\theta, \omega)$ is calculated *via*:

$$\hbar\omega = \frac{m_n}{2} \left(\frac{L_1^2}{(t - t_2)^2} - \frac{L_2^2}{t_2^2} \right) \quad (\text{B.6})$$

and

$$S_{\text{norm,indirect}}(\theta, \omega) = \frac{L_2(t - t_2)^4}{t_2 m_n L_1^3} \frac{d^2\sigma}{d\Omega dt}, \quad (\text{B.7})$$

As seen in equations (B.5) and (B.7), the relationship between the double differential cross sections in energy and in flight time is nonlinear. Consequently,

although the dynamical structure factor is theoretically independent of the instrument type, spurious effects may arise due to this nonlinearity. For example, a time-independent background, manifesting as a constant in $\frac{d^2\sigma}{d\Omega dt}$, will appear as a diverging trend in the energy spectrum, proportional to t^4 .

4. **Detector efficiency correction.** The detector efficiency typically depends on the neutron energy and is corrected using an empirical efficiency factor, $\epsilon(E_f)$, which accounts for the variation in detector response as a function of the final neutron energy.
5. **Grouping detectors.** Detectors are grouped, and Q is determined from θ and $\hbar\omega$ using eq. (2.3).

Acknowledgements

I would like to express all my gratitude to my supervisors Maths Karlsson and Michael Marek Koza, for the great trust they placed in me, for their always encouraging feedback, and for their guidance, which allowed me to develop freely in a supportive and safe environment. Many thanks to my examiner Itai Panas for the captivating, almost philosophical discussions on the nature of matter, and for his invaluable support with the theoretical aspects of my research. I could not have undertaken this journey without Stéphane Rols, who has long been supporting me and encouraging me. Many thanks to my collaborator Hiroshi Kageyama for his warm welcome and enthusiasm at Kyoto University, as well as for providing me samples. Also thanks to all scientists that I have met and who helped me. Special thanks to Mónica Jiménez-Ruiz for her support, readiness, and for her generous internal beam-time; to Masato Matsuura, Adrien Perrichon, Markus Appel, Gøran Nilsen, Fanni Juranyi, Jacques Ollivier, Andrew Seel, Zefeng Wei.

To my colleagues and friends at the ILL and Chalmers: Laura, Ronja, Agathe, Lorenzo, Bettina, Miloš, Rasmus, Elena, Kanming, Joanna, Pedram, Peng, Oskar; thank you for your vital friendship, for your moral support and help.

Most importantly, a lot of love to my family, whose unwavering love and support made it possible for me to write these words.

Bibliography

- [1] B. Jiang, J. Iocozzia, L. Zhao, *et al.*, Chem. Soc. Rev. **48**, 1194 (2019).
- [2] Z. Zakaria, S. H. Abu Hassan, N. Shaari, *et al.*, Int. J. Energy Res. **44**, 631 (2020).
- [3] A. R. Armstrong and P. G. Bruce, Nature **381**, 499 (1996).
- [4] H. Kageyama and F. Takeiri, in *Chemistry of Mixed-anion Compounds* (Royal Society of Chemistry, 2024) pp. 1–20.
- [5] H. Kageyama, K. Hayashi, K. Maeda, *et al.*, Nat. Commun. **9**, 772 (2018).
- [6] T. S. Tripathi and M. Karppinen, Adv. Mater. Interfaces **8**, 2100146 (2021).
- [7] IEA, Net Zero by 2050, <https://www.iea.org/reports/net-zero-by-2050> (2021).
- [8] S. Ghavam, M. Vahdati, I. A. G. Wilson, and P. Styring, Front. Energy Res. **9** (2021).
- [9] N. Nesterenko, I. C. Medeiros-Costa, E. B. Clatworthy, *et al.*, Natl. Sci. Rev. **10**, nwad116 (2023).
- [10] Z. Gao, L. V. Mogni, E. C. Miller, *et al.*, Energy Environ. Sci. **9**, 1602 (2016).
- [11] P. Boldrin and N. P. Brandon, Nat. Catal. **2**, 571 (2019).
- [12] H. Fang, D. Liu, Y. Luo, *et al.*, ACS Catal. **12**, 3938 (2022).
- [13] J. Humphreys, R. Lan, and S. Tao, Adv. Energy Sustain. Res. **2**, 2000043 (2021).
- [14] V. S. Marakatti and E. M. Gaigneaux, ChemCatChem **12**, 5838 (2020).

- [15] Y. Kobayashi, O. Hernandez, C. Tassel, and H. Kageyama, *Sci. Technol. Adv. Mater.* **18**, 905 (2017).
- [16] S. Yamaguchi, *Science* **351**, 1262 (2016).
- [17] Y. Zhang, M. C. Verbraeken, C. Tassel, and H. Kageyama, in *Handbook of Solid State Chemistry* (John Wiley & Sons, Ltd, 2017) Chap. 12, pp. 477–520.
- [18] G. J. Irvine, R. I. Smith, M. O. Jones, and J. T. S. Irvine, *Nat. Commun.* **14**, 4389 (2023).
- [19] M. Kitano, Y. Inoue, H. Ishikawa, *et al.*, *Chem. Sci.* **7**, 4036 (2016).
- [20] G. Kobayashi, Y. Hinuma, S. Matsuoka, *et al.*, *Science* **351**, 1314 (2016).
- [21] H. Ubukata, F. Takeiri, K. Shitara, *et al.*, *Sci. Adv.* **7**, eabf7883 (2021).
- [22] X. He, Y. Zhu, and Y. Mo, *Nat. Commun.* **8**, 15893 (2017).
- [23] P. Zou, D. Iuga, S. Ling, *et al.*, *Nat. Commun.* **15**, 909 (2024).
- [24] M. Kitano, J. Kujirai, K. Ogasawara, *et al.*, *J. Am. Chem. Soc.* **141**, 20344 (2019).
- [25] M. Kitano, Y. Inoue, M. Sasase, *et al.*, *Angew. Chem. Int. Ed.* **57**, 2648 (2018).
- [26] M. Kitano, Y. Inoue, Y. Yamazaki, *et al.*, *Nat. Chem.* **4**, 934 (2012).
- [27] Y. Tang, Y. Kobayashi, N. Masuda, *et al.*, *Adv. Energy Mater.* **8**, 1801772 (2018).
- [28] Y. Kobayashi, O. J. Hernandez, T. Sakaguchi, *et al.*, *Nat. Mater.* **11**, 507 (2012).
- [29] Y. Cao, E. Toshcheva, W. Almaksoud, *et al.*, *ChemSusChem* **16**, e202300234 (2023).
- [30] N. Imanaka and Y. Kato, *Chem. Commun.* , 1270 (2003).
- [31] N. Imanaka, K. Okamoto, and G.-y. Adachi, *Angew. Chem. Int. Ed.* **41**, 3890 (2002).
- [32] T. Yajima, F. Takeiri, K. Aidzu, *et al.*, *Nat. Chem.* **7**, 1017 (2015).

- [33] G. Hitoki, T. Takata, J. N. Kondo, *et al.*, Chem. Commun. , 1698 (2002).
- [34] Z. Hiroi, N. Kobayashi, and M. Takano, Nature **371**, 139 (1994).
- [35] M. Al-Mamouri, P. P. Edwards, C. Greaves, and M. Slaski, Nature **369**, 382 (1994).
- [36] M. A. Hayward, E. J. Cussen, J. B. Claridge, *et al.*, Science **295**, 1882 (2002).
- [37] A. Bowman, J. B. Claridge, and M. J. Rosseinsky, Chem. Mater. **18**, 3046 (2006).
- [38] R. M. Helps, N. H. Rees, and M. A. Hayward, Inorg. Chem. **49**, 11062 (2010).
- [39] T. Sakaguchi, Y. Kobayashi, T. Yajima, *et al.*, Inorg. Chem. **51**, 11371 (2012).
- [40] T. Yajima, A. Kitada, Y. Kobayashi, *et al.*, J. Am. Chem. Soc. **134**, 8782 (2012).
- [41] F. Denis Romero, A. Leach, J. S. Möller, *et al.*, Angew. Chem. Int. Ed. **53**, 7556 (2014).
- [42] C. Tassel, Y. Goto, Y. Kuno, *et al.*, Angew. Chem. Int. Ed. **53**, 10377 (2014).
- [43] R. Nedumkandathil, A. Jaworski, J. Grins, *et al.*, ACS Omega **3**, 11426 (2018).
- [44] H. Guo, A. Jaworski, Z. Ma, *et al.*, RSC Adv. **10**, 35356 (2020).
- [45] Y. Tang, Y. Kobayashi, K. Shitara, *et al.*, Chem. Mater. **29**, 8187 (2017).
- [46] X. Liu, T. S. Bjørheim, L. Vines, *et al.*, J. Am. Chem. Soc. **141**, 4653 (2019).
- [47] C. Eklöf-Österberg, R. Nedumkandathil, U. Häussermann, *et al.*, J. Phys. Chem. C **123**, 2019 (2019).
- [48] R. Aleksis, R. Nedumkandathil, W. Papawassiliou, *et al.*, Phys. Chem. Chem. Phys. **24**, 28164 (2022).
- [49] X. Liu, T. S. Bjørheim, and R. Haugsrud, J. Mater. Chem. A **5**, 1050 (2017).
- [50] C. A. Bridges, F. Fernandez-Alonso, J. P. Goff, and M. J. Rosseinsky, Adv. Mater. **18**, 3304 (2006).
- [51] Y. Iwazaki, T. Suzuki, and S. Tsuneyuki, J. Appl. Phys. **108**, 083705 (2010).

- [52] J. Zhang, G. Gou, and B. Pan, *J. Phys. Chem. C* **118**, 17254 (2014).
- [53] C. Eklöf-Österberg, L. Mazzei, E. J. Granhed, *et al.*, *J. Mater. Chem. A* **8**, 6360 (2020).
- [54] Y. Kobayashi, Y. Tang, T. Kageyama, *et al.*, *J. Am. Chem. Soc.* **139**, 18240 (2017).
- [55] K. Page, T. Kolodiaznyi, T. Proffen, *et al.*, *Phys. Rev. Lett.* **101**, 205502 (2008).
- [56] G. Bouilly, T. Yajima, T. Terashima, *et al.*, *Chem. Mater.* **27**, 6354 (2015).
- [57] E. J. Granhed, A. Lindman, C. Eklöf-Österberg, *et al.*, *J. Mater. Chem. A* **7**, 16211 (2019).
- [58] M. Chotsawat, L. Ngamwongwan, P. Komen, *et al.*, *J. Phys. Chem. C* **126**, 18216 (2022).
- [59] S. Suthirakun, A. Genest, and N. Rösch, *J. Phys. Chem. C* **122**, 150 (2018).
- [60] P. Chen, Z. Xiong, J. Luo, *et al.*, *Nature* **420**, 302 (2002).
- [61] R. Marx, *Z. für Anorg. Allg. Chem.* **623**, 1912 (1997).
- [62] J.-F. Brice, J.-P. Motte, A. Courtois, *et al.*, *J. Solid State Chem.* **17**, 135 (1976).
- [63] H. Jacobs, R. Niewa, T. Sichla, *et al.*, *J. Alloys Compd.* **246**, 91 (1997).
- [64] A. J. E. Rowberg and C. G. Van De Walle, *ACS Appl. Energy Mater.* **4**, 6348 (2021).
- [65] Y. Guan, W. Zhang, Q. Wang, *et al.*, *Chem Catalysis* **1**, 1042 (2021).
- [66] Y. Cao, M. A. Kirsanova, M. Ochi, *et al.*, *Angew. Chem. Int. Ed.* **61**, e202209187 (2022).
- [67] L. Fine, *Neutron Spectroscopy and Computational Studies of Hydride-Ion Dynamics in Oxide- and Nitride-Hydride Materials*, Licentiate Thesis, Chalmers University of Technology (2024).
- [68] A. T. Boothroyd, *Principles of neutron scattering from condensed matter* (Oxford University Press, 2020).

- [69] P. C. H. Mitchell, S. F. Parker, A. J. Ramirez-Cuesta, and J. Tomkinson, *Vibrational Spectroscopy with Neutrons: With Applications in Chemistry, Biology, Materials Science and Catalysis*, Series on Neutron Techniques and Applications, Vol. 3 (World Scientific, 2005).
- [70] C. T. Chudley and R. J. Elliott, Proc. Phys. Soc. **77**, 353 (1961).
- [71] J. Ollivier and H. Mutka, J. Phys. Soc. Jpn. **80**, SB003 (2011).
- [72] R. I. Bewley, J. W. Taylor, and S. M. Bennington., Nucl. Instrum. Methods Phys. Res. A **637**, 128 (2011).
- [73] K. Nakajima, Y. Kawakita, S. Itoh, *et al.*, Quantum Beam Sci. **1**, 9 (2017).
- [74] R. Kajimoto, M. Nakamura, Y. Inamura, *et al.*, J. Phys. Soc. Jpn. **80**, SB025 (2011).
- [75] B. Frick, E. Mamontov, L. van Eijck, and T. Seydel, Z. Für Phys. Chem. **224**, 33 (2010).
- [76] K. Shibata, N. Takahashi, Y. Kawakita, *et al.*, in *Proc. 2nd Int. Symp. Sci. J-PARC - Unlocking Mysteries Life Matter Universe*, JPS Conference Proceedings, Vol. 8 (Journal of the Physical Society of Japan, 2015).
- [77] M. Jiménez-Ruiz, A. Ivanov, and S. Fuard, J. Phys.: Conf. Ser. **549**, 012004 (2014).
- [78] A. Ivanov, M. Jimenéz-Ruiz, and J. Kulda, in *J. Phys. Conf. Ser.*, Vol. 554 (IOP Publishing, 2014) p. 012001.
- [79] R. M. Martin, *Electronic Structure: Basic Theory and Practical Methods* (Cambridge University Press, Cambridge, 2004).
- [80] D. Marx and J. Hutter, *Ab Initio Molecular Dynamics: Basic Theory and Advanced Methods* (Cambridge University Press, 2009).
- [81] P. Hohenberg and W. Kohn, Phys. Rev. **136**, B864 (1964).
- [82] W. Kohn and L. J. Sham, Phys. Rev. **140**, A1133 (1965).
- [83] A. D. Becke, J. Chem. Phys. **140**, 18A301 (2014).
- [84] J. P. Perdew, K. Burke, and M. Ernzerhof, Phys. Rev. Lett. **77**, 3865–3868 (1996).

- [85] J. P. Perdew, A. Ruzsinszky, G. I. Csonka, *et al.*, Phys. Rev. Lett. **102**, 039902 (2009).
- [86] R. Wahl, D. Vogtenhuber, and G. Kresse, Phys. Rev. B **78**, 104116 (2008).
- [87] R. P. Feynman, Phys. Rev. **56**, 340 (1939).
- [88] A. Togo, J. Phys. Soc. Jpn. **92**, 012001 (2023).
- [89] A. Togo, L. Chaput, T. Tadano, and I. Tanaka, J. Phys.: Condens. Matter **35**, 353001 (2023).
- [90] H. Jónsson, G. Mills, and K. W. Jacobsen, in *Classical and Quantum Dynamics in Condensed Phase Simulations* (World Scientific, 1998) pp. 385–404.
- [91] D. Sheppard, R. Terrell, and G. Henkelman, J. Chem. Phys. **128**, 134106 (2008).
- [92] H. J. C. Berendsen, J. P. M. Postma, W. F. van Gunsteren, *et al.*, J. Chem. Phys. **81**, 3684 (1984).
- [93] S. Nosé, J. Chem. Phys. **81**, 511 (1984).
- [94] W. G. Hoover, Phys. Rev. A **31**, 1695 (1985).
- [95] Z. Fan, W. Chen, V. Vierimaa, and A. Harju, Comput. Phys. Commun. **218**, 10 (2017).
- [96] Z. Fan, Z. Zeng, C. Zhang, *et al.*, Phys. Rev. B **104**, 104309 (2021).
- [97] Z. Fan, Y. Wang, P. Ying, *et al.*, J. Chem. Phys. **157**, 114801 (2022).
- [98] C. Chang and L.-D. Zhao, Mater. Today Phys. **4**, 50 (2018).
- [99] N. Kamaya, K. Homma, Y. Yamakawa, *et al.*, Nat. Mater. **10**, 682 (2011).
- [100] H. Aono, E. Sugimoto, Y. Sadaoka, *et al.*, Solid State Ion. **40–41**, 38 (1990).
- [101] M. Gombotz, K. Hogrefe, R. Zettl, *et al.*, Phil. Trans. R. Soc. A **379**, 20200434 (2021).
- [102] S. Hori, R. Kanno, O. Kwon, *et al.*, J. Phys. Chem. C **126**, 9518 (2022).
- [103] R. Lavén, U. Häussermann, A. Perrichon, *et al.*, Chem. Mater. **33**, 2967 (2021).

- [104] P. G. Sundell, M. E. Björketun, and G. Wahnström, Phys. Rev. B **76**, 094301 (2007).
- [105] M. G. Wardle, J. P. Goss, and P. R. Briddon, Phys. Rev. Lett. **96**, 205504 (2006).
- [106] J. A. Ryder, A. K. Chakraborty, and A. T. Bell, J. Phys. Chem. B **104**, 6998 (2000).
- [107] M. Björketun, P. Sundell, G. Wahnstrom, and D. Engberg, Solid State Ion. **176**, 3035 (2005).
- [108] R. A. De Souza, V. Metlenko, D. Park, and T. E. Weirich, Phys. Rev. B **85**, 174109 (2012).
- [109] M. Kessel, R. A. De Souza, and M. Martin, Phys. Chem. Chem. Phys. **17**, 12587 (2015).
- [110] N. W. Falb, J. N. Neu, T. Besara, *et al.*, Inorg. Chem. **58**, 3302 (2019).